Magnetotransport and Magnetocrystalline Anisotropy Studies of Gallium Manganese Arsenide Thin Films

Christopher Stuart King, MSci (Hons)

Thesis submitted to the University of Nottingham

for the degree of Doctor of Philosophy

September 2008

Abstract

The ferromagnetic semiconductor gallium manganese arsenide is an important test-bed material for spintronics applications. Whilst a Curie temperature anywhere close to room temperature has yet to be demonstrated, the excellent micromagnetic properties, simple band structure and unusual combination of having both low moment densities and high spin-orbit coupling make this an interesting material to study from both theoretical and experimental perspectives.

This Thesis reports some experimental studies into the magnetic and magnetoresistive anisotropies in gallium manganese arsenide. In the first main chapter a study of the Anisotropic Magnetoresistance in thin (Ga,Mn)As films is reported, based on transport measurements of micro-scale devices, contributing to the first systematic study in this material. The Anisotropic Magnetoresistance comprises crystalline and non-crystalline components; this study shows that a uniaxial crystalline component can dominate over the whole range of temperatures from 2K up to the Curie temperature, the first time this has been seen in any material system to our knowledge.

The following chapter shows that the magnetic anisotropy of gallium manganese arsenide thin films can be engineered by lithographically patterning the material into structures on length scales of a micron or less. Using electron beam lithography to define the structures and SQUID magnetometery to study the resulting magnetic configuration, it is shown that the magnetic anisotropy can be greatly modified, even resulting in a switching of the easy- and hard-axis directions.

Finally a new technique based on Anisotropic Magnetoresistance measurements is presented to locate the crossover of competing magnetic anisotropy coefficients in the temperature domain. Conventionally performed by SQUID magnetometry, this new technique is cheaper and simpler whilst qualitatively reproducing the main features of the SQUID measurements.

Acknowledgements

I would like to thank the large number of people without whom my Ph.D. simply would not have been possible. First and foremost I would like to thank my supervisor Professor Bryan Gallagher for his support both academic and pastoral and for his enduring guidance with my project work. Second I would like to thank Dr. Andrew Rushforth, who I frequently turned to for advice on experiments and for help with theory, and who provided invaluable support in all areas of my Ph.D.

There are a number of other people at Nottingham who I thank for their academic support — Kevin Edmonds for his help with theory and experimental apparatus, Richard Campion and Tom Foxon for helping with my understanding of gallium manganese arsenide, Oleg Makarovsky for assistance with my earliest measurements and Chris Mellor and Ehsan Ahmad for advice on device fabrication. I would like to thank all the technicians who made my projects possible — in particular Jas Chauhan and Dave Taylor in the cleanrooms, Dave Laird and Pete Smith in the engineering support workshop and Bob Chettle and Steve Booth in the electronics workshop. Finally from Nottingham I would like to thank the other Ph.D. students in our group, especially Devin Giddings for help at the start and James Haigh for assistance towards the end.

I would also like to thank Hitachi Cambridge Laboratory for sponsoring my research, in particular those people who aided me in cleanroom processing and device fabrication in the first months of my research. Specifically I would like to thank Mohammed Khalil who imparted a vast amount of knowledge in the few days we worked together along with Jörg Wunderlich and, not least, the laboratory manager and senior researcher David Williams who acted as my industrial supervisor.

Finally I would like to thank three close collaborators from the Institute of Physics in Prague for their invaluable contributions, particularly to the work on strain relaxation; these are Kamil Olejník, Jan Zemen, and Tomas Jungwirth.

List of Publications and Conference Presentations

A. W. Rushforth, E. D. Ranieri, J. Zemen, J. Wunderlich, K. W. Edmonds, C. S. King, E. Ahmad, R. P. Campion, C. T. Foxon, B. L. Gallagher, K. Výborný, J. Kučera, and T. Jungwirth, "Voltage control of magnetocrystalline anisotropy in ferromagnetic-semiconductor-piezoelectric hybrid structures" *Physical Review B*, vol. 78, no. 8, p. 085314, 2008.

A. W. Rushforth, K. Výborný, C. S. King, K. W. Edmonds, R. P. Campion, C. T. Foxon, J. Wunderlich, A. C. Irvine, P. Vašek, V. Novák, K. Olejník, J. Sinova, T. Jungwirth, and B. L. Gallagher, "Anisotropic Magnetoresistance Components in (Ga,Mn)As," *Physical Review Letters*, vol. 99, p. 147207, 2007.

"AMR and Magnetometry Studies of GaMnAs Thin Films", oral presentation at *Current Research in Magnetism* meeting, Imperial College London, December 2006.

" In The Beginning Was The Word And The Word Was 'Aarrrrrrrr' "

The Flying Spaghetti Monster

" 88.2 percent of all statistics are made up on the spot "

Vic Reeves

Contents

Abstract i

Acknowledgements iii

List of Publications and Conference Presentations v

Contents x

1 Introduction and Background Theory 1
- 1.1 Semiconductor Spintronics . . . 1
- 1.2 Gallium Manganese Arsenide . . . 2
  - 1.2.1 Growth and Structure . . . 3
  - 1.2.2 Charge Carriers . . . 5
  - 1.2.3 Self Compensation . . . 5
  - 1.2.4 Post-growth annealing . . . 6
  - 1.2.5 Ferromagnetism . . . 7
  - 1.2.6 Curie Temperature . . . 8
- 1.3 AMR and Magnetic Anisotropies in (Ga,Mn)As . . . 9
  - 1.3.1 Spin-orbit coupling . . . 9
  - 1.3.2 AMR . . . 10
  - 1.3.3 Magnetic Anisotropies . . . 10
- 1.4 Thesis . . . 15

References . . . 17

2 AMR Studies of (Ga,Mn)As Thin Films 21
- 2.1 Introduction and Motivation . . . 21
- 2.2 Theory . . . 22
- 2.3 Fabrication and Measurement . . . 25
- 2.4 Results . . . 27
  - 2.4.1 Hall bars from wafer Mn292 . . . 27
  - 2.4.2 Hall bars from wafer Mn293 . . . 28
  - 2.4.3 Corbino disc from wafer Mn291 . . . 38
  - 2.4.4 The scaling of the longitudinal AMR with resistance . . . 40
- 2.5 Summary . . . 42

References . . . 43

3 Magnetometry Studies of Patterned (Ga,Mn)As Films **45**
3.1 Motivation . . . 45
3.2 Background and Theory . . . 46
3.3 Sample Fabrication . . . 51
3.4 Measurement and Analysis Description . . . 56
3.4.1 Remanent Magnetization Measurements . . . 56
3.4.2 Hysteresis Measurements . . . 58
3.4.3 Remanent Magnetization Simulations . . . 62
3.5 Results & Analysis — 1µm Gratings . . . 64
3.5.1 Sample Details . . . 64
3.5.2 Remanent Magnetization Measurements . . . 66
3.5.3 Summary . . . 68
3.6 Results & Analysis — 750nm Gratings . . . 72
3.6.1 Sample Details . . . 72
3.6.2 Remanent Magnetization Measurements . . . 77
3.6.3 Hysteresis Loop Measurements . . . 92
3.6.4 Collated Anisotropy Coefficients . . . 110
3.6.5 Remanent Magnetization Simulations . . . 113
3.7 Summary . . . 118
References . . . 120

4 A.C. Susceptibility Measurements by an AMR Method **123**
4.1 Introduction and Background Theory . . . 123
4.1.1 Spin Reorientation Transition . . . 123
4.1.2 A.C. Susceptibility . . . 125
4.1.3 The Peak in the A.C. Susceptibility at the SRT . . . 127
4.1.4 A.C. SQUID Magnetometry . . . 130
4.1.5 AC-AMR . . . 131
4.2 Experimental setup . . . 132
4.3 Sample details . . . 133
4.4 Results . . . 136
4.5 Discussion . . . 140
4.6 Summary and Future Work . . . 141
References . . . 142

5 Conclusions and Future Work **143**

APPENDICES

A Extraction of Crystalline AMR Terms from Hall Bar Data **145**

B Derivation of Fitting Formulae **149**

C Solenoid Design **153**

D Angle Definitions **155**

E List of Acronyms **157**

F Units of Magnetization **159**

Chapter 1

Introduction and Background Theory

1.1 Semiconductor Spintronics

The field of spintronics began to emerge in the 1980s as a natural progression from work on novel magnetic structures. It has since evolved into a revolutionary sphere of research leading to the development of whole new types of technological application. Several spintronics-based devices have already come to the mainstream electronics market, with a whole host of other potential technologies currently being researched. The breakthrough was the discovery of the Giant Magnetoresistance (GMR) effect in 1988, independently by Baibich *et. al.* in France [1] and Binasch *et. al.* in Germany [2], a technology based on magnetic multilayers which offers a magnetoresistance around ten times stronger than the simpler Anisotropic Magnetoresistance (AMR) found in monolayered systems; the discovery earned Albert Fert and Peter Grünberg the Nobel Prize for Physics in 2007. Underpinning all of the technological development is the requirement for a clear understanding of the underlying physics, which provides the basis for this Thesis.

The name *spintronics* (also called *magnetoelectronics*) is a confluence of the words

spin and *electronics* which hints at the nature of the field. Whilst conventional electronics relies upon the charge of an electron for device functionality it is possible to go a step further and exploit the quantum-mechanical spin of a charge carrier as an alternative degree of freedom to bring about new functionality, whilst also promising devices having faster switching times and reduced power consumption [3]. The continuing reduction in size of the classical transistor over the decades, now under 100 nm, will be limited by quantum mechanical effects which become more and more obstructive to the classically-governed operation of the devices. Spintronics works because of, not in spite of, quantum mechanical effects.

Spintronics was initially developed in metallic systems due to the widespread availability of ferromagnetic metals. However, there are significant advantages to implementing spintronics in semiconductor systems, the main benefit being the ease with which the new applications can be integrated into existing semiconductor architectures such as computer memory and processors. Ferromagnetism has been incorporated into semiconductors since the early 1990s but challenges for developing viable semiconductor-based spintronics applications remain, including achieving room temperature ferromagnetism and demonstrating n-type, as well as p-type, doping [3].

Whilst a review of spintronics devices and applications, current and future, is not the subject of this introduction it might be of interest to the reader, in which case the following articles are recommended: [4],[3],[5].

1.2 Gallium Manganese Arsenide

The first viable magnetic semiconductors were doped II-VIs, which are paramagnetic at all temperatures. Progress in Molecular Beam Epitaxy (MBE) allowed Ohno *et. al.* to grow the first III-V-based magnetic semiconductor, (In,Mn)As, in 1992 [6], the advantage over II-VIs being that (III,Mn)V semiconductors are ferromagnetic below a sample-specific critical temperature; the hysteresis provided by ferromagnetism is a

requisite for persistent devices. The growth of this, the first ferromagnetic semiconductor, marked the beginning of semiconductor spintronics.

(Ga,Mn)As has since become the most widely-studied of all the ferromagnetic semiconductors. The growth of this material is well under control with substitutional manganese concentrations of greater than 10% being routine nowadays, with carrier concentrations up to $\sim 10^{21}$ cm^{-3}, high Curie temperatures (compared with, for example, antimonides) and excellent micromagnetic properties. (Ga,Mn)As thin films are single-crystal with relatively low defect densities (in contrast to single metal crystals which are very hard to make) and are single-domain over square-millimetre scales. From a theoretical point, (Ga,Mn)As occupies the interesting position of having both low moment densities and high spin-orbit coupling, whilst the band structure is relatively simple.

1.2.1 Growth and Structure

Gallium manganese arsenide is grown by Molecular Beam Epitaxy by adding manganese as a dopant in standard GaAs growth, with some caveats. In the MBE growth process, single-crystal (Ga,Mn)As is formed epilayer-by-epilayer on a chosen substrate in an ultra-high vacuum environment where the grower has a great deal of control over a variety of growth parameters and conditions.

The lattice structure of single-crystal gallium arsenide is zinc-blende in nature, comprising two interpenetrating face-centred cubic sublattices — one of gallium ions and one of arsenide ions displaced by a quarter of a lattice parameter along the [111] direction — as shown in figure 1.1. The lattice parameter of fully relaxed (see section 1.3.3) GaAs is 5.653 Å and under normal conditions it is non-magnetic and insulating.

There are several viable mechanisms for the incorporation of the manganese ions into the lattice; these range from mechanisms which preserve the single-crystal structure, specifically those involving substitutional incorporation of the manganese onto

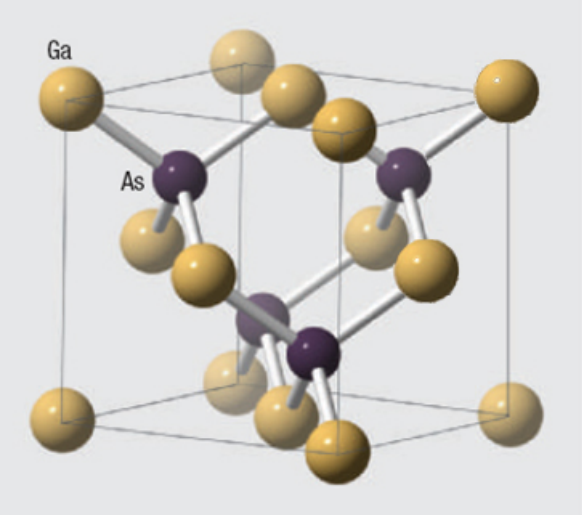

Fig. 1.1 — Gallium arsenide lattice structure. Figure adapted from Nature Materials 4, 195 (2005).

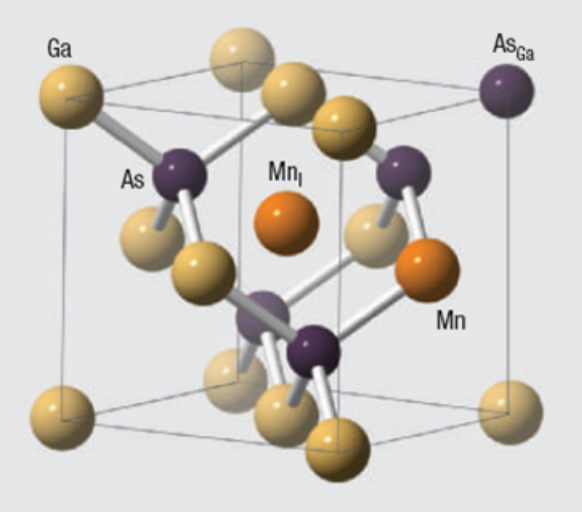

Fig. 1.2 — Gallium manganese arsenide lattice structure, showing substitutional manganese (labelled Mn), interstitial manganese (labelled Mn_I) and arsenic antisites (labelled As_{Ga} — see section 1.2.6). Figure taken from Nature Materials 4, 195 (2005).

gallium lattice sites or interstitial incorporation between lattice sites, to phase segregation which results in discrete regions of crystalline GaAs and MnAs and hence destroys the original lattice structure. Figure 1.2 shows the lattice structure of gallium manganese arsenide indicating both substitutional and interstitial manganese ions. The preferred mechanism for the manganese incorporation is by substituting for gallium ions; through careful growth control it is then possible to produce ferromagnetic single-crystal gallium manganese arsenide with high charge carrier concentrations of $\gtrsim 10^{21}$ cm^{-3}, volume magnetizations at base temperature of up to 70 emu/cm^{-3} (for (Ga_{1-x},Mn_x)As with $x > 10\%$ [7] — this compares with iron at ∼1,740, cobalt at ∼1,446 and nickel at ∼510 emu/cm^{-3} [8]), low defect densities and Curie temperatures up to ∼180 K.

1.2.2 Charge Carriers

The electronic configurations of manganese and gallium are shown in table 1.1. Due to having one fewer electron available for bonding, manganese ions which substitute for gallium ions on gallium lattice sites act as single electron acceptors, each contributing one hole as a free carrier to the lattice. Assuming that all the manganese ions in a sample of (Ga,Mn)As are in substitutional positions and the lattice is defect-free, the carrier concentration is therefore equal to the manganese concentration. The concentration of gallium in gallium arsenide is 2.2×10^{22} cm^{-3}; so ideally a sample of ($Ga_{0.9}$,$Mn_{0.1}$)As would give a hole concentration of 2.2×10^{21} cm^{-3} and 5% manganese would give 1.1×10^{21} cm^{-3}.

1.2.3 Self Compensation

In reality such hole concentrations are never achieved in as-grown samples for their respective manganese concentrations. The lowest-energy configuration for a Ga(Mn)As lattice is to be insulating, with any carrier concentration above zero being energet-

Ga	:	[Ar] $3d^{10}$ $4s^2$ $4p^1$
Mn	:	[Ar] $3d^5$ $4s^2$
As	:	[Ar] $3d^{10}$ $4s^2$ $4p^3$

Table 1.1 — Electronic structures of the atoms of gallium, manganese and arsenic.

ically unfavourable. To reduce the energy of a doped lattice there is a tendency of the system to introduce self-compensating defects during the growth in order to lower the carrier concentration. The lowest-energy self-compensation mechanism for (Ga,Mn)As is to incorporate manganese ions into the lattice interstitially. Each interstitial manganese atom can give up two electrons (table 1.1); in terms of carrier concentration, therefore, each manganese interstitial eliminates the charge carriers provided by two substitutional manganese ions. As one tries to make samples with higher and higher carrier concentrations (which also means higher and higher moment densities and Curie temperatures — see below) there is more and more tendency for the lattice to generate interstitial manganese ions. One of the main challenges in MBE growth of (Ga,Mn)As, therefore, is to increase the proportion of substitutional to interstitial manganese as far as possible. Details of MBE growth are esoteric and not the subject of this report; for those interested, further information can be found elsewhere: [9],[10],[11],[7].

1.2.4 Post-growth annealing

Fortunately the lowest-energy self-compensation mechanism is the formation of manganese interstitials. It is now well known that post-growth annealing in air of thin (Ga,Mn)As films can cause the vast majority of the interstitial manganese ions to diffuse to the surface where they are oxidised, recovering almost completely the ex-

pected carrier concentration[1]. More information on the details of the out-diffusion of manganese interstitials due to annealing can be found here: [12],[13].

1.2.5 Ferromagnetism

The ions of gallium and arsenic in crystalline GaAs have no unpaired electrons (table 1.1) and therefore have no net magnetic moment. The ferromagnetism in (Ga,Mn)As comes from the manganese ions which have half-filled `d` shells. Closely-neighbouring manganese ions couple antiferromagnetically but the separation between manganese ions in typical (Ga,Mn)As films is too great for direct manganese-manganese interactions — for example the average manganese separation in 5% (Ga,Mn)As is of the order of 1 nm. Instead the magnetic order is mediated by the itinerant holes which couple antiferromagnetically with the manganese ions, resulting in a long-range ferromagnetic arrangement of the manganese moments. Each substitutional manganese ion provides a moment of approximately 4 Bohr magnetons (μ_B) (this is made up of $5\mu_B$ from the five electrons in the `d` shell minus $1\mu_B$ from one hole coupled antiferromagnetically) whereas interstitials provide around $-3\mu_B$ (which comes from $-5\mu_B$ from the ion coupled antiferromagnetically with a substitutional minus ($-2\mu_B$) from the removal of two holes) [14]. Once again interstitials are detrimental to the ferromagnetism but post-growth annealing allows us to recover the moment density, as with the carrier concentration. For a sample with 5% manganese all in substitutional positions, $4\mu_B$ per ion would correspond to a volume magnetization of 40 emu/cm^3 which is exactly what is found for 5% samples after annealing, whereas it can be as low as 30 emu/cm^3 before annealing.

[1] For samples with up to 8% substitutional manganese content, as far as we know *all* of the interstitials out-diffuse during annealing. For higher concentrations we find that the expected moment density is not recovered in full, which means that not all of the interstitials out-diffuse and/or another self-compensation mechanism comes into play [7].

Domain size

By showing that the behaviour of macroscopic (Ga,Mn)As samples fits single-domain models we know that this material can be single-domain even for samples as large as several millimeters by several millimeters [15]. This is in contrast to dense-moment systems which tend to have much smaller domain sizes, and is important for the work I will present in the following chapters.

1.2.6 Curie Temperature

Theory based on the *mean field Zener model* predicted in 2000 that the Curie temperature in (Ga,Mn)As scales as $T_C \propto x \cdot p^{1/3}$ where x is the percentage of manganese and p is the hole concentration [16]. The corresponding prediction for room-temperature ferromagnetism was that 10% manganese should give $T_C \approx 300$ K. Recently, more sophisticated theory has again predicted an approximately-linear scaling of T_C with x and a weak dependence on hole concentration [14]. After the first successful growth of ferromagnetic (Ga,Mn)As in 1996 with a Curie temperature of around 60 K [17], the record T_C steadily rose over the next few years to 110 K following improvements in growth techniques, a temperature where it plateaued for some considerable time. This was at first believed to be a fundamental limit [18] but is now understood to have been due to self-compensation mechanisms, specifically manganese interstitials. After the discovery of the effects of post-growth annealing this stepped quickly to 173 K [19], since when it has increased stepwise to ∼185 K after refinements in the growth and annealing processes [7]. Once more a limit seems to be being approached which is again attributed to self-compensation mechanisms — either due to not all interstitials being annealed out at high manganese concentrations and/or other compensating mechanisms occurring (e.g. arsenic antisites — see figure 1.2 — which are not so readily removed) [7]. Because of this, the prospects for (Ga,Mn)As as a candidate material for room-temperature devices are poor, at least for the foreseeable

future. Nevertheless (Ga,Mn)As remains an important testbed material for the reasons described above.

1.3 AMR and Magnetic Anisotropies in (Ga,Mn)As

1.3.1 Spin-orbit coupling

Both the Anisotropic Magnetoresistance and the magnetocrystalline anisotropy, which are the principles behind the bulk of this Thesis, are a result of the *Spin-Orbit Interaction* or *Spin-Orbit Coupling (SOC)*. At its simplest, this is the interaction between a particle's intrinsic, or spin, angular momentum **S** and its orbital angular momentum **L**.

An electron (or in our case a hole) orbiting a nucleus has angular momentum due to its orbit, as well as an intrinsic angular momentum which has become known as *spin*. A classical analogy is Earth orbiting the Sun. Our planet has an angular momentum due to its orbit and an angular momentum due to spinning on its North-South axis. Whilst there is no evidence that an electron has this conventional spin, Dirac showed that an electron has to be defined as a point particle with an intrinsic angular momentum, albeit one of unknown origin [20].

An external magnetic field will try to align the intrinsic angular momenta and due to the SOC this also attempts to align the orbital angular momenta. In a single crystal, however, this has to compete with the lattice-orbit interaction which tries to keep the orbits aligned to the underlying crystal structure. This is the origin of the magnetocrystalline anisotropy: most materials have weak SOC compared with the lattice-orbit energy so the energy required to overcome the SOC and realign the spins is small. Due to the SOC being strong in (Ga,Mn)As, it takes relatively high energy to realign the spins and hence the magnetocrystalline anisotropy is strong in this material. Similarly, the SOC is also responsible for the AMR which is the transport-equivalent of the magnetocrystalline anisotropy. Starting from the SOC, many of the

anisotropic properties of (Ga,Mn)As can be explained and predicted [21],[22].

1.3.2 AMR

Anisotropic Magnetoresistance is a well-established and technologically important effect which has been used in devices such as magnetic recording elements, bubble memory and field sensors since the 1970s [23],[24]. It manifests itself as a variation in resistance in magnetized samples as the orientation of the magnetization is changed with respect to the current direction. A direct result of the spin-orbit coupling, it is due to a higher probability of s–d scattering occurring when the current is parallel to the magnetization; therefore the resistance is highest when the magnetization is parallel to the current and lowest when it is perpendicular. The magnitude of the AMR, defined in chapter 2, can be almost 20% in permalloy [25] and has recently been reported to be as much as 50% in uranium compounds [26]. Such large changes in resistance provide useful device functionality.

Recent effects reported in (Ga,Mn)As have been attributed to originate from AMR and yet there has until now been no systematic study of AMR in this material; such a study provides the basis for chapter 2. Further details are given in the introduction to that chapter.

1.3.3 Magnetic Anisotropies

Definitions

Throughout this report I define the [001] crystallographic direction as being the direction normal to the growth surface. *Biaxial* refers to general four-fold symmetry with the specific case of 90° symmetry along the [100] and [010] directions being termed *cubic*. This is illustrated in figure 1.3.

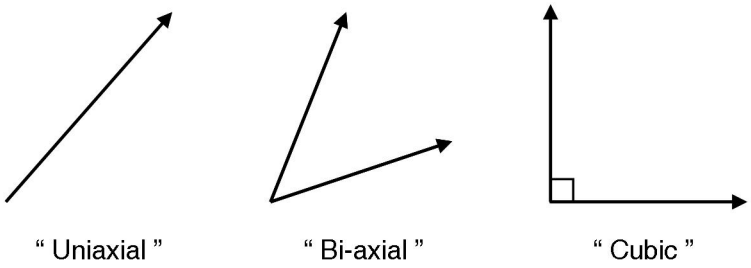

Fig. 1.3 — Definitions of in-plane easy-axis configurations used in this report.

Growth strain and lattice mismatch

During MBE-growth of single-crystal (Ga,Mn)As on a GaAs substrate there is a lattice mismatch between the substrate and the (Ga,Mn)As layer. Although manganese atoms have fewer electrons than both gallium and arsenic atoms (table 1.1), both substitutional and interstitial manganese increase the lattice parameter of GaAs. Thus unstrained (Ga,Mn)As has a larger lattice parameter than unstrained GaAs, even for concentrations of manganese as small as a few percent. For example, the lattice parameter of unstrained ($Ga_{0.95}$,$Mn_{0.05}$)As is approximately 0.1-0.2% larger than unstrained GaAs, as measured by X-ray diffraction [27]. Consequently, a thin (Ga,Mn)As film will be under in-plane compressive strain, as illustrated in figure 1.4. Although the difference in lattice parameter between the film and substrate is tiny, it is enough to dictate in the broadest sense the anisotropy of the film. It is well established that compressively-strained (Ga,Mn)As films exhibit magnetic anisotropy which is all in the plane of the film whilst tensile-strained films are dominated by a perpendicular-to-plane component [28].

All of the (Ga,Mn)As films in this Thesis were grown on GaAs substrates and therefore incorporate compressive growth strain and exhibit in-plane anisotropy. Details of the in-plane anistropies, which are characterized by a competition between a uniaxial anisotropy along the [$\bar{1}$10] direction and a cubic anisotropy along [100] and [010], are covered on the following pages. As a matter of interest, growing an (In,Ga)As buffer layer between the GaAs substrate and (Ga,Mn)As thin film causes

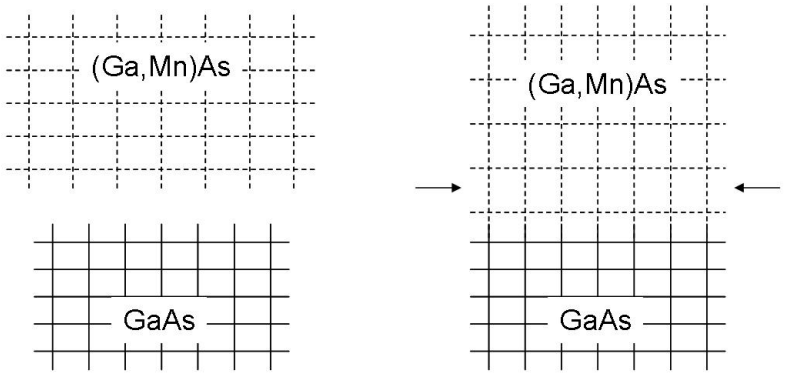

Fig. 1.4 — Left: Fully relaxed (Ga,Mn)As has a larger lattice constant than fully relaxed GaAs. Right: A thin (Ga,Mn)As film grown on a thick GaAs substrate will incorporate in-plane, symmetric, compressive strain, often referred to as *growth strain*.

tensile strain of the thin film and therefore out-of-plane anisotropy, since (In,Ga)As has a larger lattice constant than both GaAs and (Ga,Mn)As.

The magnetic anisotropies in a ferromagnetic material can be of three different types — shape, strain and, for crystalline materials, magnetocrystalline. I will show later that the shape anisotropy is very small in low-moment (Ga,Mn)As, whilst investigating effects related to the other two anisotropies forms the backbone of chapters 3 and 4.

Shape Anisotropy

Shape anisotropy is a magnetic anisotropy which exists for any non-spherical magnetic domain. For a single-domain sample magnetized along a particular direction, magnetic poles form at the sample's edges which create a field that acts in a direction opposing the internal magnetization — this is the *demagnetizing field*. For a spherical sample the size of the demagnetizing field will be the same for any orientation of the internal magnetization due to symmetry. Conversely, for a long, thin sample the demagnetizing field is much stronger when the magnetization lies across the axis of the sample than when magnetized along it; the long axis is therefore a strongly-preferred direction for the magnetization and there is a distinct magnetic easy axis along the main axis. For

any sample of anisotropic shape there will be an anisotropy of the demagnetizing field and the further from spherical the sample the stronger the effect.

The strength of the demagnetizing field, and therefore the shape anisotropy, depends on two things — the *demagnetizing factor* and the square of the net magnetization of the sample. The demagnetizing factor is a coefficient between zero and one which determines the preferred direction for the magnetization. For example for a cube it is 1/3 along each of the three orthogonal axes whereas for a wire it is ~ 0 along the length of the wire and ~ 1 in the directions perpendicular to the length of the wire, which determines the main physical axis as the magnetic easy axis[2]. However, since the magnetic moment density in (Ga,Mn)As is small (typically of the order of 40 emu/cm^3), the shape anisotropy turns out to be insignificant for all the samples used in this Thesis, as I will show in chapter 3.

Magnetocrystalline Anisotropy

The cubic symmetry of the (Ga,Mn)As lattice provides a cubic term in the magnetocrystalline energy landscape, with energy minima along the [100] and [010] directions. For compressively-strained films, this and a uniaxial term along the [$\bar{1}$10] direction together dominate the magnetocrystalline anisotropy. The origin of the uniaxial term is unknown but if an artificial anisotropic shear strain along this direction is added into calculations the magnetic anisotropy is reproduced [29]. Despite this, X-ray investigations which have specifically sought to measure a uniaxial strain in (Ga,Mn)As have failed to find one [30],[31]. Although bulk GaAs comprises no uniaxial asymmetry (figure 1.2), during epitaxial growth the Ga-Ga bonds at the surface of the substrate will run either along [110] or [$\bar{1}$10], and it has been suggested that this anisotropy can be incorporated into the growth of subsequent epitaxial layers [30].

In fact, further contributions to the magnetic anisotropy have also emerged but are generally much weaker. The magnetocrystalline anisotropy is discussed in greater

[2] This, incidentally, is why it is not trivial to manufacture fridge magnets.

detail in the introduction to chapter 3.

Strain Anisotropy

Finally, strain anisotropy occurs for any sample which undergoes a physical strain that is anisotropic in nature. I discussed earlier in this section how thin (Ga,Mn)As films grown on relaxed GaAs substrates incorporate in-plane symmetric, compressive growth strain and this causes the magnetic anisotropies to be dominated by competing in-plane contributions. By physically patterning (Ga,Mn)As samples it is possible to allow the growth strain to relax in a controlled manner, which forms the basis for chapter 3. I will show in that chapter that strain relaxations even as small as 10^{-4} can cause remarkably strong modifications to the magnetic energy landscape in thin-film (Ga,Mn)As samples.

Typical anisotropy in compressively-strained, ~5% (Ga,Mn)As thin films

I have described how the magnetic anisotropy in the samples used in this Thesis is characterized by in-plane contributions from a uniaxial [$\bar{1}$10] term and a cubic [100]-[010] term. From a large collection of (Ga_{1-x},Mn_x)As samples where x is a few percent, grown and measured by several groups worldwide including our own, it is well known that details vary greatly from one to the next, even amongst nominally-identical samples; this is due in part to the sensitive dependence of the anisotropy on hole concentration and strain. Consistently, however, the cubic anisotropy has a stronger temperature dependence than the uniaxial. Because of this, all samples tend to be uniaxial as they approach T_C; however, as we go down in temperature and the cubic anisotropy becomes stronger faster than the uniaxial, we sometimes see a crossover after which the cubic term dominates, whereas in other samples we find that the uniaxial remains dominant right down to the lowest temperatures. Furthermore, since the hole concentration can be greatly increased by post-growth annealing (see section 1.2.4), there can be big differences between the magnetocrystalline anisotropies

of a sample as-grown and after annealing.

Manipulation of Magnetic Anisotropy

The ability to manipulate the magnetic anisotropy of a sample is potentially of use in operational devices. Due to the dependence of the anisotropy on hole concentration, manganese incorporation, temperature and strain there are several mechanisms for global control of the anisotropy of a whole sample. For example, during MBE the grower can choose different substrates to provide particular strain in the sample and can control to some extent the manganese concentration which determines the hole concentration and moment density. It is also straightforward to control the sample thickness which relates to the degree of strain relaxation. After growth the samples can be annealed for various periods of time to bring about further sample-wide changes to the energy landscape.

More useful, however, is the ability to manipulate the anisotropy of a very specific region of a sample. Such control can be achieved by allowing local relaxation of the incorporated growth strain through physical patterning of the samples, which forms the basis of chapter 3.

1.4 Thesis

This Thesis is sectioned into three main parts. In chapter 2 I present a systematic study of the Anisotropic Magnetoresistance in 5 nm (Ga,Mn)As films, which complements a previous study by our group on 25 nm films. Together these comprise the first such study in this material system and I will show that a uniaxial crystalline component can dominate the AMR, the first material system to our knowledge in which this has been seen. This leads directly onto a study of the magnetocrystalline anisotropy which is the magnetometry analogy of the AMR. Chapter 3 comprises a study of the effects on the magnetic anisotropy of patterning narrow stripes in (Ga,Mn)As

films, which allows the incorporated growth strain to relax in a direction perpendicular to the stripes. The results show that we are able to manipulate the anisotropy with stripes as wide as 1 µm, in one case rotating the easy axis through 90° which is equivalent to switching the orientations of the easy and hard axes of the un-patterned material. In the following chapter I present a new technique based on the magnetic susceptibility to locate the Spin Reorientation Transition, the temperature at which the cubic and uniaxial anisotropy components are equal. Conventionally measured by A.C. SQUID magnetometry, I show that the same results can be qualitatively reproduced in much simpler measurements based on the AMR.

References

[1] M. N. Baibich, J. M. Broto, A. Fert, F. Nguyen Van Dau, F. Petroff, P. Eitenne, G. Creuzet, A. Friederich, and J. Chazelas, "Giant magnetoresistance of (001)Fe/(001)Cr magnetic superlattices," *Physical Review Letters*, vol. 61, p. 2472, 1988.

[2] G. Binasch, P. Grünberg, F. Saurenbach, and W. Zinn, "Enhanced magnetoresistance in layered magnetic structures with antiferromagnetic interlayer exchange," *Physical Review B*, vol. 39, p. 4828, 1989.

[3] S. A. Wolf, D. D. Awschalom, R. A. Buhrman, J. M. Daughton, S. von Molnár, M. L. Roukes, A. Y. Chtchelkanova, and D. M. Treger, "Spintronics: A Spin-Based Electronics Vision for the Future," *Science*, vol. 294, p. 1488, 2001.

[4] G. A. Prinz, "Magnetoelectronics," *Science*, vol. 282, p. 1660, 1998.

[5] D. D. Awschalom, M. E. Flatté, and N. Samarth, "Spintronics," *Scientific American*, p. 53, May 2002.

[6] H. Ohno, H. Munekata, T. Penney, S. von Molnár, and L. L. Chang, "Magnetotransport properties of p-type (In,Mn)As diluted magnetic III-V semiconductors," *Physical Review Letters*, vol. 68, pp. 2664–2667, 1992.

[7] M. Wang, R. P. Campion, A. W. Rushforth, K. W. Edmonds, C. T. Foxon, and B. L. Gallagher, "Achieving High Curie Temperature in (Ga,Mn)As," *Applied Physics Letters*. (In press). arXiv:0808.1464v1 [cond-mat.mtrl-sci].

[8] C. Kittel, *Introduction to Solid State Physics*. Wiley & Sons, sixth ed. p. 429.

[9] B. A. Joyce, D. D. Vvedensky, and C. T. Foxon, *Handbook on Semiconductors*, ch. 4. (Growth Mechanisms in MBE and CBE of III-V Compounds), p. 275. Elsevier Science, 1994.

[10] R. P. Campion, K. W. Edmonds, L. X. Zhao, K. Y. Wang, C. T. Foxon, B. L. Gallagher, and C. R. Staddon, "High-quality GaMnAs films grown with arsenic dimers," *Journal of Crystal Growth*, vol. 247, pp. 42–48, January 2003.

[11] R. P. Campion, K. W. Edmonds, L. X. Zhao, K. Y. Wang, C. T. Foxon, B. L. Gallagher, and C. R. Staddon, "The growth of GaMnAs films by molecular beam epitaxy using arsenic dimers," *Journal of Crystal Growth*, vol. 251, pp. 311–316, April 2003.

[12] K. W. Edmonds, P. Bogusławski, K. Y. Wang, R. P. Campion, S. N. Novikov, N. R. S. Farley, B. L. Gallagher, C. T. Foxon, M. Sawicki, T. Dietl, M. Buongiorno Nardelli, and J. Bernholc, "Mn interstitial diffusion in (Ga,Mn)As," *Physical Review Letters*, vol. 92, p. 037201, Jan 2004.

[13] S. J. Potashnik, K. C. Ku, S. H. Chun, J. J. Berry, N. Samarth, and P. Schiffer, "Effects of annealing time on defect-controlled ferromagnetism in $Ga_{1-x}Mn_xAs$," *Applied Physics Letters*, vol. 79, no. 10, pp. 1495–1497, 2001.

[14] T. Jungwirth, J. Sinova, J. Mašek, J. Kučera, and A. H. MacDonald, "Theory of ferromagnetic (III,Mn)V semiconductors," *Reviews of Modern Physics*, vol. 78, no. 3, pp. 809–864, 2006.

[15] H. X. Tang, R. K. Kawakami, D. D. Awschalom, and M. L. Roukes, "Giant planar hall effect in epitaxial (Ga,Mn)As devices," *Physical Review Letters*, vol. 90, p. 107201, Mar 2003.

[16] T. Dietl, H. Ohno, F. Matsukura, J. Cibert, and D. Ferrand, "Zener model description of ferromagnetism in zinc-blende magnetic semiconductors," *Science*, vol. 287, p. 1019, 2000.

[17] H. Ohno, A. Shen, F. Matsukura, A. Oiwa, A. Endo, S. Katsumoto, and Y. Iye, "(Ga,Mn)As: A new diluted magnetic semiconductor based on GaAs," *Applied Physics Letters*, vol. 69, no. 3, pp. 363–365, 1996.

[18] K. M. Yu, W. Walukiewicz, T. Wojtowicz, I. Kuryliszyn, X. Liu, Y. Sasaki, and J. K. Furdyna, "Effect of the location of Mn sites in ferromagnetic $Ga_{1-x}Mn_xAs$ on its Curie temperature," *Physical Review B*, vol. 65, p. 201303, 2002.

[19] K. Y. Wang, R. P. Campion, K. W. Edmonds, M. Sawicki, T. Dietl, C. T. Foxon, and B. L. Gallagher, "Magnetism in (Ga,Mn)As Thin Films With T_C Up To 173K," *ICPS-27 Proceedings*, vol. 772, pp. 333–334, 2005.

[20] A. I. M. Rae, *Quantum Mechanics*. Institute of Physics Publishing, 3rd ed. Chapter 5.

[21] T. Dietl, H. Ohno, and F. Matsukura, "Hole-mediated ferromagnetism in tetrahedrally coordinated semiconductors," *Physical Review B*, vol. 63, p. 195205, Apr 2001.

[22] M. Abolfath, T. Jungwirth, J. Brum, and A. H. MacDonald, "Theory of magnetic anisotropy in $III_{1-x}Mn_xV$ ferromagnets," *Phys. Rev. B*, vol. 63, p. 054418, Jan 2001.

[23] T. R. McGuire and R. I. Potter, "Anisotropic Magnetoresistance in Ferromagnetic 3d Alloys," *IEEE Transactions on Magnetics*, vol. 11, no. 4, pp. 1018–1038, 1975.

[24] D. A. Thompson, L. T. Romankiw, and A. F. Mayadas, "Thin Film Magnetoresistors in Memory, Storage, and Related Applications," *IEEE Transactions on Magnetics*, vol. 11, no. 4, pp. 1039–1050, 1975.

[25] I. A. Campbell, A. Fert, and O. Jaoul, "The spontaneous resistivity anisotropy in Ni-based alloys," *Journal of Physics C*, vol. 3, p. S95, May 1970.

[26] P. Wiśniewski, "Giant anisotropic magnetoresistance and magnetothermopower in cubic 3:4 uranium pnictides," *Applied Physics Letters*, vol. 90, no. 19, p. 192106, 2007.

[27] L. X. Zhao, C. R. Staddon, K. Y. Wang, K. W. Edmonds, R. P. Campion, B. L. Gallagher, and C. T. Foxon, "Intrinsic and extrinsic contributions to the lattice parameter of GaMnAs," *Applied Physics Letters*, vol. 86, no. 7, p. 071902, 2005.

[28] H. Ohno, "Making nonmagnetic semiconductors ferromagnetic," *Science*, vol. 281, p. 951, 1998.

[29] M. Sawicki, K.-Y. Wang, K. W. Edmonds, R. P. Campion, C. R. Staddon, N. R. S. Farley, C. T. Foxon, E. Papis, E. Kaminska, A. Piotrowska, T. Dietl, and B. L. Gallagher, "In-plane uniaxial anisotropy rotations in (Ga,Mn)As thin films," *Physical Review B*, vol. 71, no. 12, 2005.

[30] U. Welp, V. K. Vlasko-Vlasov, A. Menzel, H. D. You, X. Liu, J. K. Furdyna, and T. Wojtowicz, "Uniaxial in-plane magnetic anisotropy of $Ga_{1-x}Mn_xAs$," *Applied Physics Letters*, vol. 85, no. 2, pp. 260–262, 2004.

[31] U. Welp, V. K. Vlasko-Vlasov, X. Liu, J. K. Furdyna, and T. Wojtowicz, "Magnetic Domain Structure and Magnetic Anisotropy in $Ga_{1-x}Mn_xAs$," *Physical Review Letters*, vol. 90, no. 16, pp. 167206/1–4, 2003.

Chapter 2

Anisotropic Magnetoresistance Studies of Gallium Manganese Arsenide Thin Films

2.1 Introduction and Motivation

The Anisotropic Magnetoresistance (AMR) effect is of great historical importance having been used in technological applications since the 1970s. First discovered in 1857 [1], a clear understanding of the phenomenology of the AMR in ferromagnetic metals has long been well established which has enabled the implementation of devices such as magnetic recording elements, bubble memory and field sensors for several decades now [2],[3].

Despite its widespread implementation in ferromagnetic metals the AMR effect is poorly understood in ferromagnetic semiconductor systems. However, several new effects of potential technological significance have recently been reported in the ferromagnetic semiconductor gallium manganese arsenide, demanding a better understanding of AMR in this material. For example Tunnelling Anisotropic Magnetoresistance (TAMR) is an up-to-2,000% magnetoresistive effect in (Ga,Mn)As nanoconstrictions

offering potential memory and sensor device applications [4]; and Coulomb Blockade Anisotropic Magnetoresistance (CB-AMR) is an effect which can be implemented in transistor-type geometries which can be switched both magnetically (with an external field) and electrically (with a gate) [5]. The detailed origins of these effects are not well understood but are clearly due to the anisotropic response of (Ga,Mn)As and this has motivated us to perform a systematic study of the AMR in this material.

In this chapter I describe our transport measurements on Hall bar and Corbino disc (see figure 2.3) devices fabricated from 5nm (Ga,Mn)As thin films; this complements earlier recent measurements made by our group on 25nm films but shows interesting new results. In the 5nm films we find that a uniaxial, crystalline contribution dominates the AMR, whereas this has only ever been seen as a weakly-contributing term before, to our knowledge in any material system.

2.2 Theory

For a thin film of conducting, ferromagnetic material in an external magnetic field there is a magnetoresistive response comprising two parts. First is the ordinary response of the charge carriers to the external field via the Lorentz force (the ordinary isotropic magnetoresistance and Hall Effect) and second is the 'extraordinary' response to the internal magnetization, via the spin-orbit interaction. The extraordinary response can be further divided into two distinct coefficients, the *Anomalous* or *Extraordinary* Hall Effect and the AMR. The former has received much attention in ferromagnetic semiconductors and (Ga,Mn)As in particular has emerged as a testbed material for studies into this phenomenon [6],[7], but a detailed understanding of the nature and origins of the AMR effect in (Ga,Mn)As has been elusive.

Phenomenologically the AMR has crystalline and non-crystalline components. The crystalline components arise from the underlying crystallographic structure of the material whilst the non-crystalline components are due to the lowering of the symmetry

by the imposition of a specific current direction. From measurements on standard Hall bars orientated along different crystallographic directions we have separated out the crystalline and non-crystalline components. Subsequent measurements made on Corbino disks allowed us to measure the crystalline components directly, corroborating our Hall bar results.

Analysis of AMR was first performed by W. Döring in cubic nickel [8]. Extending the analysis to (Ga,Mn)As requires the consideration of the cubic [100]–[010] plus uniaxial [110] crystalline symmetry in this material (see chapter 1). For Hall bar measurements we can write the longitudinal AMR — that is the AMR along the length of the bar and, therefore, parallel to the current direction — as follows [9]:

$$\frac{\Delta\rho_{xx}}{\rho_{av}} = C_I cos2\varphi + C_U cos2\psi + C_C cos4\psi + C_{I,C} cos(4\psi - 2\varphi) \tag{2.1}$$

Here ρ_{xx} is the longitudinal resistivity for a given orientation of the in-plane magnetic field, $\Delta\rho_{xx} = \rho_{xx} - \rho_{av}$ and ρ_{av} is the measured ρ_{xx} averaged over 360°. φ is the angle between the external magnetic field and the current direction and ψ is the angle between the magnetic field and the [110] crystal axis (figure 2.1). The four terms in equation 2.1 are therefore a non-crystalline term (C_I), a uniaxial and a cubic crystalline term (C_U and C_C respectively) and a crossed non-crystalline/cubic-crystalline term ($C_{I,C}$). Higher-order crystalline and crossed terms exist but have been omitted as their contributions turn out to be negligible in this analysis.

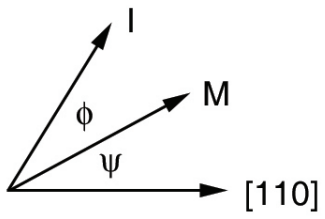

Fig. 2.1 — Angle designations in this chapter.

The transverse AMR, the AMR across the width of the bar and therefore perpendicular to the current direction, is given by equation 2.2; the purely crystalline terms are absent because of symmetry. ρ_{av} has the same meaning as above, i.e. it is still in terms of ρ_{xx}. At this point it is worth clarifying some terminology. The nomenclature adopted in this thesis is that equation 2.1 describes the *longitudinal AMR* and equation 2.2 the *transverse AMR*, which is also known as the *Planar Hall Effect*. Strictly speaking 'AMR' is an umbrella term covering both longitudinal and transverse AMR; in the literature a potential cause of confusion is that 'AMR' and 'longitudinal AMR' are sometimes used interchangeably.

$$\frac{\rho_{xy}}{\rho_{av}} = C_I sin2\varphi - C_{I,C} sin(4\psi - 2\varphi) \tag{2.2}$$

The crystalline terms in the longitudinal AMR can be extracted from measurements on orthogonal pairs of Hall bars. In theory this could be achieved with a pair along the [100] and [010] directions or a pair along the [110] and [$\bar{1}$10] directions (or indeed any other pair of orthogonal directions); in practice Hall bars were fabricated in all four of these directions. If we consider the [100]–[010] pair the crystalline terms can be extracted by combining the measurements as in equation 2.3. The non-crystalline terms drop out by symmetry — see Appendix A for the details.

$$\left[\left(\frac{\Delta\rho_{xx}}{\rho_{av}}\right)_{[100]} + \left(\frac{\Delta\rho_{xx}}{\rho_{av}}\right)_{[010]}\right]/2 = C_U cos2\psi + C_C cos4\psi \tag{2.3}$$

For the [110]–[$\bar{1}$10] pair a similar process can be followed:

$$\left[\left(\frac{\Delta\rho_{xx}}{\rho_{av}}\right)_{[110]} + \left(\frac{\Delta\rho_{xx}}{\rho_{av}}\right)_{[\bar{1}10]}\right]/2 = C_U cos2\psi + C_C cos4\psi \tag{2.4}$$

In the Corbino geometry the radial symmetry averages out the effects of the current direction (assuming high-quality fabrication) thus eliminating the non-crystalline AMR terms. Therefore measurements on Corbino disks yield the crystalline terms di-

rectly (equation 2.5), allowing us to corroborate the crystalline terms extracted from Hall bar measurements. Again, see Appendix A for the maths.

$$\frac{\Delta\rho_{corbino}}{\rho_{av}} = C_U cos2\psi + C_C cos4\psi \tag{2.5}$$

In thin, 25nm (Ga,Mn)As films the non-crystalline term C_I dominates the longitudinal AMR signal [9] whereas in ultra-thin, 5nm films we find that the uniaxial crystalline component C_U dominates over the whole temperature range, from 4K up to the Curie temperature. We believe this is the first time a uniaxial crystalline term has been found to dominate the AMR in any material.

2.3 Fabrication and Measurement

Measurements were made on high-quality, single-crystal ($Ga_{0.95}$,$Mn_{0.05}$)As thin films grown by low-temperature molecular beam epitaxy. The substrate was GaAs(001) which has a smaller lattice constant than (Ga,Mn)As so compressively strains the thin film; this creates an in-plane easy magnetic axis or axes (see chapter 1).

Optical lithography was used to fabricate our devices. Standard Hall bars 45µm wide and with voltage probes separated by 285µm were made along the [100], [010], [110] and [$\bar{1}$10] directions (figure 2.2) from adjacent pieces of the same parent wafer and Corbino disks were fabricated with an inner diameter of 800µm and an outer diameter of 1,400µm (figure 2.3).

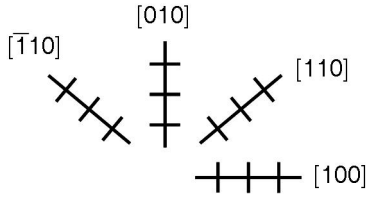

Fig. 2.2 — Hall bar orientations.

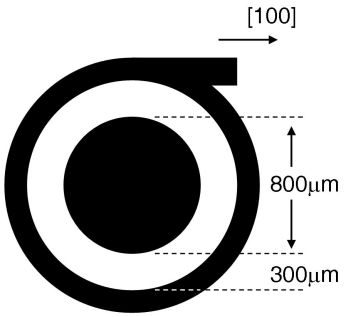

Fig. 2.3 — Corbino disk geometry.

Measurement

For each device an external magnetic field of 1T was applied in the plane of the thin film and rotated through 360° in the plane, in 3° steps. For the Corbino geometry the resistance of the device was recorded at fixed bias for a variety of temperatures, whilst for the Hall bars longitudinal and transverse resistances were recorded simultaneously. 1 Tesla was enough to saturate the magnetization for the majority of samples (determined from measurements of resistance against field strength); the exception was in high-resistance samples at the very lowest temperatures. For the Hall bar measurements it was important to use a consistent arrangement of voltage connections from sample to sample in order to measure the correct sign of the transverse AMR each time. The arrangement chosen is shown in figure 2.4 — with the positive terminal of the source voltage on the left hand side, V_{xy} is measured with the positive voltage probe at the bottom and the negative at the top. It is worth noting that V_{xx} and V_{xy} were measured on independent voltage probes. Some measurements were repeated with an external field of 500mT.

A helium-4 cryostat housed the measurement probe, with a rotary pump allowing us to lower the pressure and access temperatures down to 1.5 K. A heater under PID control allowed us to achieve relatively stable temperatures above 4K. For each sample, measurements were taken at a range of temperatures from 4K up to and sometimes exceeding the Curie Temperature. Measurements were made on the samples as grown, that is without having been annealed.

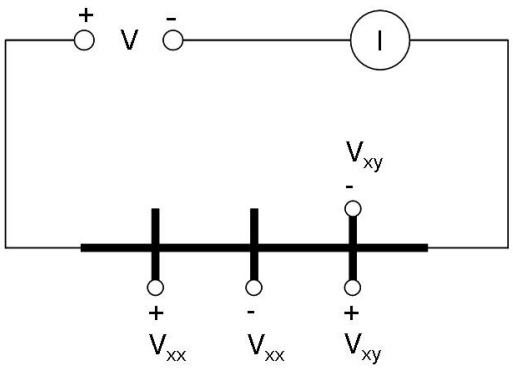

Fig. 2.4 — Hall bar measurement arrangement (Hall bar not to scale).

The longitudinal Hall bar resistances were determined by $R_{xx} = V_{xx}/I$; similarly for the transverse resistances. The longitudinal resistances were converted to resistances per square by dividing by 19/3, the number of squares between voltage probes in our Hall bar geometry.

Cooldown measurements

After inserting each sample into the cryostat, the resistance (longitudinal resistance in the case of the Hall bars) was recorded as the sample was cooled from room temperature down to ∼1.5K. The (longitudinal) resistance as a function of temperature is a useful tool as it provides a reasonable indication of the quality of the thin film. The cooldown curve can also provide an initial indication of the Curie temperature of the sample. Cooldowns were performed with a fixed bias of 1V and zero external magnetic field unless otherwise stated.

2.4 Results

2.4.1 Hall bars from wafer Mn292

Initial measurements were made on a set of as-grown Hall bars fabricated from wafer number Mn292, which comprised a 5nm ($Ga_{0.95}$,$Mn_{0.05}$)As film grown at Notting-

ham's MBE facility. The first measurements were on the bar along the [100] direction, followed by the bar along the [$\bar{1}$10] direction. Although these yielded good results the remaining Hall bars in the set were of such high resistance that it was not possible to make AMR measurements on them. Annealing the two high-resistance samples did not lead to a significant improvement. Since an orthogonal pair of Hall bars is required for the extraction of the crystalline coefficients, this set of devices was of limited use.

The cooldown curves for the four bars are shown in figure 2.5. Of some concern was the fact that there seemed to be two distinct resistance paths — a lower resistance path taken by the [100] and [$\bar{1}$10] bars and a higher resistance path for [010] and [110]. It could be problematic if there was a fundamental reason why two of the crystallographic directions should follow the same low resistance whilst the other directions were of the same high resistance. This would make comparing results from orthogonal Hall bars rather tricky. An alternative could be that there was a systematic variation in growth properties across the wafer, with the two low-resistance samples and the two high-resistance samples having come from two different regions of the wafer. Although the source of this problem remains unclear, the next set of samples proved much more straightforward.

2.4.2 Hall bars from wafer Mn293

A second set of four Hall bars was fabricated from a new 5nm wafer, number Mn293. The cooldowns for the four samples, as grown, are shown in figure 2.6. In this set of samples the four cooldown curves show remarkably good agreement with one another and the resistance is an order of magnitude lower over most of the temperature range. This allows us to conclude that any differences in the resulting AMR data can be attributed to the fact that the bars were made along different crystallographic directions. The resistance is $\sim$15MΩ at 4K, $\sim$250kΩ at 20K and $\sim$200kΩ at 30K — low enough for us to be able to make measurements down to low temperature ($\lesssim$4K).

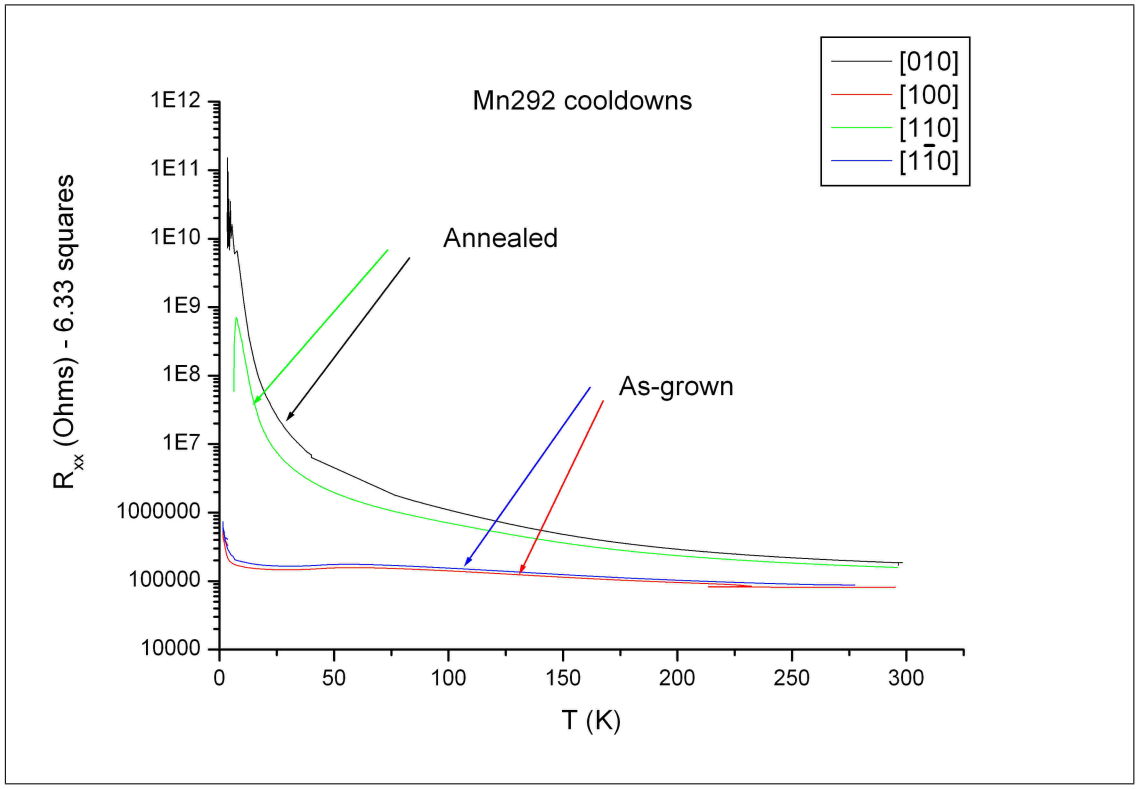

Fig. 2.5 — Cooldowns of four Hall bars fabricated from wafer number Mn292.

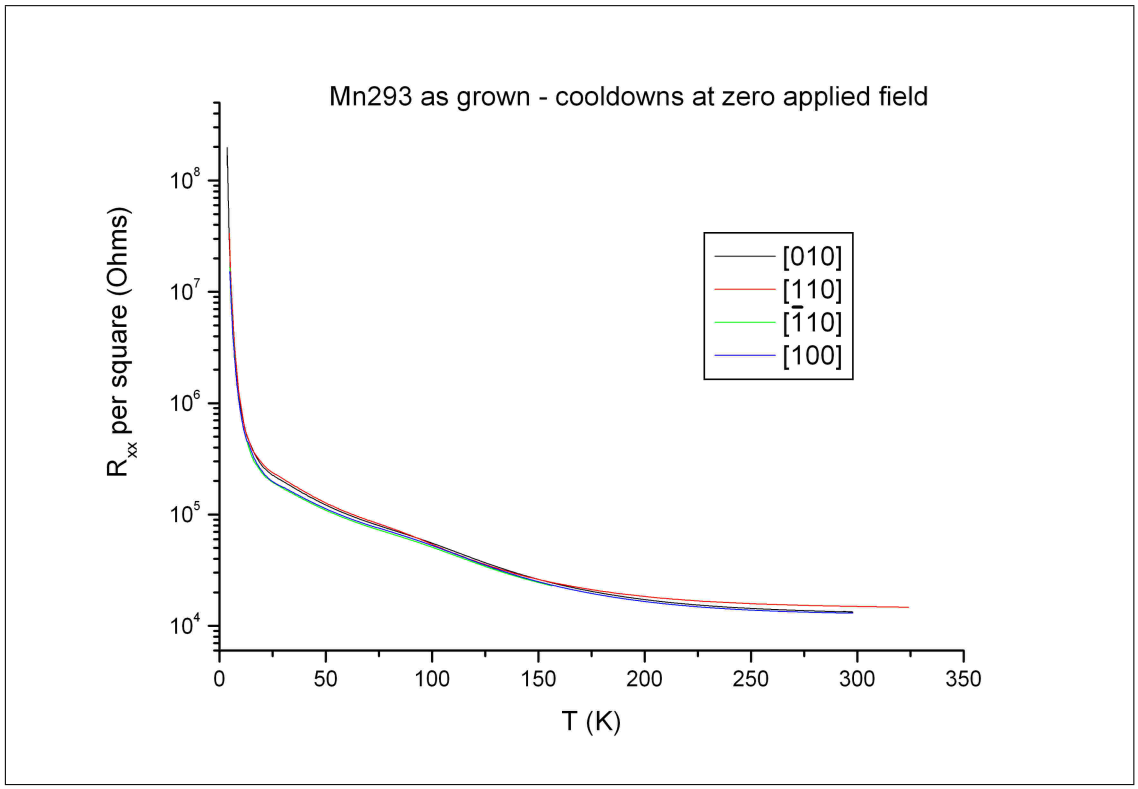

Fig. 2.6 — Cooldowns of four Hall bars fabricated from wafer number Mn293, as-grown.

In order for measurements to be truly as-grown it was necessary to make sure the fabrication of the devices was performed without any heating above a few tens of degrees Celsius. This required some unusual techniques — the resist was prepared without being baked (it was cured at room temperature for over 24 hours) and no metallic bond pads were deposited. Instead the bond wires were bonded directly to the (Ga,Mn)As surface, which has worked well.

Let us first consider the [010] Hall bar.

Mn293-[010] Hall bar

The first AMR measurements were made at 30K and at a variety of biases. The first of these — at 4V bias — is shown in figure 2.7. The phase of the R_{xx} curve is far from a simple $\cos 2\varphi$ dependence which indicates a strong contribution from the crystalline terms, rather than a dependence dominated by the $C_I \cos 2\varphi$ term. There could also be a small phase shift due to misalignment of the sample with respect to the external field but this is disguised by the shift caused by the non-crystalline terms; therefore one has to be careful how to remove such a phase shift before extracting the anisotropy coefficients from the data.

From equation 2.2 we would expect the R_{xy} curve to be centred on zero Ohms. The fact that it isn't is most likely to be due to mixing-in of R_{xx} data; this is caused by voltage probes on the Hall bar being of finite width and not absolutely perfectly aligned. Due to the large magnitude of R_{xx}, even a small amount of mixing can offset R_{xy} by the magnitude seen. Again this offset has to be carefully removed before extracting the AMR coefficients from the data.

No bias dependence was found in the 30K measurements so AMR measurements were made at biases of 300mV and 4V at temperatures ranging from 4K to 70K, with further biases of 1V, 2V and 3V at 30K. The sinusoidal variation of the resistance with φ indicates that the external field is enough to saturate the magnetization. This is in contrast to figure 2.8 which shows a measurement at 500mT, 4K and 4V bias

(along the [100] Hall bar); the strong deviation from sinusoidal dependence indicates that the weaker field is not saturating the magnetization.

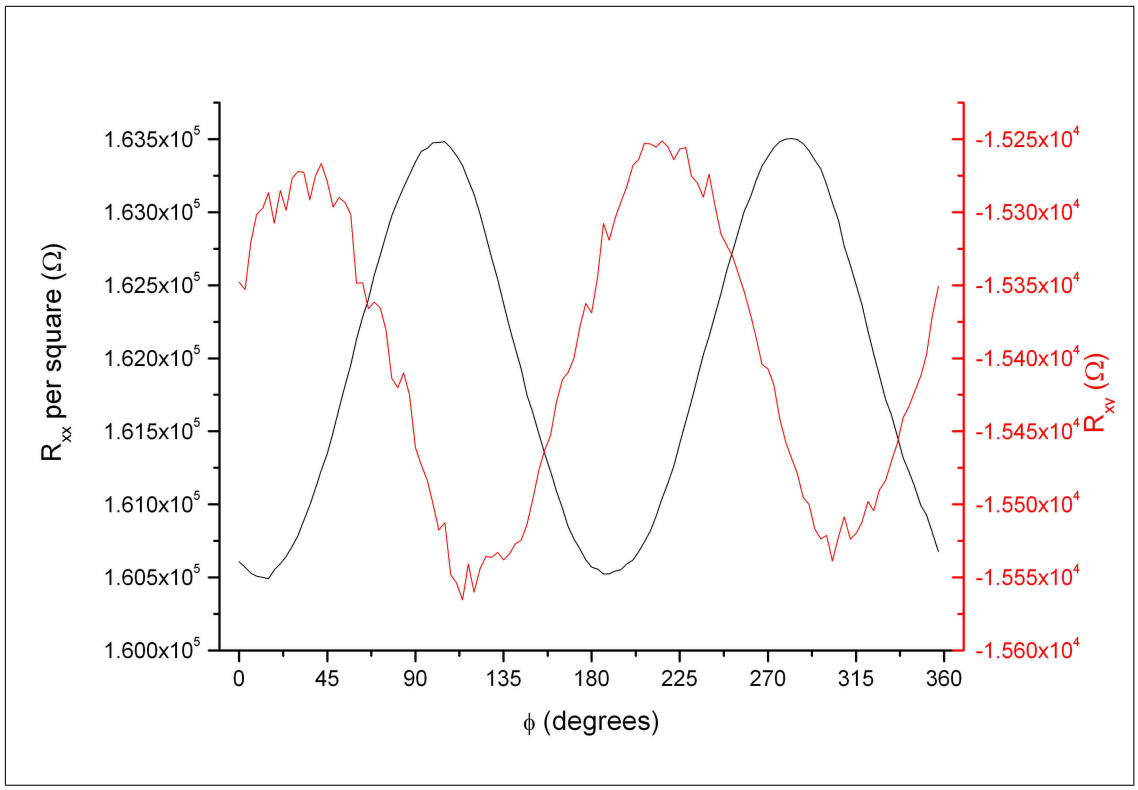

Fig. 2.7 — Longitudinal and transverse AMR for Mn293-[010], as-grown, at 30K and 4V bias.

The longitudinal AMR at 30K and 4V, defined as $\frac{\Delta\rho_{xx}}{\rho_{av}}$, is found to be 1.8% peak-to-peak (figure 2.7). The variation of longitudinal AMR with temperature is shown in figure 2.9 for all the biases. The independence of the AMR with respect to bias is strongly evident, as is the expected drop in the AMR as the temperature approaches the Curie temperature; of great interest is the sharp increase in the AMR as the temperature falls to $\lesssim$10K. The origin of this feature is as yet unexplained. This will be addressed after data from the remaining Hall Bars has been presented.

Mn293-[100] Hall bar

For the Hall bar fabricated along the [100] crystallographic direction, angular sweeps were made at 4V bias at temperatures ranging from 4K to 60K, with an external field

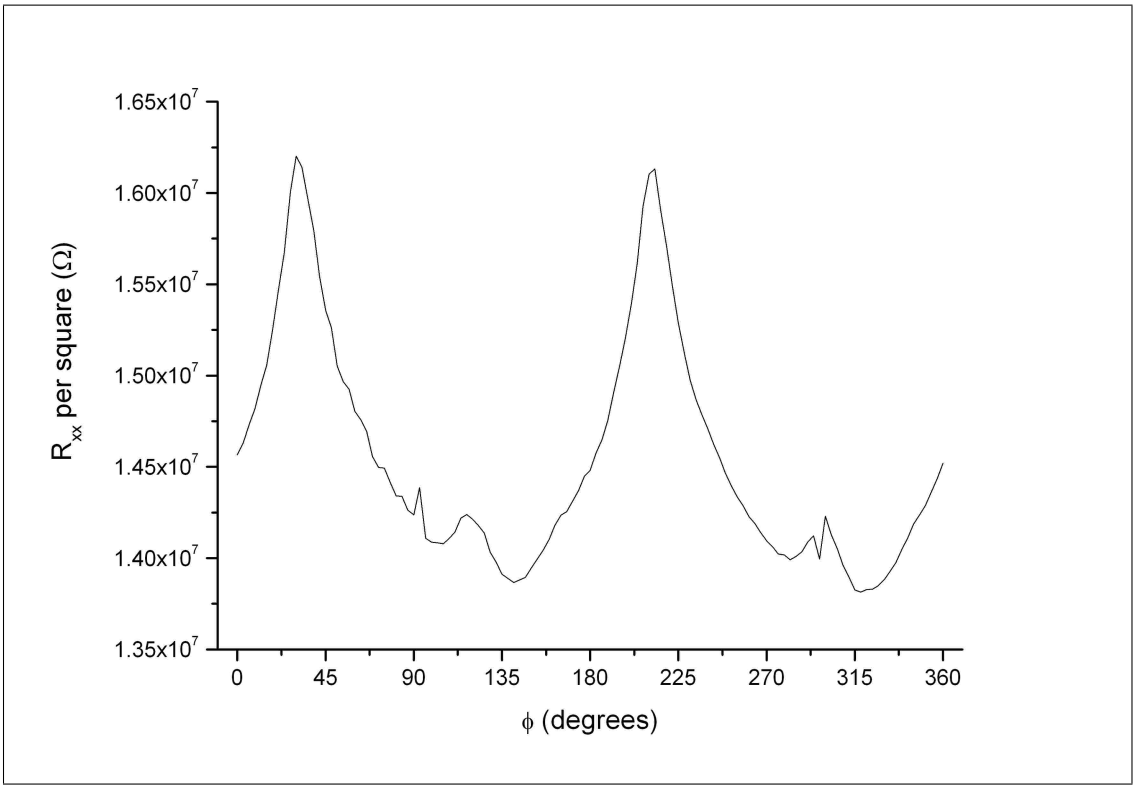

Fig. 2.8 — Longitudinal AMR for Mn293-[100], as-grown, at 4K, 4V bias and an external field of just 500mT. The weaker field is not enough to saturate the magnetization.

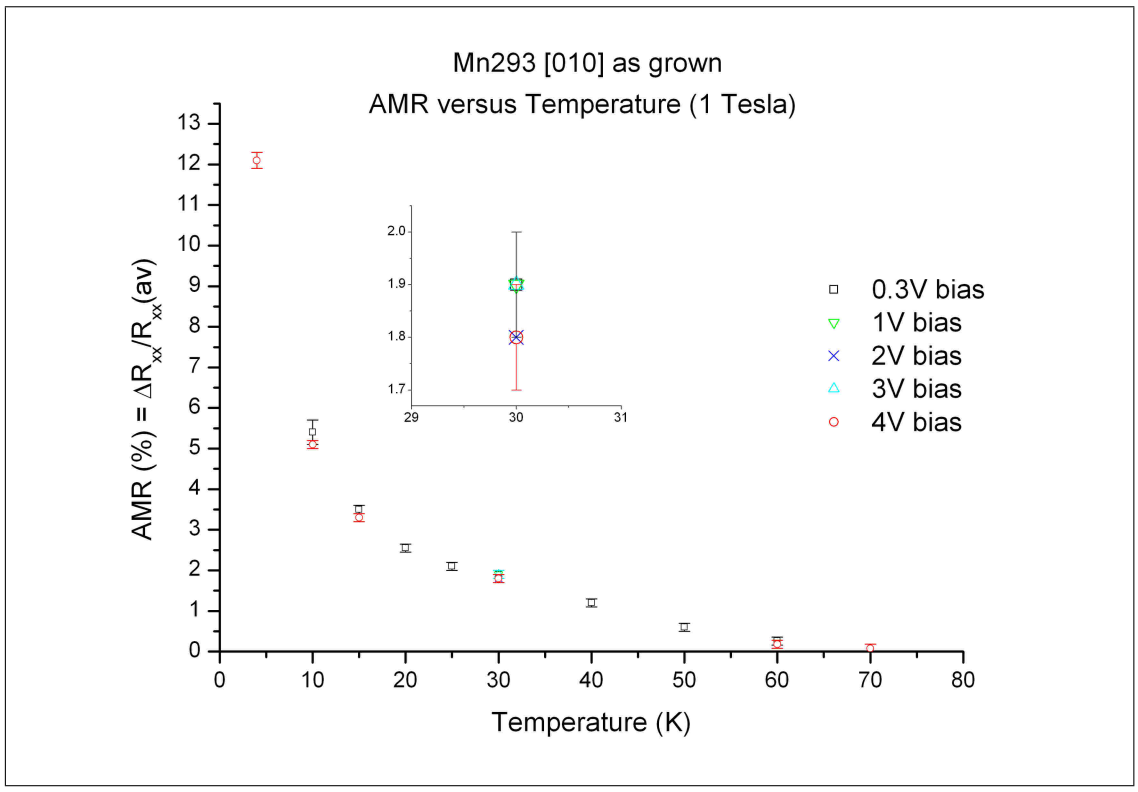

Fig. 2.9 — Longitudinal AMR as a function of temperature at various biases, for sample Mn293-[010], as-grown.

of 1T. Measurements were repeated at a field of 500mT for temperatures between 4K and 30K.

The AMR data taken at 30K, 4V bias and 1T are shown in figure 2.10. The transverse signal for this Hall bar is qualitatively the same as for the [010]-orientated bar; this is expected from the symmetry of equation 2.2. The longitudinal signals are phase-shifted, suggesting a significant contribution from the uniaxial crystalline term, $C_U cos2\psi$, in equation 2.1. The longitudinal AMR is again 1.8% peak-to-peak.

By combining the [010] and [100] data in the manner explained above (equation 2.3) we can extract the crystalline terms for 30K and 4V. The data is plotted in figure 2.11 and from the curve fit we obtain $C_U = 0.0069$ and $C_C = 0.00007$. The uniaxial term, C_U, is significantly larger than the cubic term, C_C (which is in fact zero within error at this temperature).

Pairs of data for the [010] and [100] Hall bars at 4V bias and 1T applied field also

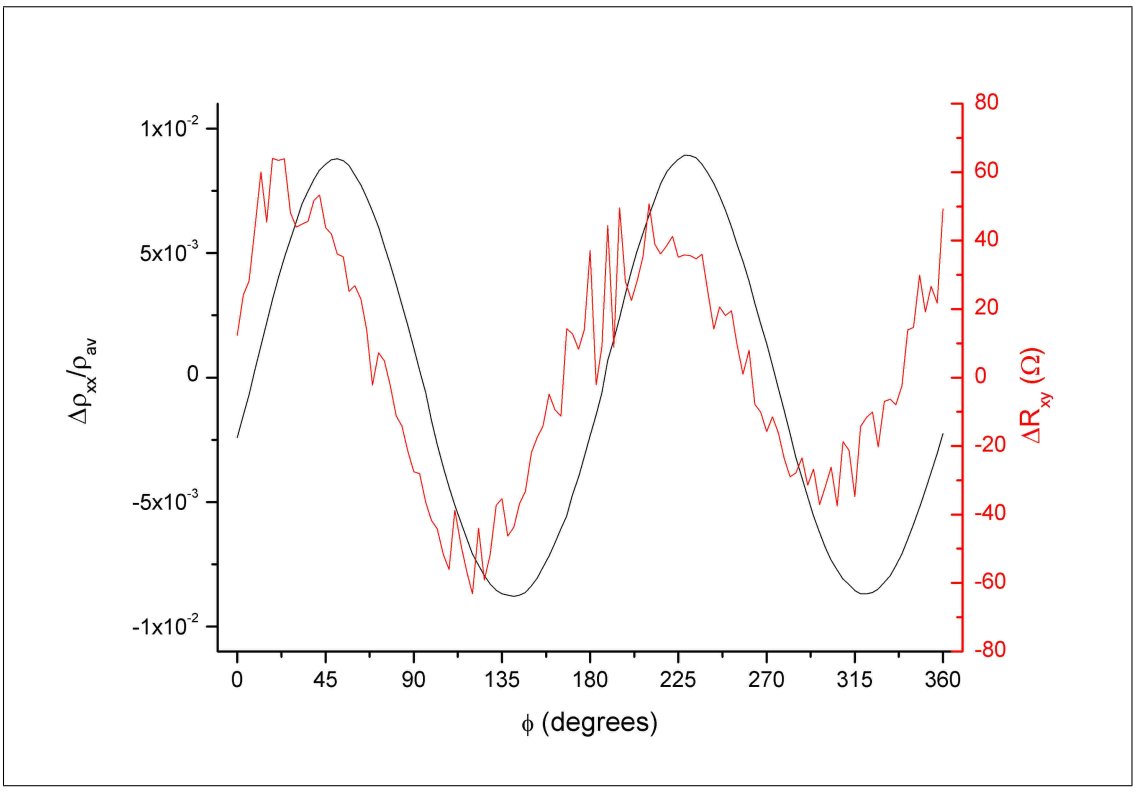

Fig. 2.10 — Longitudinal and transverse AMR for Mn293-[100], as-grown, at 30K, 4V bias and 1T field.

exist for temperatures of 4K, 10K and 15K. For these temperatures the crystalline AMR coefficients have been determined in the same manner as for 30K. The coefficients plotted as a function of temperature are shown in figure 2.12. We find that the uniaxial crystalline term dominates over the cubic term at all temperatures.

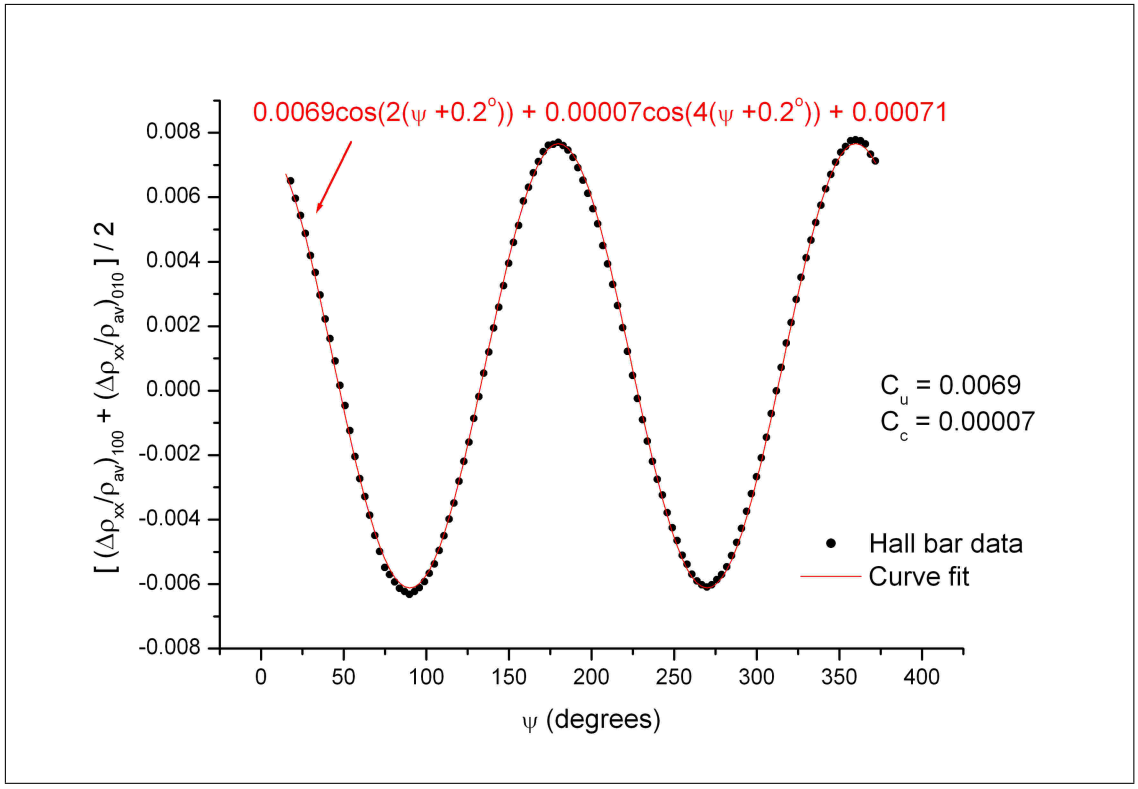

Fig. 2.11 — Crystalline terms extracted from [100]-[010] pair of Hall bars for MN293 as-grown, at 30K, 4V bias and 1T field.

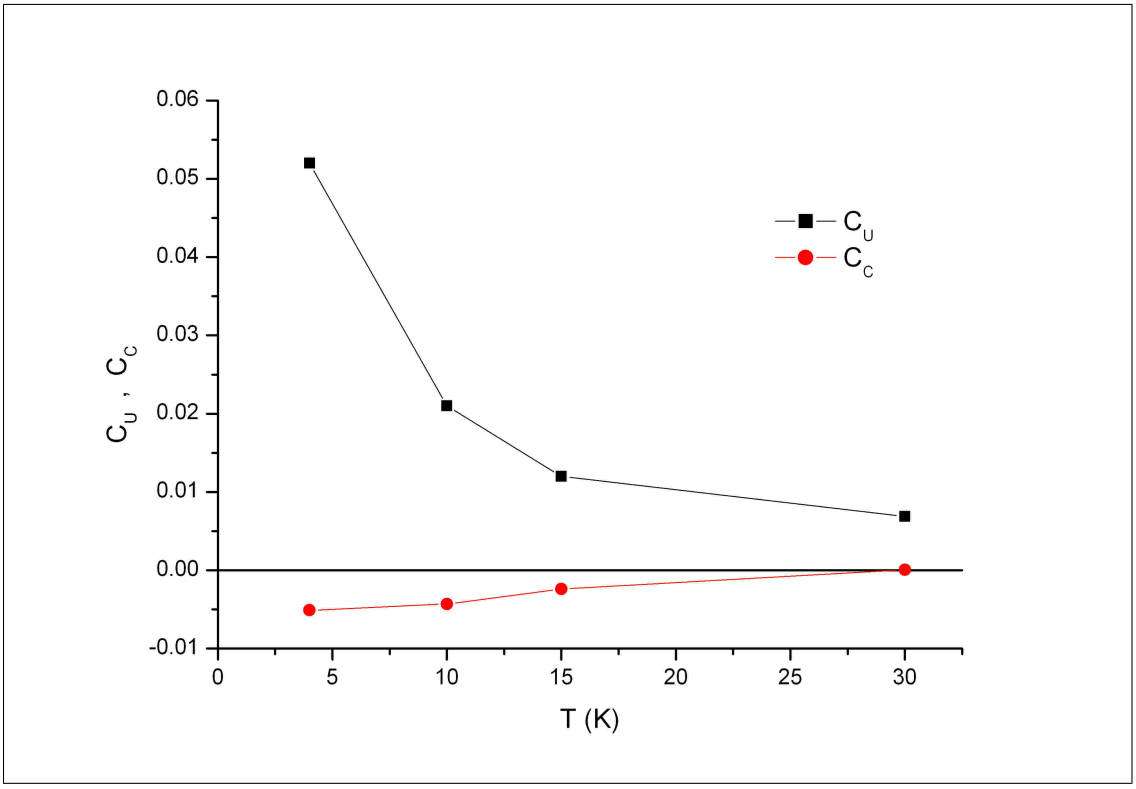

Fig. 2.12 — Crystalline terms versus temperature for [100]-[010] pair of Hall bars from Mn293 as-grown, at 4V bias and 1T field.

Mn293-[110] and Mn293-[$\bar{1}$10] Hall bars

The above process has been repeated for the other pair of orthogonal Hall bars. The angular sweeps for the [110] and [$\bar{1}$10] directions at 30K, 4V bias and 1T are shown in figures 2.13 and 2.14 respectively. R_{xy} is again qualitatively the same for the two curves as expected from equation 2.2. The longitudinal signals are again phase-shifted between the two directions which again suggests a significant contribution from the uniaxial crystalline term in equation 2.1. The longitudinal AMR is 1.5% − 1.6% peak-to-peak for both directions.

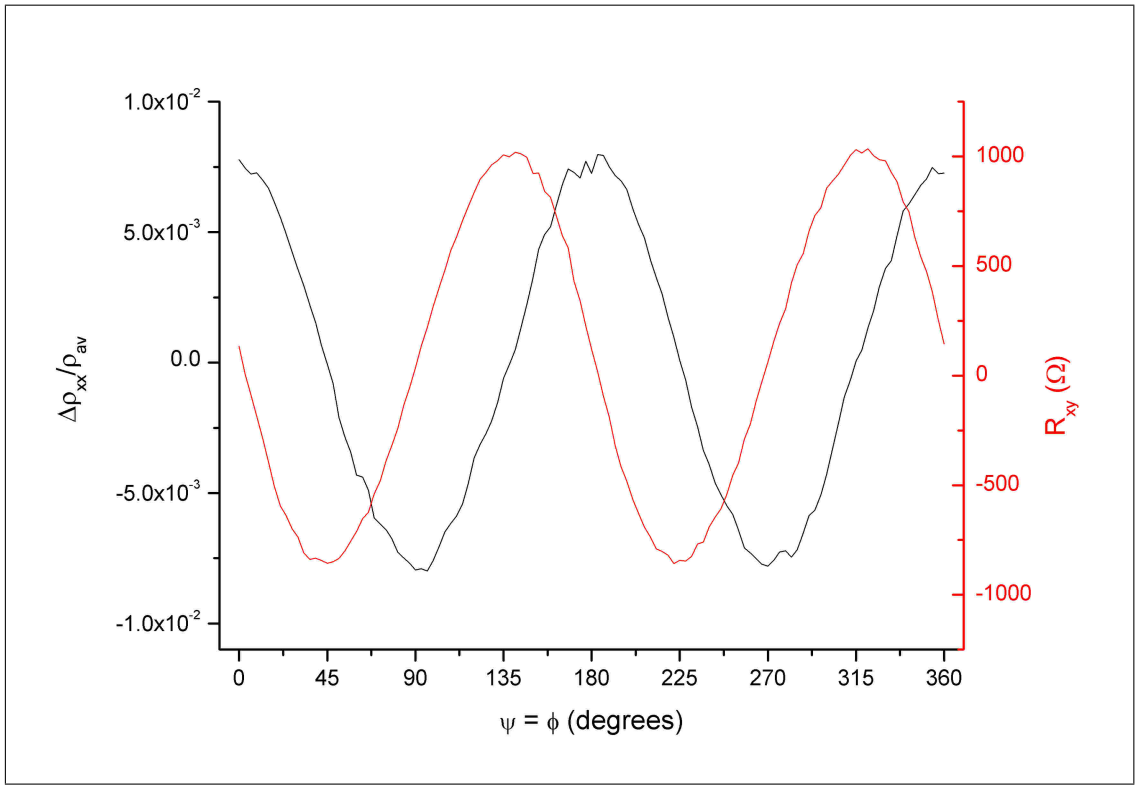

Fig. 2.13 — Longitudinal and transverse AMR for Mn293-[110], as-grown, at 30K, 4V bias and 1T field.

For the [110]-[$\bar{1}$10] pair of Hall bars we have equivalent data at the following temperatures: 4K, 10K, 20K, 30K, 40K and 50K. The crystalline coefficients have been extracted in the familiar manner and have been added to the data in figure 2.12, plotted in figure 2.16. Also in this figure are the non-crystalline terms C_I and $C_{I,C}$ which come from the R_{xy} data. The uniaxial term dominates at all temperatures.

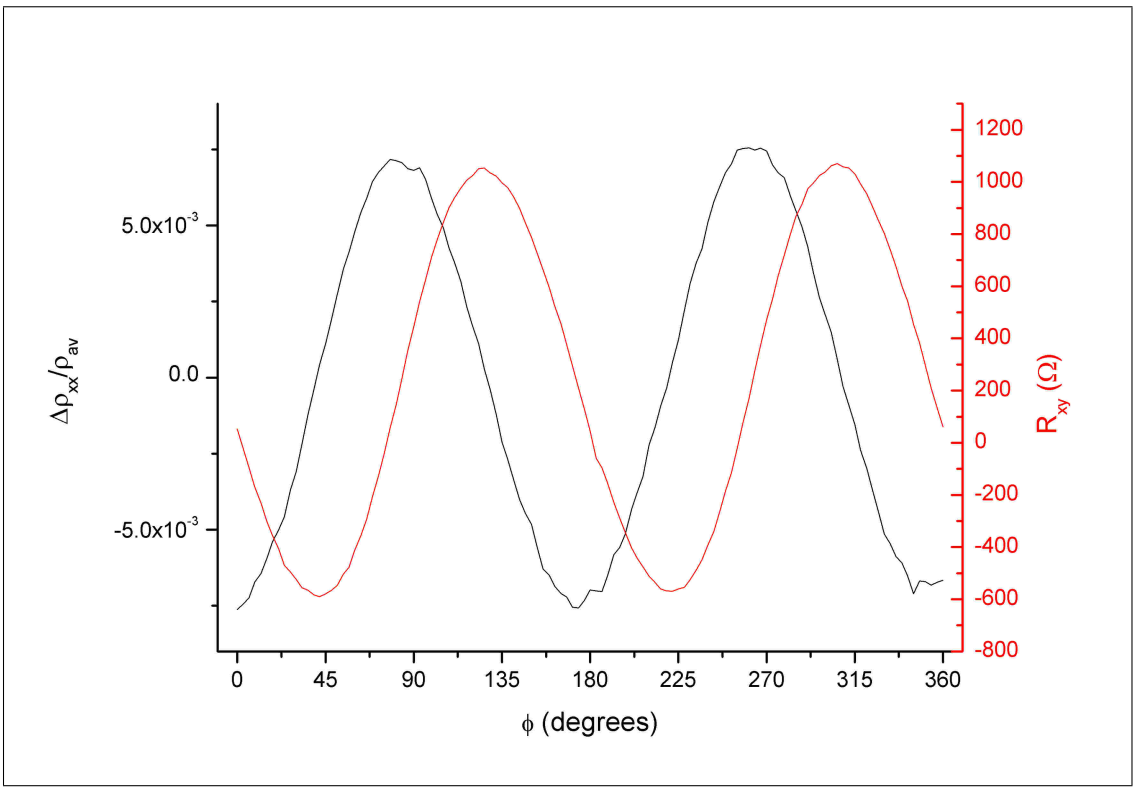

Fig. 2.14 — Longitudinal and transverse AMR for Mn293-[$\bar{1}$10], as-grown, at 30K, 4V bias and 1T field.

2.4.3 Corbino disc from wafer Mn291

Corbino discs were fabricated on wafer number Mn291, another wafer grown at Nottingham with a 5nm ($Ga_{0.95}$,$Mn_{0.05}$)As thin film and nominally identical to wafer Mn293 used for the Hall bars. Again, measurements were on the material as-grown, so the same novel fabrication steps as described above were required.

$R_{Corbino}$ is shown in figure 2.15 for an angular sweep at 30K. Data were also taken at 10K and 50K. This takes very much the same form as figure 2.11 as expected — figure 2.11 shows the crystalline terms as extracted from Hall bar data and figure 2.15 shows the raw Corbino data, which is itself just the crystalline contribution. Note also the similarity with the R_{xx} curve for the Hall bar in the [110] direction (figure 2.13), for which $\varphi = \psi$ so the C_I and $C_{I,C}$ terms introduce no phase shift.

The curve fit in figure 2.15 gives C_U ~0.0093 and C_C ~0.0007. All the coefficients — that is for the Corbino, the [100]-[010] pair and the [110]-[$\bar{1}$10] pair, over the

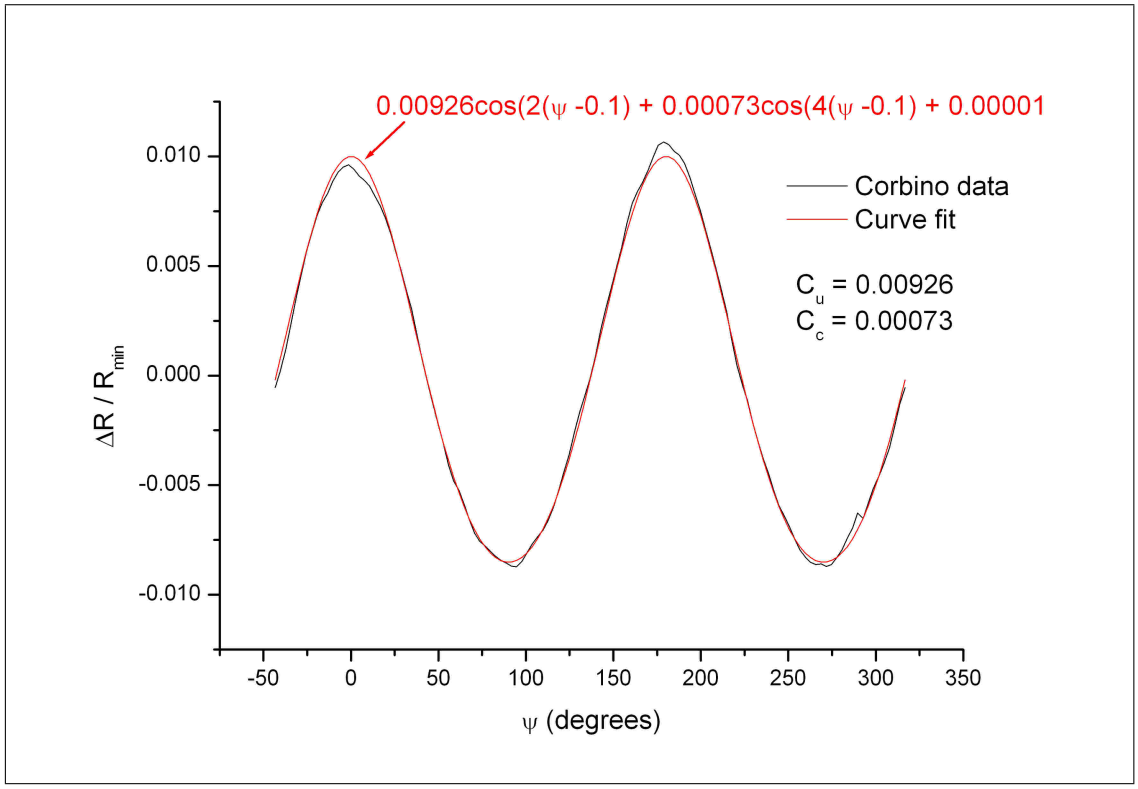

Fig. 2.15 — AMR for as-grown Corbino disc at 30K, 4V bias and 1T field. For the Corbino, a phase shift in the data simply corresponds to a misalignment of the Corbino with respect to the magnetic field.

whole range of temperatures — are plotted together in figure 2.16.

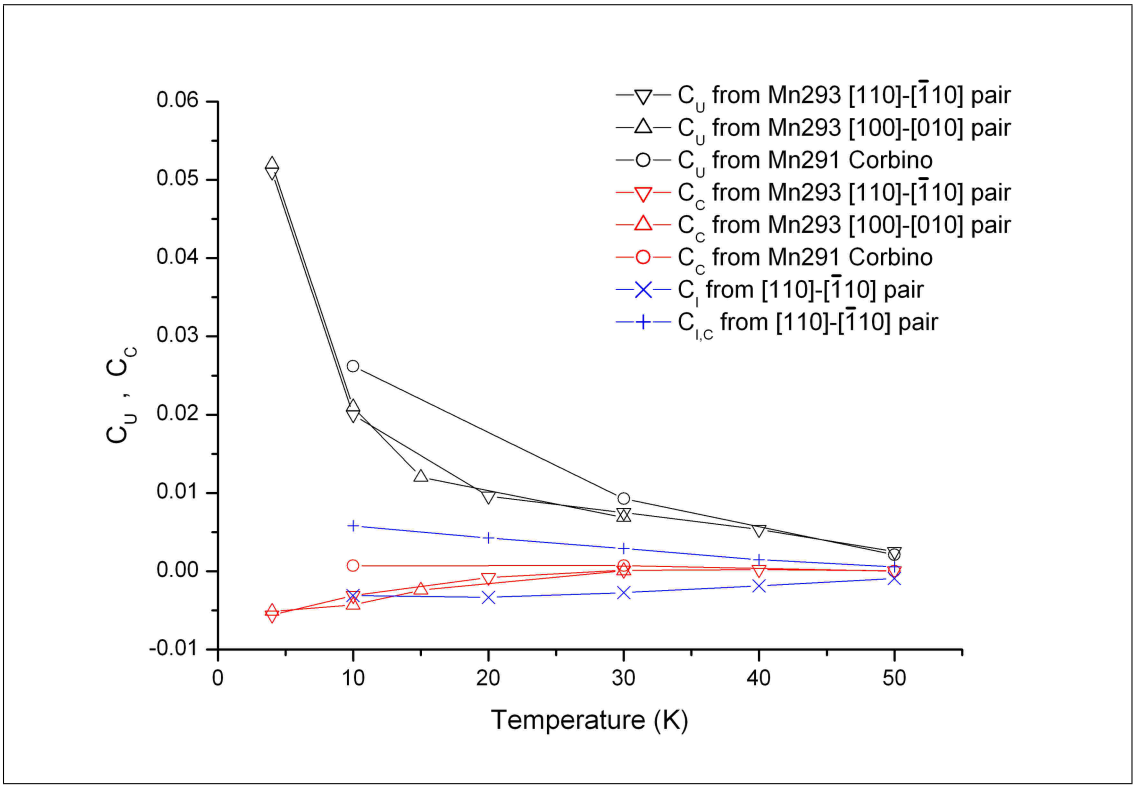

Fig. 2.16 — Crystalline and non-crystalline terms versus temperature for both pairs of Hall bars from Mn293 as-grown, at 4V bias and 1T field, and from a Corbino from wafer Mn291 as-grown.

Figure 2.16 shows that for ultra-thin, 5nm (Ga,Mn)As films the uniaxial term is the dominant term over all temperatures from 4K to 50K, with good agreement between the results from the two orthogonal Hall bar pairs and the Corbino disc.

2.4.4 The scaling of the longitudinal AMR with resistance

We can now return to the variation of longitudinal AMR with temperature, touched on briefly in section 2.4.2 above and illustrated in figure 2.9. Added to this plot is data from the other three Hall bars and from the Corbino — giving figure 2.17. Instead of plotting the longitudinal AMR against temperature it is now plotted against the log of the average resistance; although temperature is the main factor affecting resistance we can now also include data for various biases and field strengths.

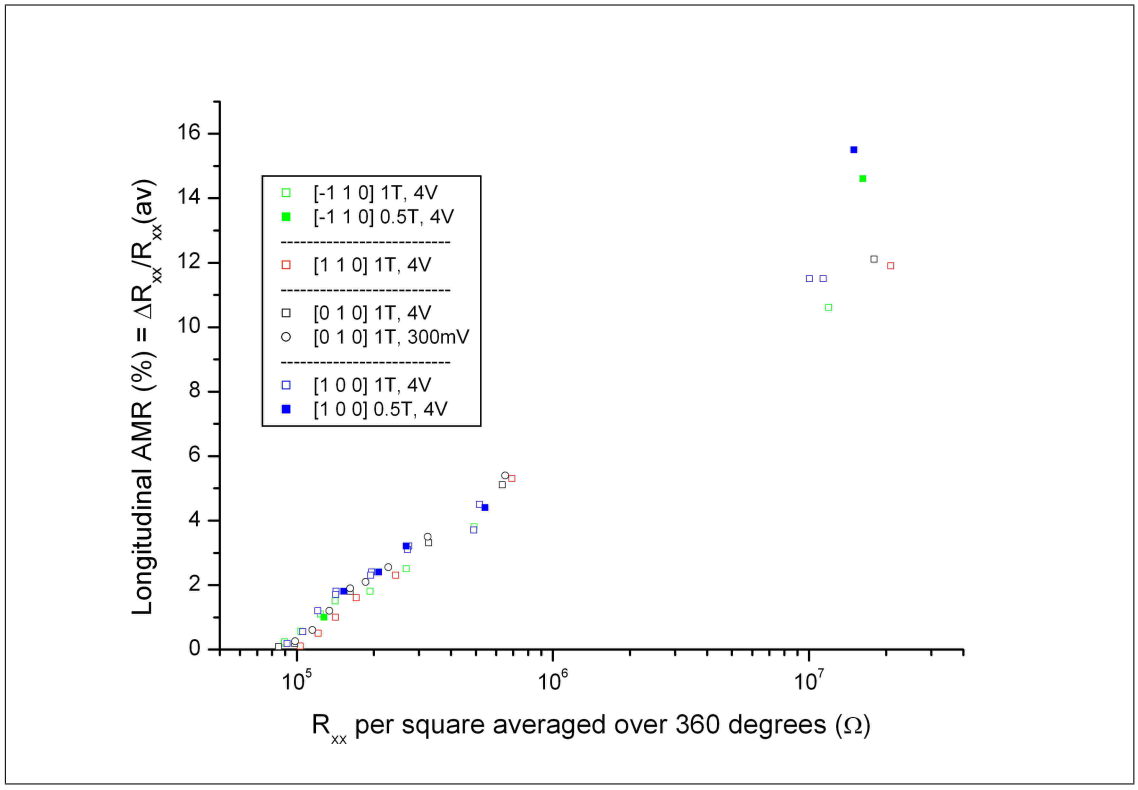

Fig. 2.17 — Longitudinal AMR as a function of temperature at various biases, for all four Hall bar samples and the Corbino disc, as-grown.

The large gap in data between $R \sim 10^6\Omega$ and $R \sim 10^7\Omega$ is from temperatures between 4K and 10K, at which we are not currently able to hold our samples at stable temperature. We are looking at other ways to reach these resistances.

2.5 Summary

The Anisotropic Magnetoresistance in gallium manganese arsenide comprises crystalline and non-crystalline parts. The non-crystalline part comes from the lowering of the symmetry by imposing a current direction. The crystalline part can be divided into a cubic [100]-[010] part and a uniaxial [110] part. In 25nm (Ga,Mn)As films the non-crystalline component dominates the AMR.

We fabricated Hall bars along the [100], [010], [110] and [$\bar{1}$10] crystallographic axes in 5nm ($Ga_{0.95}$, $Mn_{0.05}$)As thin films and through transport measurements we were able to extract the crystalline coefficients from orthogonal Hall bar pairs, showing that the uniaxial crystalline component dominates over the whole temperature range, from 4K to 50K. By similar measurements on Corbino geometries we were able to measure the crystalline terms directly thereby corroborating the Hall bar results. Data from the two orthogonal Hall bar pairs and from the Corbino disc were in very good agreement. We believe this is the first time a uniaxial crystalline component has been found to dominate the AMR signal in any material. Although the microscopic origin of this effect is unknown we also see a dominant uniaxial magnetocrystalline anisotropy, as shown in the following chapter.

References

[1] W. Thomson, "On the electro-dynamic qualities of metals: Effects of magnetization on the electric conductivity of nickel and iron," *Proceedings of the Royal Society*, vol. 8, pp. 546–550, 1857.

[2] T. R. McGuire and R. I. Potter, "Anisotropic Magnetoresistance in Ferromagnetic 3d Alloys," *IEEE Transactions on Magnetics*, vol. 11, no. 4, pp. 1018–1038, 1975.

[3] D. A. Thompson, L. T. Romankiw, and A. F. Mayadas, "Thin Film Magnetoresistors in Memory, Storage, and Related Applications," *IEEE Transactions on Magnetics*, vol. 11, no. 4, pp. 1039–1050, 1975.

[4] C. Gould, C. Rüster, T. Jungwirth, E. Girgis, G. M. Schott, R. Giraud, K. Brunner, G. Schmidt, and L. W. Molenkamp, "Tunneling Anisotropic Magnetoresistance: A spin-valve like tunnel magnetoresistance using a single magnetic layer," *Physical Review Letters*, vol. 93, no. 11, pp. 117203/1–4, 2004.

[5] J. Wunderlich, T. Jungwirth, B. Kaestner, A. C. Irvine, A. B. Shick, N. Stone, K.-Y. Wang, U. Rana, A. D. Giddings, C. T. Foxon, R. P. Campion, D. A. Williams, and B. L. Gallagher, "Coulomb Blockade Anisotropic Magnetoresistance Effect in a (Ga, Mn)As Single-Electron Transistor," *Physical Review Letters*, vol. 97, no. 7, pp. 077201–1, 2006.

[6] J. Sinova, T. Jungwirth, and J. Černe, "Magneto-Transport and Magneto-Optical Properties of Ferromagnetic (III,Mn)V Semiconductors: A Review," *International Journal of Modern Physics B*, vol. 18, no. 8, pp. 1083–1118, 2004.

[7] T. Dietl, F. Matsukura, H. Ohno, J. Cibert, and D. Ferrand, *Recent Trends in Theory of Physical Phenomena in High Magnetic Fields*. Kluwer, Dordrecht, 2003. p. 197. cond-mat/0306484.

[8] W. Döring, "Dependence of resistance of Ni crystals on direction of spontaneous magnetization," *Annalen der Physik*, vol. 32, pp. 259–276, 1938.

[9] A. W. Rushforth, K. Výborný, C. S. King, K. W. Edmonds, R. P. Campion, C. T. Foxon, J. Wunderlich, A. C. Irvine, P. Vašek, V. Novák, K. Olejník, J. Sinova, T. Jungwirth, and B. L. Gallagher, "Anisotropic Magnetoresistance Components in (Ga,Mn)As," *Physical Review Letters*, vol. 99, p. 147207, 2007.

Chapter 3

Magnetometry Studies of Patterned Gallium Manganese Arsenide Thin Films

3.1 Motivation

In chapter 2 I presented a systematic study of the Anisotropic Magnetoresistance (AMR) in thin films of the ferromagnetic semiconductor gallium manganese arsenide. This study had been motivated by the need to have a clearer understanding of the AMR in this material, in part due to recent reports of effects in (Ga,Mn)As that are of potential technological importance. Phenomena such as Tunnelling Anisotropic Magnetoresistance (TAMR) and Coulomb Blockade Anisotropic Magnetoresistance (CBAMR) could provide the basis for novel spintronic devices [1], [2], [3], [4], [5], development of which would rely on a detailed understanding of the AMR.

Furthermore, the ability to manipulate the magnetic anisotropy, in particular to have local control over the orientation of the easy axis or axes with respect to the crystal structure, would be of great benefit for the realization of spintronic devices to their full potential, and it is this that forms the motivation for this chapter. Such

local control has lately been demonstrated, most recently in (Ga,Mn)As nanobars [6] where it was shown that patterning elongated nanostructures along the direction of one of the magnetic easy axes in a cubic system can harden the perpendicular axis, which was an equivalent easy axis in the un-patterned material, over the whole range of temperatures from 5K up to the Curie temperature.

In this chapter I develop a method first used by Wang *et. al.* [7] for extracting anisotropy coefficients quantitatively. By applying this analysis to my own patterned and un-patterned (Ga,Mn)As thin films I am able to quantify the local-control effects. Moreover, with patterned samples having arrays of stripes along the easy and hard axes I demonstrate that stripes along the hard axis can be used to flip the hard- and easy-axis directions. We see no reason that this method could not be used to bring the easy axis into *any* in-plane orientation.

3.2 Background and Theory

From extensive previous measurements on un-patterned (Ga,Mn)As thin films it is well-established that this material exhibits a complex and varied magnetic anisotropy. In chapter 1 I described how a gallium manganese arsenide film grown epitaxially on a gallium arsenide substrate has in-plane symmetric, compressive strain due to the larger lattice constant of the film compared with the substrate. Early studies of compressively-strained films revealed a competition between in-plane cubic easy axes along the [100] and [010] crystallographic directions and a uniaxial in-plane easy axis along $[\bar{1}10]$ (figure 1.3 in the introduction provides the definitions of *uniaxial*, *cubic* and *biaxial* used in this report). Although the uniaxial anisotropy is well documented its microscopic origin remains unclear; it is unexpected since the [110] and $[\bar{1}10]$ directions are equivalent in the lattice unit cell (see figure 1.1 in chapter 1). However, if an artificial anisotropic shear strain along this direction is added into calculations the magnetic anisotropy is reproduced [8] (see section 1.3.3 for more details). The

cubic contribution is a result of the GaAs lattice symmetry.

The magnetic anisotropy is very sensitive to the hole concentration, temperature, strain and proportion of substitutional to interstitial manganese (see chapter 1); consequently the anisotropy can vary greatly from one sample to the next. In many 25nm samples the $[\bar{1}10]$ uniaxial easy axis was seen to dominate over the whole temperature range up to the Curie temperature, whereas in other samples this axis dominated only between T_C and ∼20K, below which the cubic easy axes were dominant. For samples as large as 5mm×5mm, Wang *et. al.* were able to show [7] that such behaviour in these thin films can be consistent with a single-domain model comprising a cubic term with energy minima along the [100] and [010] directions and a uniaxial term with a minimum along $[\bar{1}10]$, as given in equation 3.1:

$$E = K_U \sin^2\theta + \left(\frac{K_C}{4}\right)\sin^2(2\theta) - M_S H\cos(\gamma - \theta) \tag{3.1}$$

Here K_C and K_U are the lowest order cubic and uniaxial anisotropy coefficients, H is the external magnetic field, M_S is the magnetization and θ and γ are the angles of M and H to the $[\bar{1}10]$ direction respectively (figure 3.1).

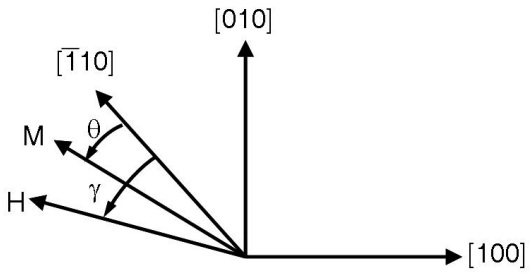

Fig. 3.1 — In-plane angle designations in single-domain model.

It is now known that a strongly-competing uniaxial [110] component is also present in many samples, as seen later in this chapter. More generally, therefore, we could in principle write an energy equation which includes a uniaxial term $K'_U \sin^2(\theta - 90°)$ along [110]. In practice, however, this isn't necessary if we allow the uniaxial term K_U to be either positive, corresponding to an easy axis along $[\bar{1}10]$, or negative,

corresponding to a [110] uniaxial easy axis. A uniaxial contribution along [010] has also been reported in compressively-strained (Ga,Ma)As thin films but this is much weaker [2].

A corollary of the dependence of the magnetic anisotropy on hole concentration, temperature, manganese incorporation and strain is that the only method we have for *local* manipulation of the anisotropy, important for device applications, is local control of the in-plane compressive growth strain. This has been achieved by etching structures into the film which allows the strain to relax in the directions perpendicular to the etched sidewalls. Transport and magnetometry measurements on patterned (Ga,Mn)As samples have shown that structures such as wires [9],[10],[11],[12], Hall bars [13],[14] and nanobars [6] can modify the intrinsic anisotropy by lowering the energy density along the length of the structure. For narrow-enough structures these induced anisotropies can dominate over the intrinsic material anisotropy at all temperatures below T_C.

Hamaya *et. al.* compared magnetotransport results from 2-µm-wide and 1-µm-wide (Ga,Mn)As wires [9] and 100-µm-wide, 1.5-µm-wide and 0.8-µm-wide wires [10] fabricated along various orientations; they observed in the narrower wires a new anisotropy contribution along the length of the wire, of a similar magnitude to the intrinsic anistropies. It was reported [9],[10],[11] that the additional contribution was due to shape anisotropy in the narrower structures, but it is now established that the shape anisotropy is in fact around an order of magnitude weaker than the intrinsic anisotropies in thin (Ga,Mn)As films, due to the low moment density in this material (the shape anisotropy is proportional to the net sample magnetization squared). Hamaya *et. al.* had used an infinite rod model to calculate the shape anisotropy whereas these thin film samples, whose thickness is much smaller than their width, are more precisely described by a rectangular prism model [15] which, for the same cross-sectional area, predicts a shape anisotropy much smaller than that predicted by the infinite rods model [6]. Using the rectangular prism model gives the shape aniso-

tropy in Hamaya's samples as around 70 Jm^{-3} at 10 K, compared with uniaxial and cubic magnetocrystalline anisotropy coefficients of around 200 Jm^{-3} and 500 Jm^{-3} respectively.

Later, SQUID magnetometry and magnetotransport data were reported for nanobars 20nm thick by 200nm wide by 1µm long [6]. These were patterned along the [100] and [010] directions which were equivalent easy axes in the parent wafer, but for the patterned samples it was shown that the direction perpendicular to the bar ([010] in the case of the [100] bar, and *vice versa*) had gone from being equivalent to being a pronounced hard axis. This effect dominated the intrinsic anisotropy at all temperatures below T_C. At a similar time, during our AMR studies although not presented in chapter 2, we also observed that the AMR in very narrow Hall bars was modified compared with that in wider Hall bars [13] and very similar effects have since been described in detail in a comparison of Hall bars of different widths [14]. The effect seen in all these cases — an additional anisotropy contribution along the length of narrow, elongated structures — is now known to be due in fact to relaxation along the width of the bar of the in-plane, compressive growth strain. Most recently, the significance of strain relaxation as being the cause of these effects was confirmed by a combination of SQUID magnetometry, x-ray diffraction measurements, finite elements simulation and $\boldsymbol{k \cdot p}$ calculation for samples comprising arrays of stripes along the [100] direction [12]. With stripes 70nm thick by 200nm wide by 100µm long, separated by 200nm, it was again shown by SQUID magnetometry that the [010] direction (perpendicular to the long axis of the stripe) had gone from being an equivalent easy axis to being a pronounced hard axis compared with the un-patterned wafer; furthermore, x-ray diffraction experiments on the samples showed that, whilst the samples were strained in the [100] direction there was a "large degree of strain relaxation" along [010]. This strain relaxation was confirmed to be the cause of the modified magnetic anisotropy in $\boldsymbol{k \cdot p}$ calculations; with this strain included in the calculations the modified magnetic anisotropy was qualitatively reproduced.

Several independent studies, involving a variety of structures orientated along various crystallographic directions, have now provided mutual confirmation that tiny changes in lattice constant can completely change the magnetocrystalline energy landscape of the material [14], [6], [16], [12], [17], with strain relaxations in these studies being typically as small as 10^{-4}.

In this chapter I extract the anisotropy coefficients K_U and K_C quantitatively for patterned and un-patterned (Ga,Mn)As samples to quantify the change in magnetic anisotropy due to strain relaxation. I pattern arrays of stripes along the $[\bar{1}10]$ and [110] directions, respectively the easy and hard axes over most of the temperature range below T_C in the un-patterned material. The chosen dimensions of the stripes were expected to achieve strain relaxation of the order of 10^{-4} and the resulting analysis shows striking results, with a deepening of the easy axis energy minimum for the stripes patterned along $[\bar{1}10]$ (and a corresponding hardening of the hardest of the main crystallographic axes), and a rotation of the easy axis by a full 90° for samples patterned along [110], bringing the easy axis into the stripe direction for this sample.

In the literature it has frequently been reported that the uniaxial anisotropy should vary with magnetization as $K_U \propto M^2$ and the cubic anisotropy as $K_C \propto M^4$. The basis for these statements is a 1966 paper which provides a theoretical treatment of the temperature dependence of magnetic anisotropies in ferromagnetic insulators [18] and these relationships have even been reported experimentally in (Ga,Mn)As thin films [7]. However, it has since been shown that these simple dependencies do not hold true in metallic systems [19]. The results from my quantitative analysis show clearly that the dependencies of K_U and K_C on M are not so straightforward; this is contrary to the results presented in reference [7] for similar material, but the samples in that study were thicker (50nm), of a lower doping and not annealed, and the cubic term was much stronger in that material.

3.3 Sample Fabrication

Samples were fabricated in sets of three — one sample with gratings orientated along the [110] crystallographic axis, one with gratings along the [$\bar{1}$10] axis and a control sample with no patterning. The samples are 5mm×5mm squares from adjacent positions on the same parent wafer.

To make certain that the three samples are truly similar they were all fabricated together on a single 10mm×10mm chip, ensuring that all fabrication steps, most importantly baking, developing and etching, were exactly the same for each sample. Unlike for the Hall bar and Corbino samples described in chapter 2, the fabrication involved baking the samples at 180° for between 1 and 3 hours (for the purposes of dehydrating the samples after cleaning and for curing the polymer resist mask). Measurements, therefore, are not on as-grown samples, but partially annealed. After all fabrication steps had been completed the 10mm×10mm chip was cleaved into the smaller samples.

The gratings were defined by electron beam lithography using an accelerating voltage of 30kV and a beam current of 600pA. The resist was A2 950 PMMA[1]; this is a positive resist at this beam current, i.e. it is the exposed areas that are developed. The resist thickness was approximately 60nm.

Each of the 5mm×5mm gratings was made by writing an array of smaller fields as illustrated in figure 3.2, each field being 100µm by 100µm and overlapping by 6µm. The 100µm fields comprise exposed lines 100µm long with a period of 1.2µm; the exposure was intended to create a trench 400nm wide in the resist after development, leaving 800nm of masked substrate. A border trench 4µm wide was defined around each field to allow for imperfect stitching together; without these trenches the gratings could end up with kinks which could act as domain wall nucleation or trapping centres — see figure 3.3. The writing time was almost 45 hours; despite this being significantly longer than is usually desirable the exposure proved to be remarkably

[1] Poly(methyl methacrylate)

consistent across the whole chip (as determined from AFM measurements), due to the high stability of our beam current.

After the electron beam resist had been developed the grating pattern was transferred down to the thin film by wet etching, using a hydrogen peroxide–phosphoric acid etchant [20]. Given the lithographic dimensions described above this should result in 800nm-wide (Ga,Mn)As stripes separated by 400nm; these dimensions were chosen based on the previous studies described in section 3.2. Finally the resist mask was cleaned off with a conventional solvent wash.

Etch Profile

A very important caveat of wet chemical etching is that the etch profile is often anisotropic, with certain crystallographic planes of the substrate etching more rapidly than others. For gallium arsenide etched in the hydrogen peroxide–phosphoric acid etchant that I have used the result is that stripes along the [110] direction have an undercut cross-section whilst stripes along $[\bar{1}10]$ are bevelled in the opposite direction, as shown in figures 3.4 (taken from reference [20]). In this reference the substrate is GaAs, the stripes are almost forty times as large as mine, the etch solution is the same as mine but in a concentration 100 times stronger and the etch time was ten times as long. Despite these differences I expected my (Ga,Mn)As samples to undergo the same anisotropic etching behaviour and I have verified this to be the case by taking cross-sectional SEM images of my stripes, presented later in this chapter. This has important consequences for the strain relaxation. Finite elements simulations performed by a colleague of mine in Prague show that the strain relaxation is markedly different for undercut and overcut etch profiles, with more relaxation for the undercut profile. The results of these simulations are shown in figure 3.5.

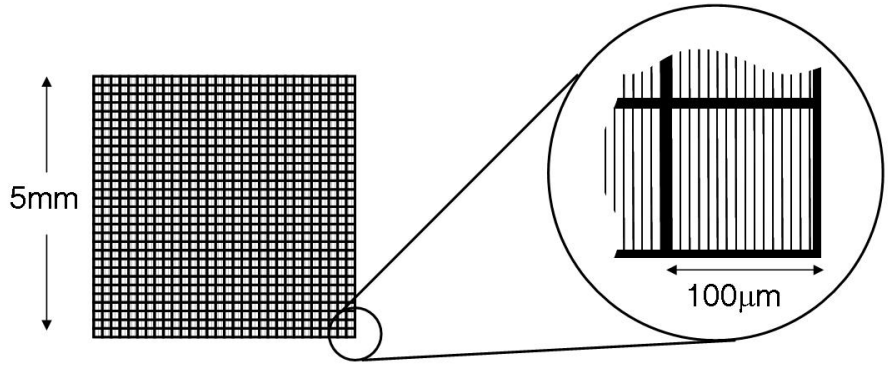

Fig. 3.2 — Gratings design (not to scale). Lines and rectangles show where the resist is exposed.

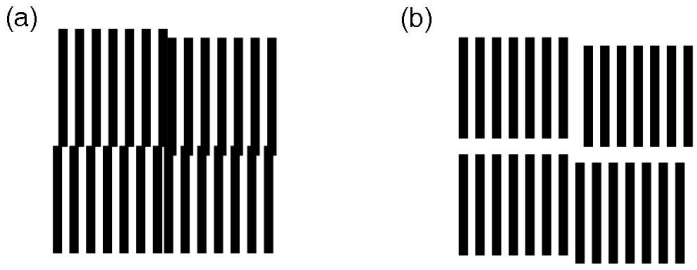

Fig. 3.3 — Resulting gratings patterns, (a) with and (b) without the use of border trenches between fields. Here shaded regions represent (Ga,Mn)As. Without border trenches imperfect alignment of fields could lead to overlapping of (Ga,Mn)As stripes resulting in discontinuous boundaries.

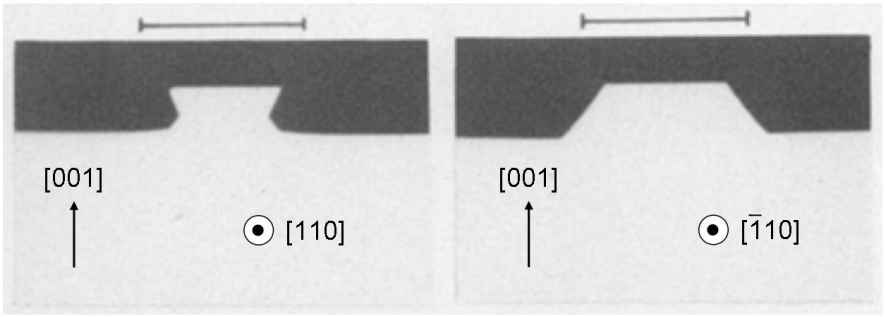

(a)

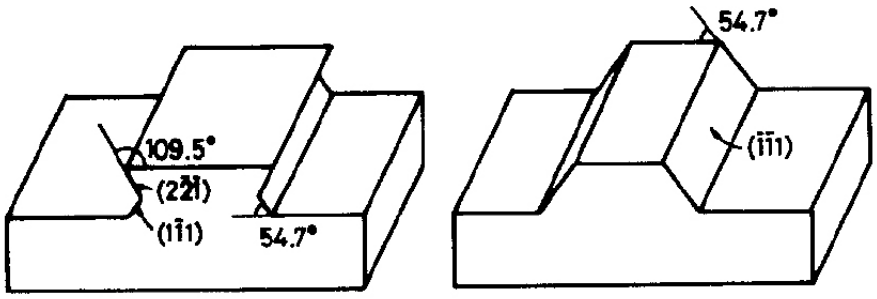

(b)

Fig. 3.4 — Etching profiles of (001)GaAs etched in $1H_3PO_4$: lH_2O_2 : $1H_20$ for two minutes. The bars drawn in the top of the figure correspond to the masking pattern length of 28 µm. Images adapted from reference [20].

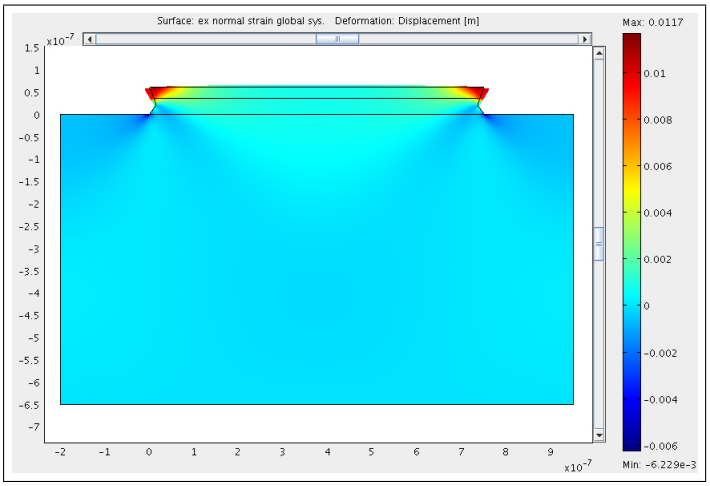

(a) Undercut etch profile

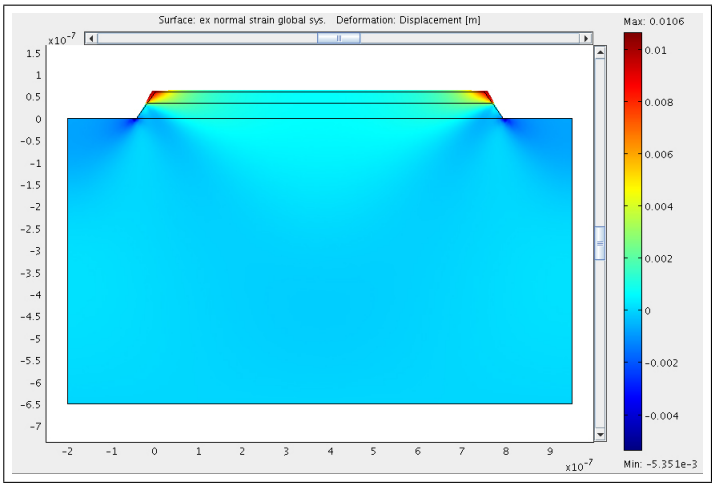

(b) Overcut etch profile

Fig. 3.5 — Strain relaxation calculations for undercut and overcut etch profiles based on finite elements simulation and performed by a colleague in Prague. The colourbar on the right hand side indicates the strain, with the darkest red denoting the most strain relaxation.

3.4 Measurement and Analysis Description

We investigate the magnetic anisotropy of the samples by performing two kinds of SQUID magnetometry measurement. The first is measurement of the remanent magnetization of the sample from which we can determine, as a function of temperature, the orientation and symmetry (uniaxial, biaxial or cubic) of the easy magnetic axis or axes, as well as obtaining an accurate measure of the Curie temperature. For temperature ranges where the cubic term is dominant it is possible to extract from the remanence data the ratio of the uniaxial to cubic anisotropy coefficients, K_U/K_C.

The second type of measurement is M–H hysteresis measurements along the hard axis at various temperatures, from which it is possible to quantify the coefficients individually.

3.4.1 Remanent Magnetization Measurements

Remanence measurements were made along each of the four in-plane crystallographic orientations — that is [100], [010], [110] and [$\bar{1}$10] — for each sample. The sample is mounted in the chosen direction then cooled from 150K (well above the Curie temperature for these wafers) to 2K in an external field of 1000 Oe applied along the measurement axis. At 2K the external field is removed, at which point the magnetization rotates into the nearest energy minimum (or minima in the case of a multi-domain state), and we record the remanent magnetization — that is the projection of the magnetization of the sample in zero applied field onto the measurement axis — as the sample is warmed back up to 150K. The sample is removed and remounted and the process repeated for the remaining three in-plane orientations.

The first step in the analysis is to work out the net magnetization of each sample as a function of temperature. For single-domain samples with competing biaxial ([100]-[010]) and uniaxial ([$\bar{1}$10] and/or [110]) symmetries we find the net magnetization, denoted M_S, from the sum of the squares of the remanent magnetizations along [110]

and $[\bar{1}10]$ (denoted $M_{[110]}$ and $M_{[\bar{1}10]}$ respectively), as shown in equation 3.2. This is correct for a single-domain sample in both the biaxial and uniaxial regimes if the biaxial easy axes are symmetrical about $[\bar{1}10]$. The sum of the squares of $M_{[100]}$ and $M_{[010]}$ — equation 3.3 — should also provide the net magnetization for temperatures where the sample is uniaxial, but in the biaxial regime this calculation will give a value which is too large.

$$M_{S,1} = \sqrt{{M_{[110]}}^2 + {M_{[\bar{1}10]}}^2} \tag{3.2}$$

$$M_{S,2} = \sqrt{{M_{[100]}}^2 + {M_{[010]}}^2} \tag{3.3}$$

If the biaxial easy axes are not symmetrical about $[\bar{1}10]$ four further relationships can be used to find the net magnetization (3.4). One pair of these — either $M_{S,A}$ and $M_{S,B}$ or $M_{S,C}$ and $M_{S,D}$ — should each provide the correct magnetization for both the uniaxial *and* biaxial regimes for a single-domain sample, even in the case that biaxial axes are not symmetric about $[\bar{1}10]$. If the biaxial axes are symmetrical all four should be correct; if the bisector of the biaxial axes is closer to [100] the first pair applies; and when the bisector is closer to [010] the second pair applies.

$$\begin{aligned}
M_{S,A} &= \sqrt{\left(M_{[100]} - \sqrt{2}M_{[110]}\right)^2 + {M_{[100]}}^2} \\
M_{S,B} &= \sqrt{\left(M_{[010]} - \sqrt{2}M_{[\bar{1}10]}\right)^2 + {M_{[010]}}^2} \\
M_{S,C} &= \sqrt{\left(M_{[100]} - \sqrt{2}M_{[\bar{1}10]}\right)^2 + {M_{[100]}}^2} \\
M_{S,D} &= \sqrt{\left(M_{[010]} - \sqrt{2}M_{[110]}\right)^2 + {M_{[010]}}^2}
\end{aligned} \tag{3.4}$$

Having calculated the magnitude of the net magnetization it is straightforward to extract the orientation or orientations of the magnetization with respect to the $[\bar{1}10]$ axes as follows which assumes the sample is in a single-domain state (θ is defined with

respect to the $[\bar{1}10]$ axis as previously — see figure 3.1):

$$\begin{aligned}
M_{[\bar{1}10]} &= M_S|\cos\theta| & \theta &= \pm\arccos(M_{[\bar{1}10]}/M_S) \\
M_{[110]} &= M_S|\cos(\theta+90^\circ)| & \theta &= \pm\left[90^\circ - \arccos(M_{[110]}/M_S)\right] \\
M_{[100]} &= M_S|\cos(45^\circ-\theta)| & \theta &= 45^\circ \pm \arccos(M_{[100]}/M_S) \\
M_{[010]} &= M_S|\cos(\theta+45^\circ)| & \theta &= -45^\circ \pm \arccos(M_{[010]}/M_S)
\end{aligned} \tag{3.5}$$

We are now able to extract the ratio of the anisotropy constants, K_U/K_C, from the remanence data in temperature ranges where the sample is biaxial. In remnance, i.e. with no external field, the third term in equation 3.1 is zero and the stable orientation of the magnetization is given by $(\partial E/\partial\theta = 0)$:

$$\begin{aligned}
E &= K_U\sin^2\theta + \frac{K_C}{4}\sin^2(2\theta) \\
\frac{\partial E}{\partial\theta} &= 0 = 2K_U\sin\theta\cos\theta + \frac{K_C}{4}\cdot 2\sin 2\theta\cos 2\theta\cdot 2 \\
0 &= K_U\sin 2\theta + K_C\sin 2\theta\cos 2\theta \\
\frac{K_U}{|K_C|} &= \cos 2\theta
\end{aligned} \tag{3.6}$$

3.4.2 Hysteresis Measurements

Hysteresis measurements were performed along the hard-axis direction at various temperatures for each sample. From hard-axis hysteresis measurements it is possible to extract the anisotropy coefficients quantitatively by fitting the single-domain model, equation 3.1, to the data. Repeating this at each temperature allows us to observe the evolution of the anisotropy coefficients with temperature and, by continuation, with saturation magnetization. This fitting cannot be performed for measurements along other orientations since there is no simple analytical solution, and the M–H loops would be hysteretic for non-hard axes making the fitting process inaccurate. Since hard-axis loops should be closed and not hysteretic (with coherent rotation of

the magnetization vector), accurate fitting becomes possible. One caveat is that the curvature of hard-axis M–H loops is small at low temperatures meaning that the fitting becomes less reliable the lower the temperature and the resulting anisotropy coefficients will have larger error bars as you approach 2K.

The samples were mounted along either [110] or [$\bar{1}$10] (the hard axis having been determined from remanence measurements), cooled to 2K and an external field was swept along the measurement axis from -3000 Oe to +3000 Oe and back (±3000 Oe is more than enough to saturate the magnetization in these samples, which can be seen in the M–H curves that result). The magnetization of the sample was recorded as a function of external field strength and the measurement was repeated at various temperatures up to T_C. A description of the fitting follows. We will first consider the case of the hard axis being along the [110] direction.

In general the projection of the net magnetization onto the [110] axis can be expressed as $M_{[110]} = M_S \sin\theta$ where θ is, as usual, the angle of the magnetization with respect to the [$\bar{1}$10] direction. Specifically, when the external field is above some field H_C, the magnetization will lie along the field direction — the hard axis in this case — so θ is 90°. Therefore we can write

$$\begin{aligned} M_{[110]} &= M_S && \text{for} && H > H_C \\ M_{[110]} &= M_S \sin\theta && \text{for} && H < H_C \end{aligned} \tag{3.7}$$

In order to be able to fit the single-domain model to the data we need to know H_C in terms of the anisotropy constants. With the external field applied along the [110] direction γ is 90° and the third term in equation 3.1 reduces to $MH\sin\theta$:

$$E = K_U \sin^2\theta + \left(\frac{K_C}{4}\right)\sin^2(2\theta) - M_S H \sin\theta \tag{3.8}$$

The conditions for stable magnetization, which are $(\partial E/\partial\theta = 0)$ and $(\partial^2 E/\partial\theta^2 > 0)$,

can then be expressed as

$$\frac{\partial E}{\partial \theta} = K_U \sin 2\theta + K_C \sin 2\theta \cos 2\theta - M_S H \cos\theta = 0 \tag{3.9}$$

$$\frac{\partial^2 E}{\partial \theta^2} = 2K_U \cos 2\theta + 2K_C \cos 4\theta + M_S H \sin\theta > 0 \tag{3.10}$$

The simplest solution is $\theta = 90°$, i.e. the magnetization is along the field direction, which happens when $H > H_C$, in which case $M_{[110]} = M_S \sin\theta = M_S$ and equation 3.10 becomes

$$H > 2(K_U - K_C)/M_S$$

H_C, is therefore $2(K_U - K_C)/M_S$ and we can rewrite equations 3.7 as

$$\begin{aligned} M_{[110]} &= M_S && \text{for} && H > 2(K_U - K_C)/M_S \\ M_{[110]} &= M_S \sin\theta && \text{for} && H < 2(K_U - K_C)/M_S \end{aligned} \tag{3.11}$$

Substituting $M_{[110]} = M_S \sin\theta$ into equation 3.9 then gives us the fitting relationship which is valid over the range $H < 2(K_U - K_C)/M_S$; see Appendix B for the derivation.

$$H_{110} = 2\left(\frac{K_U + K_C}{{M_S}^2}\right) M_{110} - 4\left(\frac{K_C}{{M_S}^4}\right) {M_{110}}^3 \tag{3.12}$$

Fitting this equation to the hysteresis loops requires just two fitting parameters, $(K_U + K_C)$ as the first and K_C alone as the second, from which we can trivially extract K_U and K_C individually.

In the case of the hard axis being along $[\bar{1}10]$ we can follow a similar procedure which gives the fitting formula as follows (see Appendix B for the full derivation):

$$H_{\bar{1}10} = -2\left(\frac{K_U - K_C}{{M_S}^2}\right) M_{\bar{1}10} - 4\left(\frac{K_C}{{M_S}^4}\right) {M_{\bar{1}10}}^3 \tag{3.13}$$

In this case the field H_C is $-2(K_U + K_C)/M_S$ so this fitting is valid over the range $H < -2(K_U + K_C)/M_S$.

Two points are worth considering. First, the raw magnetization signal comprises the signal from the sample magnetization, M, plus a diamagnetic background signal from the sample, the holder etc., which is proportional to H. In order to have $M(H)$ it was necessary, therefore, to subtract the diamagnetic background from each set of hysteresis data. Second, the 4^{th}-power dependence of the second term on M_S can introduce large errors into the second parameter if M_S is not chosen carefully, and since this also feeds back into the value for K_U it can cause large errors in both anisotropy constants; therefore we have to choose M_S accurately. How this was done is described for each sample in the corresponding *Results* section.

In the course of developing this procedure but before applying it to my own samples I performed this fitting on hard-axis hysteresis data for 25nm $(Ga_{0.94},Mn_{0.06})As$ films that were used in a related study by Rushforth *et. al.* [17]. By bonding Hall bar samples to piezoelectric stressors it was possible to have voltage-control of the strain of the (Ga,Mn)As sample and therefore to study the effects on the magnetic anisotropy of varying the sample strain *in situ*. Details of that study are not the subject of this report, but anisotropy coefficients extracted by the fitting procedure described above were used in 6-band $\boldsymbol{k \cdot p}$ plus kinetic exchange model calculations to compare the experimental results with theory and the agreement was remarkable, which is a good indication that using this method to extract anisotropy coefficients is reliable. In addition this work provided confirmation that induced strains of the order of 10^{-4} are enough to introduce strong adjustments to the magnetic anisotropy of the film.

Units of Anisotropy Coefficients

In our SQUID magnetometer the external field is measured in Oersteds and the sample magnetization in emu. From equation 3.9 we see that K_U and K_C take the same units as $M_S H$ so, as fitted this way, that is $(\text{emu} \cdot \text{Oe})$. It is more convenient to quote the

anisotropy energies in units of Joules. Since 1 emu $\equiv 10^{-3}$ Am^2 and 1 Oe $\equiv$ 1 Gauss $\equiv 10^{-4}$ T $\equiv 10^{-4}$ NA^{-1}m^{-1}, the anisotropy constants from this fitting process are in units of 10^{-7} Nm, i.e. 10^{-7} Joules.

For comparing samples of different volumes — for example for making comparisons between the control sample and the patterned samples which have a significant proportion of the (Ga,Mn)As film etched away — it is more useful to compare the anisotropy energy per unit volume, so we simply divide the anisotropy energy by the volume of (Ga,Mn)As in the sample. This method is entirely equivalent to converting the magnetization from emu to emu/m^3 before doing the fitting.

So, to convert the anisotropy coefficients from (emu $\cdot$ Oe) to J m^{-3} :

$$1 \text{ emu} \cdot \text{Oe} \equiv \left(\frac{10^{-7}}{\text{Volume of (Ga,Mn)As}} \right) \text{ J m}^{-3} \tag{3.14}$$

3.4.3 Remanent Magnetization Simulations

After extracting the anisotropy coefficients from hard-axis hysteresis loops for each sample these values of K_U and K_C can be substituted into the single-domain model and the expected remanent magnetization calculated. Since the calculation contains no free parameters and only takes as inputs the variation of K_U, K_C and the saturation magnetization with temperature, all determined from experiment, comparing the results of such simulations with the original remanence data provides an indication of how reliable the extracted anisotropy coefficients are.

I conduct such simulations by starting the magnetization along a particular angle θ corresponding to [$\bar{1}$10], [110], [100] then [010] ($\theta = 0°, 90°, 45°$ and $-45°$ respectively), calculating the energy gradient $\partial E/\partial\theta$ and allowing the magnetization to rotate along the energy gradient until it reaches an energy minimum. From this I have the stable orientation of the magnetization with respect to the [$\bar{1}$10] axis and it is straightforward to calculate the projection of that magnetization onto the corresponding measurement axis (from equation 3.5). Good agreement between the measured and simulated rema-

nences will provide some confirmation that that the extracted anisotropy coefficients are likely to be correct.

3.5 Results & Analysis — 1µm Gratings

An initial set of samples was made with (Ga,Mn)As stripes 1µm wide separated by 200nm. Quantitative analysis was hindered by complex behaviour of the magnetization of the parent wafer, but qualitatively it was observed that patterning along either [110] or [$\bar{1}$10] made the stripe direction the easy axis at all temperatures, an effect we were not expecting to be so pronounced in such wide structures.

3.5.1 Sample Details

This, the first set of samples, was made from wafer number Mn289 which comprises a 25nm ($Ga_{0.95}$,$Mn_{0.05}$)As thin film grown on GaAs(001). The three samples are referred to as *CSK139[110]*, *CSK139[$\bar{1}$10]* and *CSK139[control]* respectively. An AFM image of part of the grating along the [$\bar{1}$10] direction is shown in figure 3.6, with a line analysis across part of that image shown in figure 3.7. The etches are narrower than hoped for, being 200nm instead of 400nm. Having a 1.2µm period, the (Ga,Mn)As stripes are, therefore, 1µm wide instead of 800nm. This has been caused by slight underdevelopment of the electron beam resist[2]. The samples were baked for ∼3 hours at 180°C during fabrication. Although the stripes were wider than hoped for and it was expected that the effects of patterning would be too weak to be observed, these samples were nevertheless measured in the SQUID system and turned out to show strong patterning effects.

For the two chips with gratings approximately 35% of the (Ga,Mn)As film is etched away compared with the control sample. The etch depth is of the order of 60nm which confirms that the etch has gone right through the (Ga,Mn)As film and into the substrate.

[2] In practice it is difficult to achieve perfect development for these samples as the pattern rapidly goes from underdeveloped to overdeveloped.

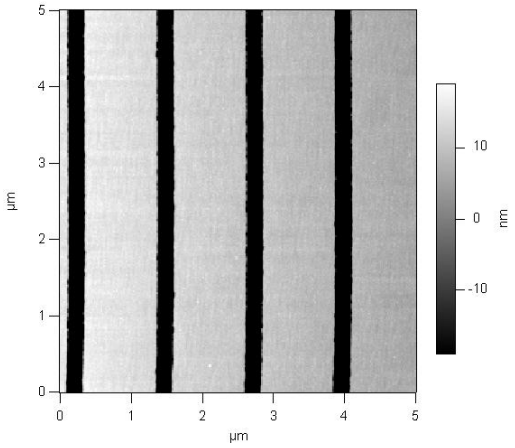

Fig. 3.6 — AFM image of the 1µm (Ga,Mn)As gratings along the [$\bar{1}$10] direction. The lighter regions are the (Ga,Mn)As stripes; the dark lines are the etched trenches.

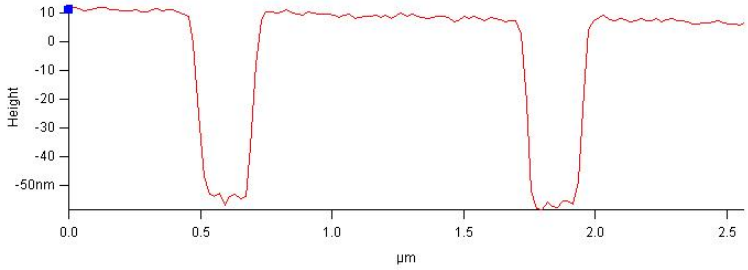

Fig. 3.7 — Height profile from a line across the middle of figure 3.6. The (Ga,Mn)As stripes are 1µm wide, separated by 200nm. The etch depth is ∼60nm, more than enough to etch right down through the (Ga,Mn)As film and into the substrate.

3.5.2 Remanent Magnetization Measurements

The remanent magnetization curves along each of the four in-plane directions for the control sample are shown in figure 3.8. In general these show typical anisotropy for a 25nm film, as described in the introduction to this chapter. A cubic, [100]-[010] symmetry dominates the energy density from 2K up to around 20K, above which there is a transition to a uniaxial, [$\bar{1}$10] symmetry; the [110] direction is a clear hard axis at all temperatures; and the Curie temperature is around 89K which is typical for films of this manganese content, thickness and annealing time. However, the [100] and [010] curves show significant splitting over most of the range of temperatures whereas, in the single-domain models presented earlier in the chapter, they are equivalent. We were unable to explain the remanence behaviour in terms of the single-domain model presented earlier; however, the splitting of the [100] and [010] traces was replicated qualitatively in remanence simulations involving an additional energy term offset by some arbitrary angle Δ from the [$\bar{1}$10] axis (using arbitrary values for K_U and K_C in the simulation). A physical interpretation of this additional energy term was elusive and, furthermore, the behaviour between ~80K and T_C is very complex.

This complicated behaviour of the parent wafer prohibited quantitative analysis from hysteresis measurements, but we were able to see clearly the effects of patterning in the remanence data from the patterned samples, qualitatively at least. The remanent magnetization curves along the [110] and [$\bar{1}$10] orientations are shown for all three samples in figure 3.9 and the remanences for all four directions for the two patterned samples are shown in figures 3.10 and 3.11. For the sample with stripes orientated along the [$\bar{1}$10] direction — the easy axis in the un-patterned material — the [110] direction, which is the hardest of the main axes, has been hardened as we had expected. For the sample with the stripes along the [110] direction — 90° to the usual easy axis — we find that the easy axis and hard axis have flipped; the stripe direction is now easier than the [$\bar{1}$10] direction for all temperatures (though the [100] and [010] axes dominate below about 60K). Qualitatively, the effects of patterning in

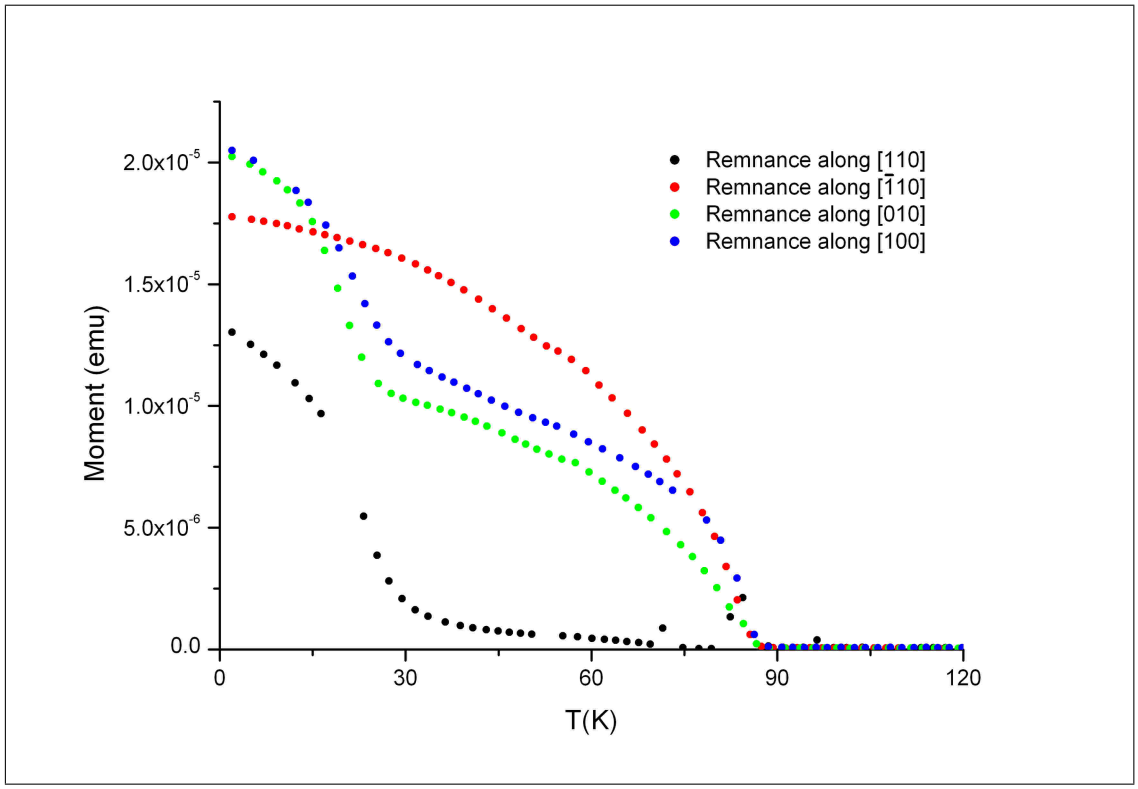

Fig. 3.8 — Remanent magnetization along all four in-plane directions for the control sample, which is an un-patterned, 25nm $(Ga_{0.05},Mn_{0.95})As$ film grown on GaAs(001). The sample has been baked for ∼3 hours at 180°C during fabrication. The remanence curves are mostly as expected for a film of this type.

these samples are very pronounced. Again there is significant splitting of the [100] and [010] remanent magnetizations, in particular for the stripes patterned along the [110] direction. In both patterned samples the total signal is ∼35% weaker than for the control sample, consistent with the volume of (Ga,Mn)As that has been etched away.

3.5.3 Summary

In summary, the effects of patterning 1µm stripes along the [$\bar{1}$10] and [110] crystallographic directions were qualitatively very evident in remanence data but we were unable to extract quantitatively the cubic and uniaxial anisotropy coefficients for the two patterned samples and a control sample due to the complex magnetic anisotropy of the parent wafer. Remanence data from the three samples show very clearly that narrow stripes orientated along a particular direction lead to a lowering of the magnetic anisotropy energy density along that direction.

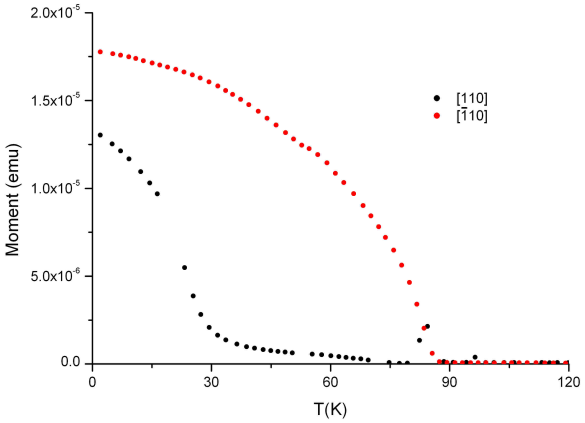

(a) Control sample

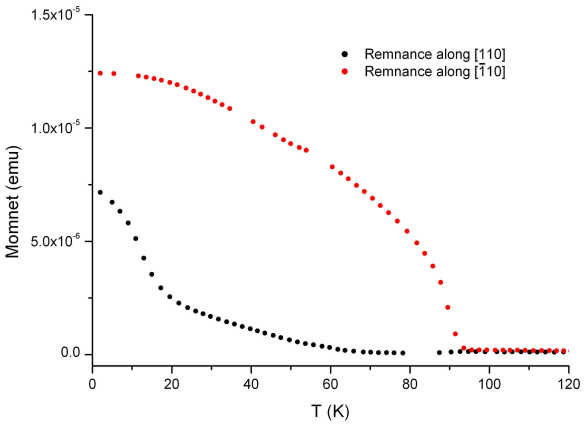

(b) $\bar{1}10$ sample

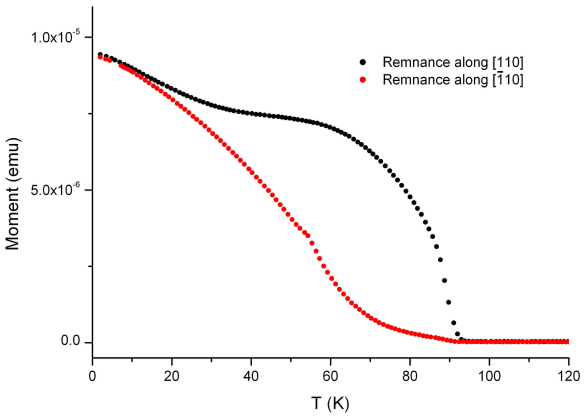

(c) 110 sample

Fig. 3.9 — Remanent magnetization along the $[\bar{1}10]$ and [110] directions for the samples with 1µm gratings (including the unpatterned, control sample).

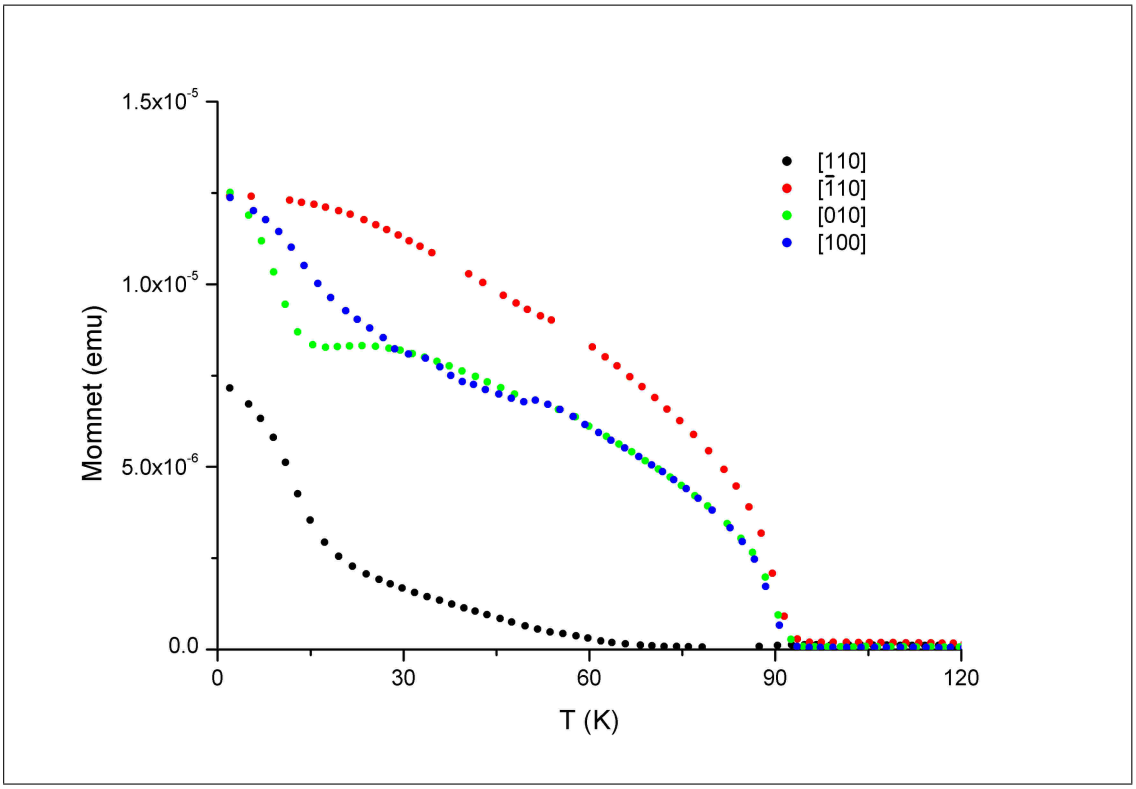

Fig. 3.10 — Remanence curves along all four in-plane crystallographic directions for *CSK139[1̄10]*, with 1µm gratings aligned to the [1̄10] axis.

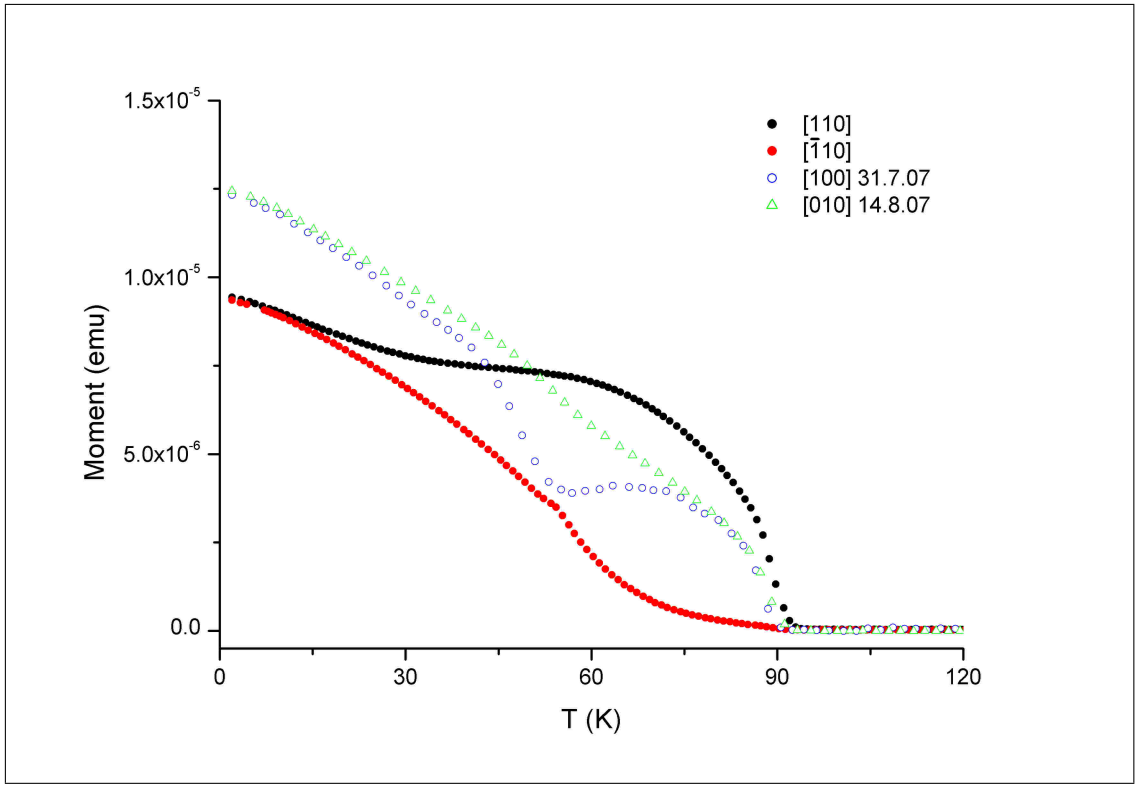

Fig. 3.11 — Remanence curves along all four directions for *CSK139[110]*, with 1µm gratings aligned to the [110] axis.

3.6 Results & Analysis — 750nm Gratings

3.6.1 Sample Details

A subsequent set of gratings was fabricated on wafer number Mn378, nominally identical to wafer Mn289 used for the 1µm gratings, that is a 25nm $(Ga_{0.95},Mn_{0.05})As$ thin film grown on GaAs(001). For the two patterned samples the design was the same, again comprising stripes 1µm long having a period of 1.2µm, but the development time was increased in order to produce wider trenches between the (Ga,Mn)As stripes and therefore narrower stripes. The intention was to have (Ga,Mn)As stripes 500nm wide separated by 700nm. These samples were baked for $\sim 1\frac{1}{4}$ hours at 180° during fabrication. The samples are named *CSK140[110]*, *CSK140[$\bar{1}$10]* and *CSK140[control]*.

An AFM image of part of one of the patterned samples is shown in figure 3.12 with a line analysis in figure 3.13. The stripes are in fact 700-750nm wide, separated by 450-500nm. The etches are again ∼60nm, deep enough to have gone right through the (Ga,Mn)As layer and into the substrate. This time the two patterned samples had about 45% of their (Ga,Mn)As layer etched away compared with the control sample. The volume of (Ga,Mn)As in the control sample is approximately $5\text{mm} \times 5\text{mm} \times 25\text{nm}$ or $6.25 \times 10^{-13}\text{m}^3$ and in the patterned samples, therefore, it is approximately $0.55 \times 6.25 \times 10^{-13}\text{m}^3$.

There is a 5° misalignment between the stripes and the crystallographic axes in the patterned samples; the gratings nominally along the [110] direction are tilted 5° towards the [010] direction whilst the [$\bar{1}$10] gratings are tilted 5° towards [100].

Shape Anisotropy

The shape anisotropy in these samples was calculated using the rectangular prism model [15] introduced in section 3.2 and the dimensions given above. For these structures the shape anisotropy is around 50 Jm^{-3} at 2 K and ∼10 Jm^{-3} at 100 K; when compared with the magnetocrystalline anisotropies extracted from hysteresis data,

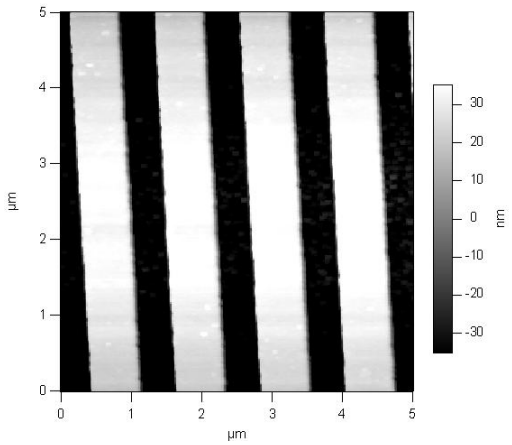

Fig. 3.12 — AFM image of the 750nm gratings along the [$\bar{1}$10] direction. The lighter regions are the (Ga,Mn)As stripes; the dark lines are the etched trenches.

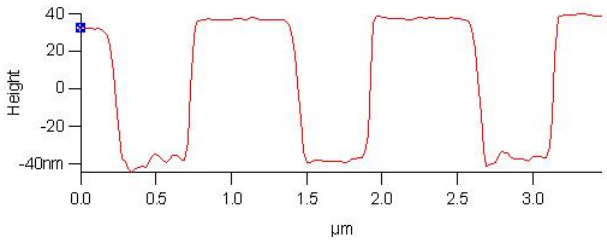

Fig. 3.13 — Height profile across the middle of figure 3.12. The (Ga,Mn)As stripes are 700-750nm wide, separated by 450-500nm. The etch depth is 65-70nm, more than enough to etch right down through the (Ga,Mn)As film and into the substrate.

presented later, it is clear that the shape anisotropy is very small.

Etch Profile

The etch profile for these stripes was verified by cleaving the samples after all measurements had been completed and imaging the cross-sections by scanning electron microscopy. The profiles are anisotropic in the manner expected (see section 3.3). Cross-sectional images are shown in figures 3.14 and 3.15 for the stripes along $[\bar{1}10]$ and [110] respectively. The over-cut profile in the $[\bar{1}10]$ sample is easily seen in the cleaved cross-section. It was not so easy to obtain clear images of the [110] sample etch profile but images with the sample tilted by about eight degrees, showing both the cleaved face and top surface of the sample, reveal a definite undercut profile, although it is not easy to discern this in print. The curvature of the stripes and sample surface in the [110] image is caused by the sample stage drifting during the exposure of the image.

Based on the strain relaxation calculations for undercut and overcut etch profiles presented in section 3.3, we can expect that the incorporated growth strain will be released more in the sample with stripes along [110] and although we don't have quantitative simulation data we might expect to see that the effect of patterning is stronger in this sample.

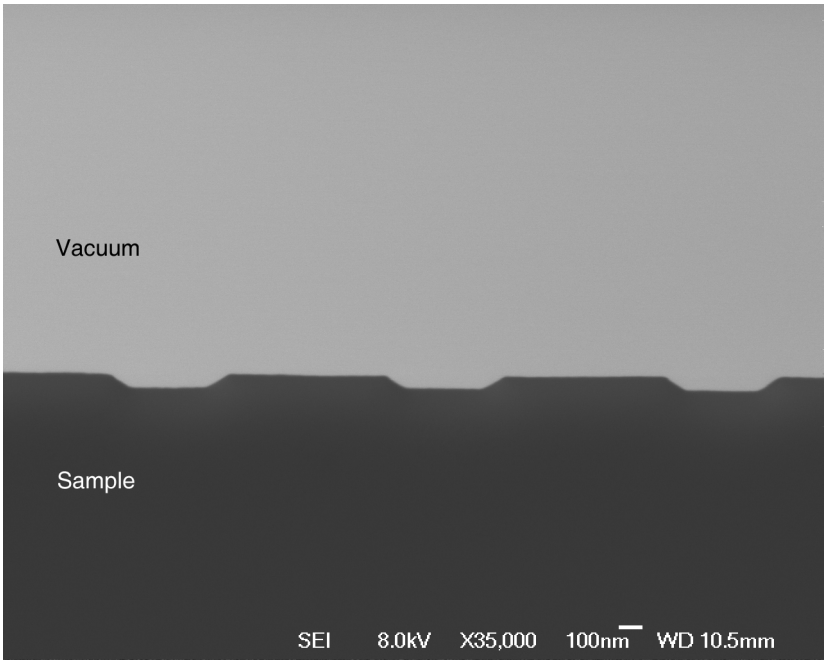

(a) Full SEM image

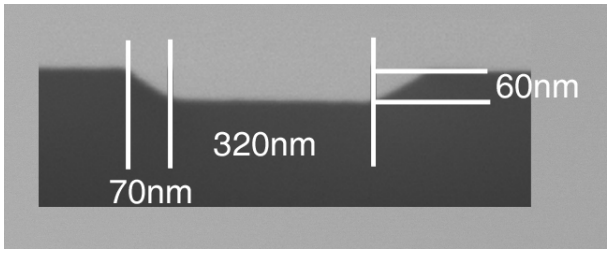

(b) Detail

Fig. 3.14 — Cross-sectional SEM image of 750nm stripes along the $[\bar{1}10]$ direction, showing distinct over-cut profile.

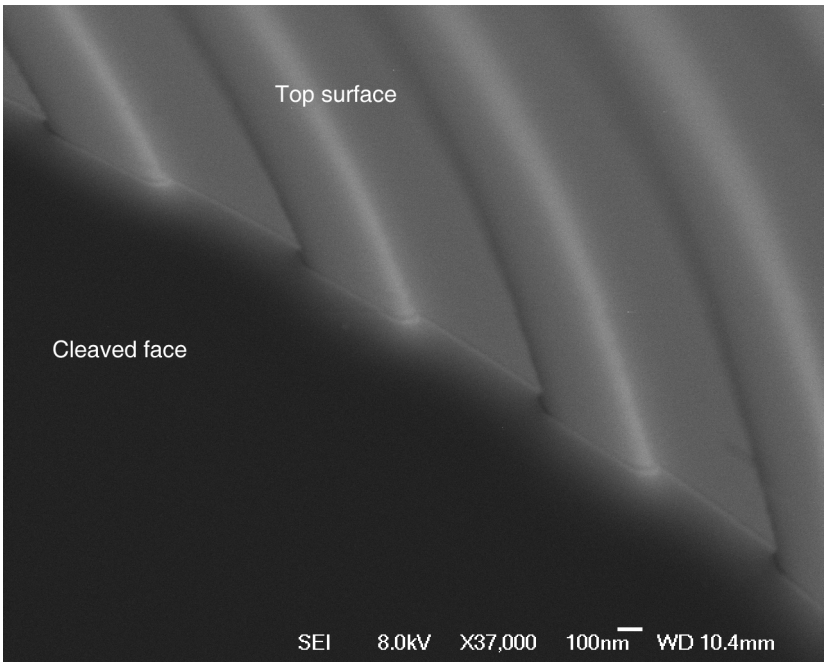

(a) Full SEM image

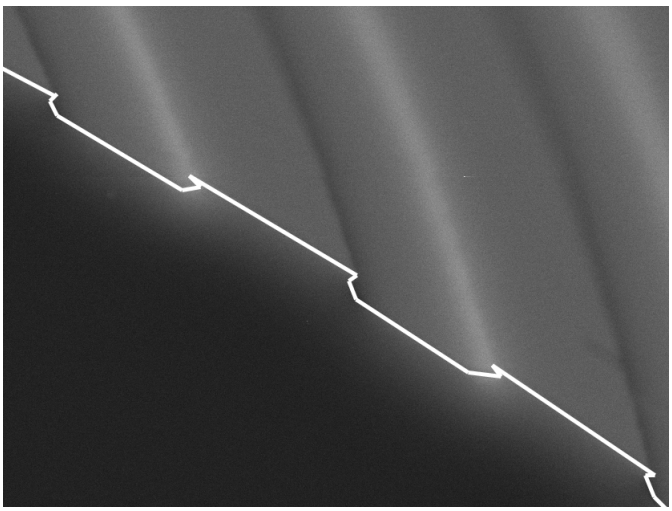

(b) Detail

Fig. 3.15 — Tilted SEM image of 750nm stripes along the [110] direction showing both the cleaved face and the top surface. Although difficult to discern in print, the profile is undercut as illustrated in (b). The curvature in the images is due to the sample stage drifting during the exposure of the image.

3.6.2 Remanent Magnetization Measurements

Overview

The remanent magnetization curves for the control sample along all four in-plane directions are shown in figure 3.16. Although somewhat different from the control sample from the 1µm sample set (figure 3.8) this does, at first sight, seem easier to understand in terms of a single-domain model, at least at lower temperatures. The anisotropy appears to be uniaxial at all temperatures, with the easy axis along $[\bar{1}10]$ up to almost 100K, giving way to [110] above this. Although this turns out to be something of a simplification, with the full behaviour described in detail below, this simple picture is a good starting point. The Curie temperature is just above 120K.

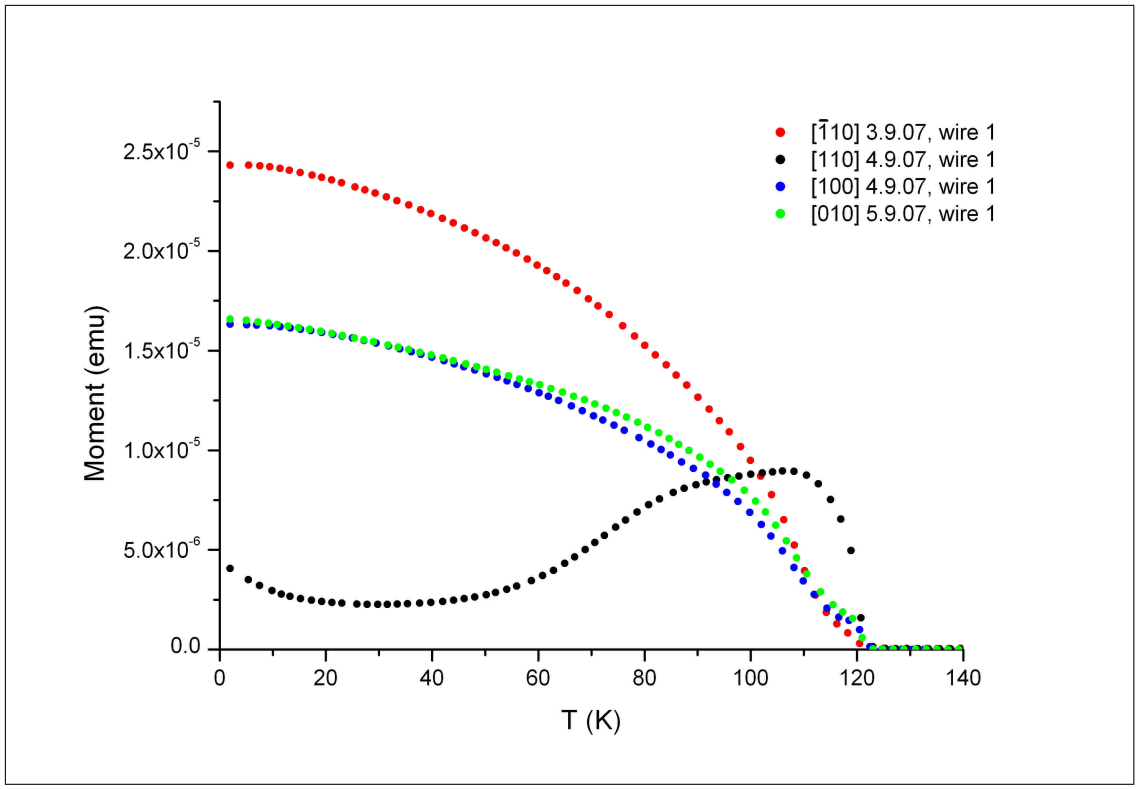

Fig. 3.16 — Remanent magnetization along all four in-plane directions for the control sample from the 750nm gratings set, which is an un-patterned, 25nm $(Ga_{0.05},Mn_{0.95})As$ film grown on GaAs(001). The sample was baked for $\sim 1\frac{1}{4}$ hours at 180°C during fabrication.

The remanent magnetizations along the [110] and $[\bar{1}10]$ directions for all three

samples are shown in figure 3.17. The effects of patterning are striking; patterning stripes along the [$\bar{1}$10] direction has 'hardened' the hard axis with the result that [$\bar{1}$10] is now the easy axis at all temperatures, whereas patterning along the [110] direction has clearly made this the easy axis over the whole temperature range, with [$\bar{1}$10] now the hard axis (in fact these interpretations also turn out to be simplifications, as detailed below, but the key observations are the same). As before the total signal is weaker in the patterned samples, consistent with the volume of (Ga,Mn)As that has been etched away.

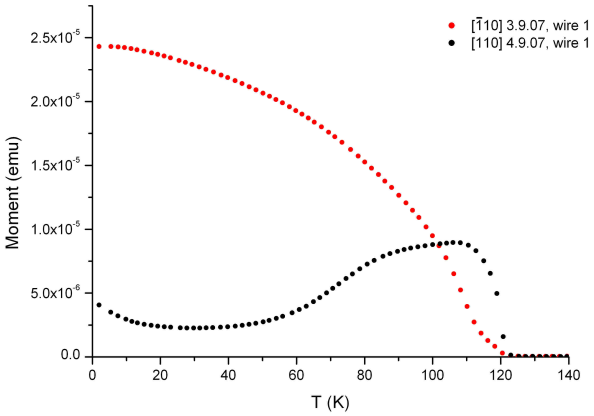

(a) Control sample

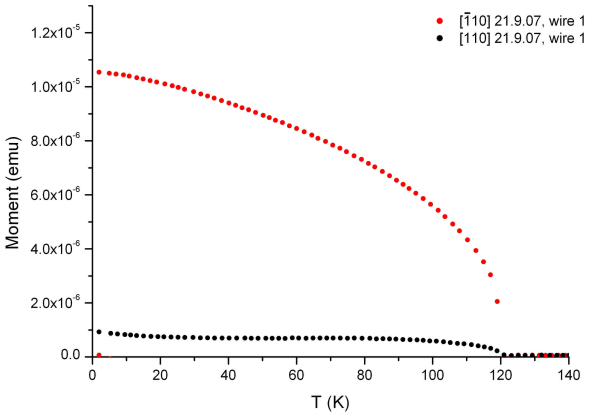

(b) $\bar{1}10$ sample

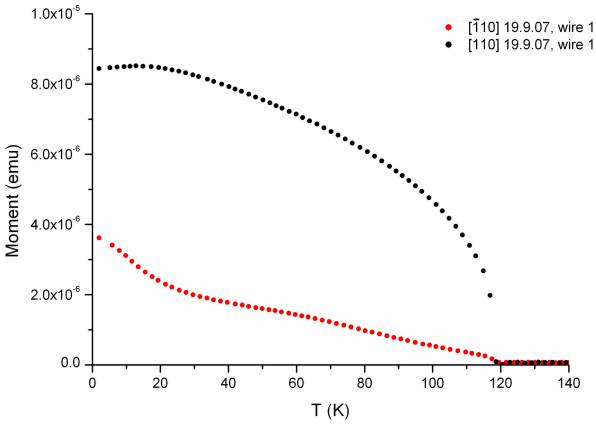

(c) 110 sample

Fig. 3.17 — Remanent magnetization along the [$\bar{1}$10] and [110] directions for each of the three samples from the 750nm-gratings set.

Detailed analysis - control sample

The initial interpretation of figure 3.16 was that the parent wafer exhibits uniaxial, single-domain behaviour with the easy axis along [$\bar{1}$10] below about 60K giving way to an easy axis along [110] towards T_C, with some rotation of the easy axis between ∼60K and ∼112K. Favourably this sample shows good agreement between the two cubic directions at all temperatures which simplifies the analysis compared with the 1µm sample set. On close inspection, however, the behaviour requires some unravelling, particularly in the intermediate temperature range.

Below 60K the saturation magnetizations $M_{S,1} = \sqrt{{M_{110}}^2 + {M_{\bar{1}10}}^2}$ and $M_{S,2} = \sqrt{{M_{100}}^2 + {M_{010}}^2}$ are roughly equal (these are confirmed to be the correct net magnetization by comparing against the saturation magnetization from hysteresis measurements, presented later) and $M_{100} \approx M_{010} \approx M_{\bar{1}10}/\sqrt{2}$. This indicates a uniaxial easy axis along the [$\bar{1}$10] direction below 60K, for which the projection of the magnetization onto the [110] direction is expected to be zero. The non-zero remanence seen in the [110] measurement below 60K can be explained by a ∼5° misalignment of the sample in the magnetometer. Above 60K the remanence along [$\bar{1}$10] falls away from the net magnetization $M_{S,1}$ and the remanences along the other 3 directions increase in proportion to it. We can be confident that $M_{S,1}$ is a good representation of the net magnetization at *all* temperatures by comparing against the saturation magnetization from hysteresis measurements and because $M_{S,1}(T)$ is almost identical for each of the three samples when scaled for the volume of (Ga,Mn)As etched (shown in figure 3.27). Therefore we interpret the behaviour above 60K as a rotation of the easy axis away from [$\bar{1}$10] and since $M_{[100]} \approx M_{[010]}$ the sample must become biaxial as the easy axis departs from the [$\bar{1}$10] direction, with the axes symmetrical about [$\bar{1}$10]. The biaxial axes open up, passing through 45° (*cubic* symmetry) at ∼100K and recombining at 90° to give a uniaxial axis along [110] near T_C.

We must go one step further to fully explain the data. If the sample remained single-domain as the magnetization rotated we would expect larger remanent mag-

netization along the [100] and [010] directions. Furthermore all other calculations of M_S — that is $M_{S,2}$ and $M_{S,A-D}$ (see section 3.4.1) — involve either or both of the [100] and [010] remanences and they are each clearly non-physical (figure 3.18), having values below remanent magnetization at certain ranges of temperature[3]. Instead we must allow the sample to split into domains in the biaxial regime, with equivalence along each direction, i.e. roughly equal magnetization along each axis. The projection of the magnetization onto the [110] and [$\bar{1}$10] axes is not changed compared with being single-domain along either direction due to the symmetry of the axes around [$\bar{1}$10] and the remanences along [100] and [010] are equal but smaller than would be expected for a single-domain system. If this multi-domain picture is correct we expect at the intermediate temperature where the axes are cubic to find $M_{[110]} = M_{[\bar{1}10]} = M_{S,1}/\sqrt{2}$ and $M_{[100]} = M_{[010]} = M_{S,1}/2$. Indeed this is the case, occurring at $T \sim$100K, confirming that this model is likely to be correct.

Further verification comes from extracting the orientations of the easy axes with temperature from equation 3.5, the results of which are shown in figure 3.19, although a slight modification of the model is required. We learn that the sample is in fact biaxial at *all* temperatures, with the magnetization starting very close to [$\bar{1}$10], remaining here up to ∼60K then rotating towards [110], finishing up in fact about 10° off this axis just below T_C. At ∼100K the angle is 45° so the symmetry is cubic along [100] and [010] at this temperature, confirming our model. The angles extracted from the [100] and [010] data appear too small, which is consistent with the sample splitting into domains, which in fact appears to be the case at all temperatures. A summary of the evolution of the easy axis with temperature is shown schematically in figure 3.20.

Aside - novel remanence measurements on the control sample

In order to test the idea that the sample was splitting into domains above ∼60K two further remanence measurements were made on the control sample along the [110]

[3] $M_{S,2}$, $M_{S,B}$ and $M_{S,C}$ are reasonable below ∼60K

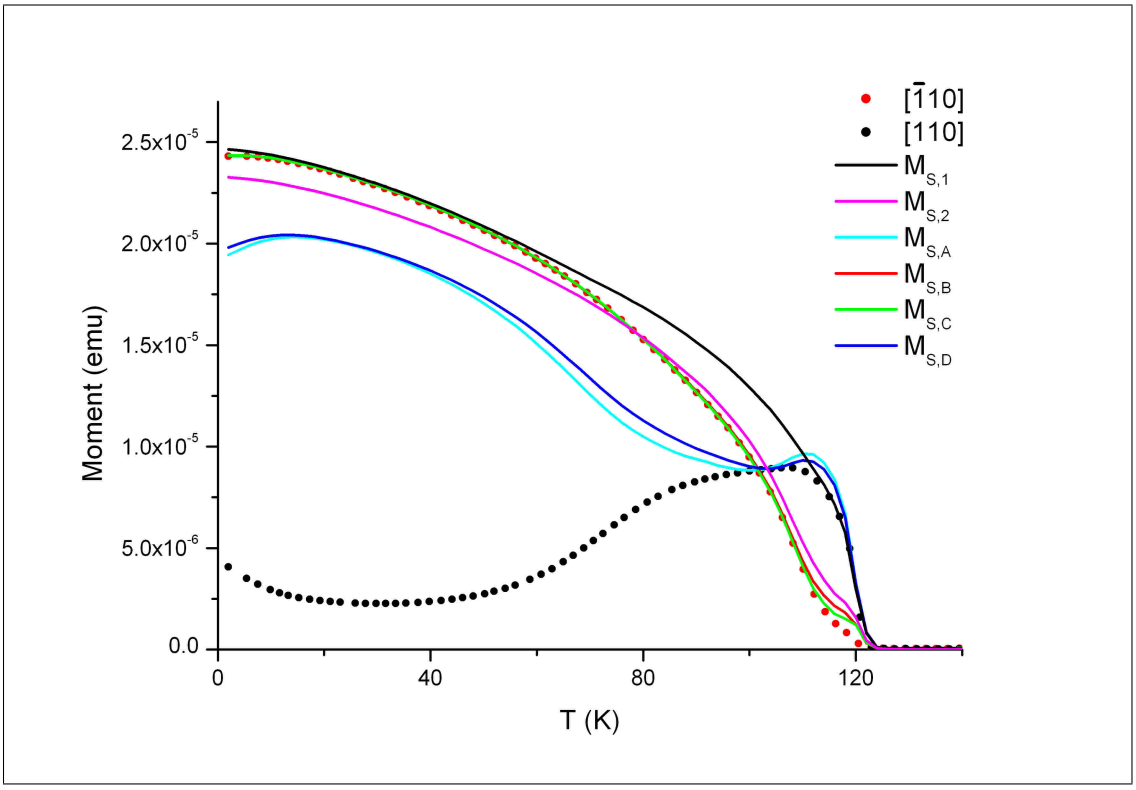

Fig. 3.18 — All possible saturation magnetizations given by equations 3.2, 3.3 and 3.4 for the control sample from the 750nm-gratings set.

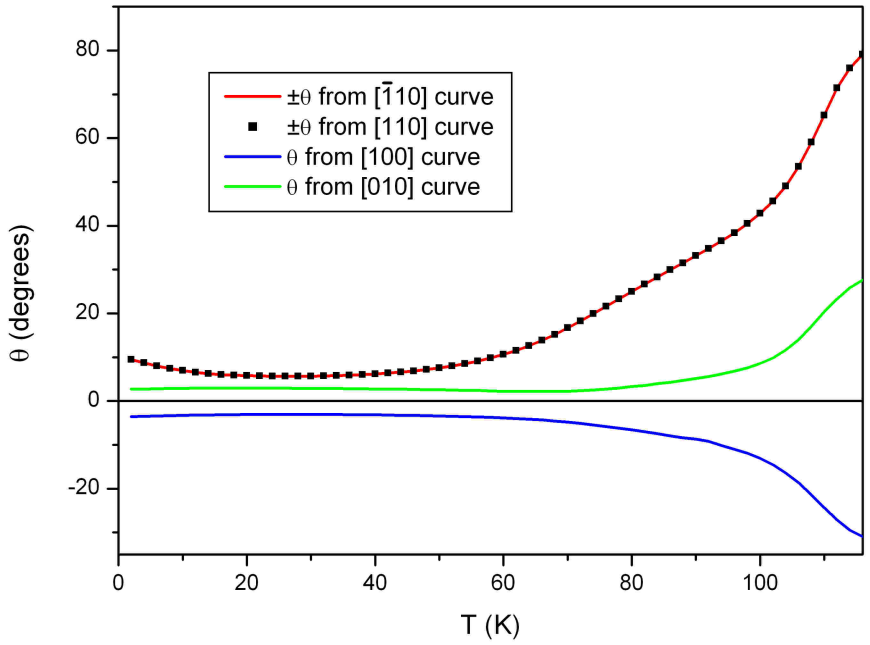

Fig. 3.19 — Orientation(s) of the easy axis(-es) for the control sample from the 750nm-grating set, extracted from the remanence data along each of the four in-plane directions.

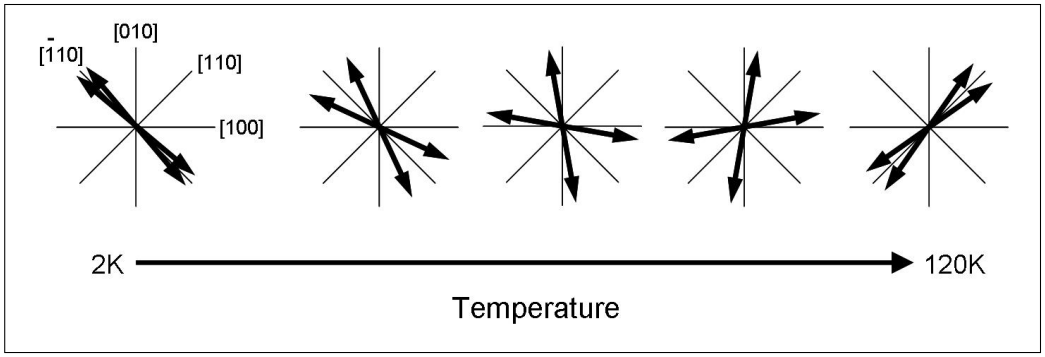

Fig. 3.20 — Schematic of the evolution of the easy axes with temperature for the control sample from the 750nm-grating set. The sample splits into domains whilst it is biaxial.

direction. An alternative explanation that had been considered was that the sample remains single-domain at all temperatures but gets stuck in local energy minima as the anisotropy crosses over at ∼105K, although it wasn't clear that this explanation would explain the data completely. We hoped that these additional remanence measurements would provide clarification of the domains proposition, and in the process we found an interesting result in that the magnetization was seen to spontaneously order itself even in the absence of an external field.

The first test was to field-cool the sample from 150K to just 112K, above the easy-axis crossover, then measure remanence in zero applied field as the sample was warmed from 112K. If the local-minimum explanation for the full remanence curve was correct we would expect the magnetization to fall into the global minimum in this restricted measurement. Instead the remanence in this measurement was just the same as for the 'normal' remance measurement, confirming that the magnetization is not stuck in local minima after the anisotropy cross-over.

The second test was to field-cool from 150K to 2K, then measure remanence as the sample was warmed to 112K then continue measuring whilst cooling back down to, say, 60K. If the sample was splitting into domains it was expected that it should stay in domains when cooled back down, giving different remanence traces for the up-sweep and down-sweep. The results of these measurements were also identical to the 'normal' remanence curves which unfortunately doesn't confirm that the sample is splitting into domains, but it doesn't necessarily mean that it isn't. It is possible that the sample splits into domains but goes back to single-domain when cooled, and this is the interpretation that we favour. This measurement was repeated, field-cooling to 2K but this time measuring remanence whilst warming to 135K, that is *above* T_C, and back down to 60K. Remarkably the remanence curve from this measurement was identical to the previous curves which indicates that the intrinsic magnetic anisotropy of this material is strong enough to overcome the magnetic disorder and create spontaneous magnetization when the sample is cooled through T_C, even in the absence of any

external field.

Detailed analysis - [$\bar{1}$10] sample

The remanent magnetization curves along all four in-plane orientations for the sample with 750nm gratings aligned along the [$\bar{1}$10] direction are shown in figure 3.21. The orientation of the magnetization was extracted in the same way as for the control sample, with the results presented in figure 3.22 up to the Curie temperature.

I interpret these data as coming from a single-domain sample having a uniaxial axis orientated along the *stripe direction* at all temperatures — that is 5° off the [$\bar{1}$10] direction (see schematic in figure 3.23). This fully explains all features of the remanence data. With the easy axis along the stripe direction, i.e. $\theta = 5°$, we can account for the splitting of the [100] and [010] traces (with [100] being the higher of the two), we expect non-zero [110] and we expect [$\bar{1}$10] to be very nearly M_S, as explained in the following table. This is corroborated by the hysteresis loop measurements and discussed further in that section. This easy axis is allowed by the single-domain model if an additional term is incorporated into equation 3.1 at some offset angle (θ+Δ). The differences between the curves in figure 3.22 can be explained by imperfect alignment of the sample between measurements.

The net magnetizations $M_{S,1}$, $M_{S,B}$ and $M_{S,C}$, and to a slightly lesser extent $M_{S,A}$, $M_{S,D}$ and $M_{S,2}$, all give reasonable-looking results and $M_{S,1}$ is almost identical to that from the control sample and the [110] sample when scaled for the volume of (Ga,Mn)As etched in the patterned samples — see figure 3.27.

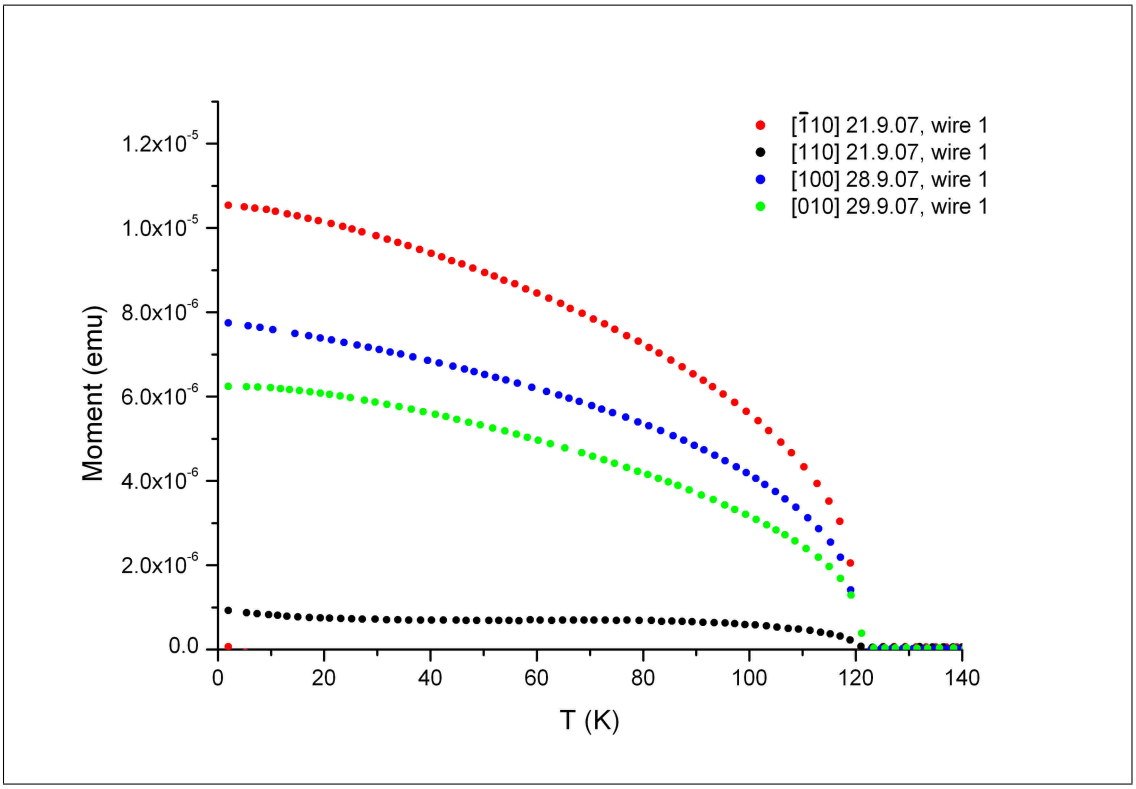

Fig. 3.21 — Remanence curves along all four in-plane crystallographic directions for *CSK140[1̄10]*, with 750nm gratings aligned to the [1̄10] axis.

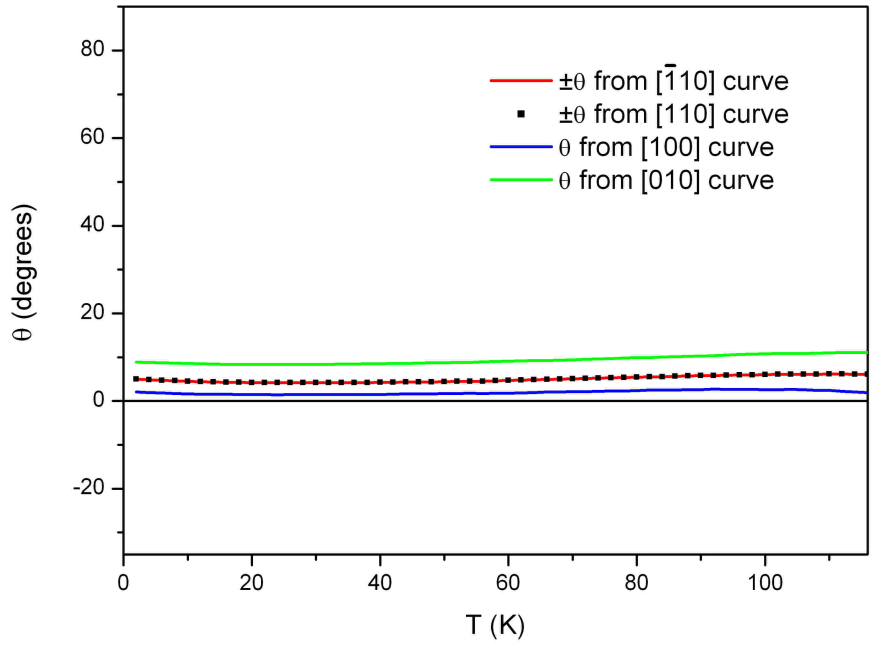

Fig. 3.22 — Orientation(s) of the easy axis(-es) for the sample with 750nm stripes along [$\bar{1}$10], extracted from remanence data along each of the four in-plane directions.

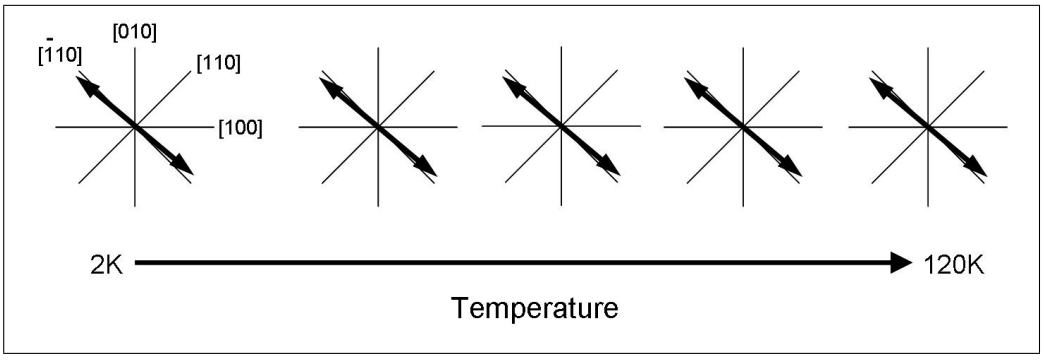

Fig. 3.23 — Schematic of the evolution of the easy axes with temperature for the sample with 750nm gratings along [$\bar{1}$10]. The easy axis is along the stripe direction, that is 5° off the [$\bar{1}$10] axis, at all temperatures.

Measurement direction	Easy axis along [$\bar{1}$10]		Easy axis along stripe	
	α	$M_S \cos\alpha$	α	$M_S \cos\alpha$
[$\bar{1}$10]	0	$\boldsymbol{M_S}$	5°	$\mathbf{0.996}\boldsymbol{M_S}$
[100]	45°	$\mathbf{0.71}\boldsymbol{M_S}$	40°	$\mathbf{0.77}\boldsymbol{M_S}$
[010]	-45°	$\mathbf{0.71}\boldsymbol{M_S}$	-50°	$\mathbf{0.64}\boldsymbol{M_S}$
[110]	90°	$\mathbf{0}$	85°	$\mathbf{0.09}\boldsymbol{M_S}$

Table 3.1 — Predicted remanent magnetization along each of the in-plane crystallographic axes when the magnetization is along [$\bar{1}$10] ($\theta = 0$) and along the stripe direction ($\theta = 5°$). α is the angle between the magnetization and the measurement direction. With the magnetization along the stripe direction we can account for the splitting of the remanence measurements along [100] and [010] and for the non-zero remanence along [110].

Detailed analysis - [110] sample

The remanent magnetizations for the sample with 750nm stripes along [110] are shown in figure 3.24 and the orientations of the magnetization shown in figure 3.25. The saturation magnetization $M_{S,1} = \sqrt{{M_{[110]}}^2 + {M_{[\bar{1}10]}}^2}$ is also shown on the remanence plot. The effects of patterning are dramatic — the easy and hard axes have flipped. In this sample [$\bar{1}$10] is now the 'hardest' of the four in-plane orientations at all temperatures. The easy axis starts ∼25° off [110] and rotates towards [110] as the temperature increases, ending up along the *stripe direction* (that is 5° off the crystallographic axis, as for the other patterned sample). The splitting of the [100] and [010] traces can again be explained by the easy axis being off the [110] direction at all temperatures. A schematic of the rotation of the easy axis with temperature is shown in figure 3.26. It should be noted that the single domain model presented earlier (equation 3.1) does not support uniaxial easy axes at arbitrary orientations due to the symmetry of the sine terms; the energy density is always symmetrical about [$\bar{1}$10] (and also, therefore, [110]) so, for example, an easy axis 25° off [110] must be complemented by another at -25°. The corollary is that, according to the model, the system is always biaxial unless the easy axis is exactly along [$\bar{1}$10] or [110] and therefore [100] and [010] are always

equivalent. However, we believe the behaviour is consistent with a single-domain, uniaxial sample at all temperatures, with the discrepancy between [100] and [010] caused by the misalignment of the stripes with respect to the [110] axis. If the 5° misalignment is incorporated into the single domain model, continuous rotation of a uniaxial easy axis is then allowed (equation 3.1 as it stands only allows symmetric rotation of biaxial axes, i.e. symmetrical opening or closing of 'scissors').

The net magnetization $M_{S,1}$ for each sample is presented in figure 3.27, showing very good agreement between the three samples, supporting our belief that $M_{S,1}$ is a good calculation of the net magnetization.

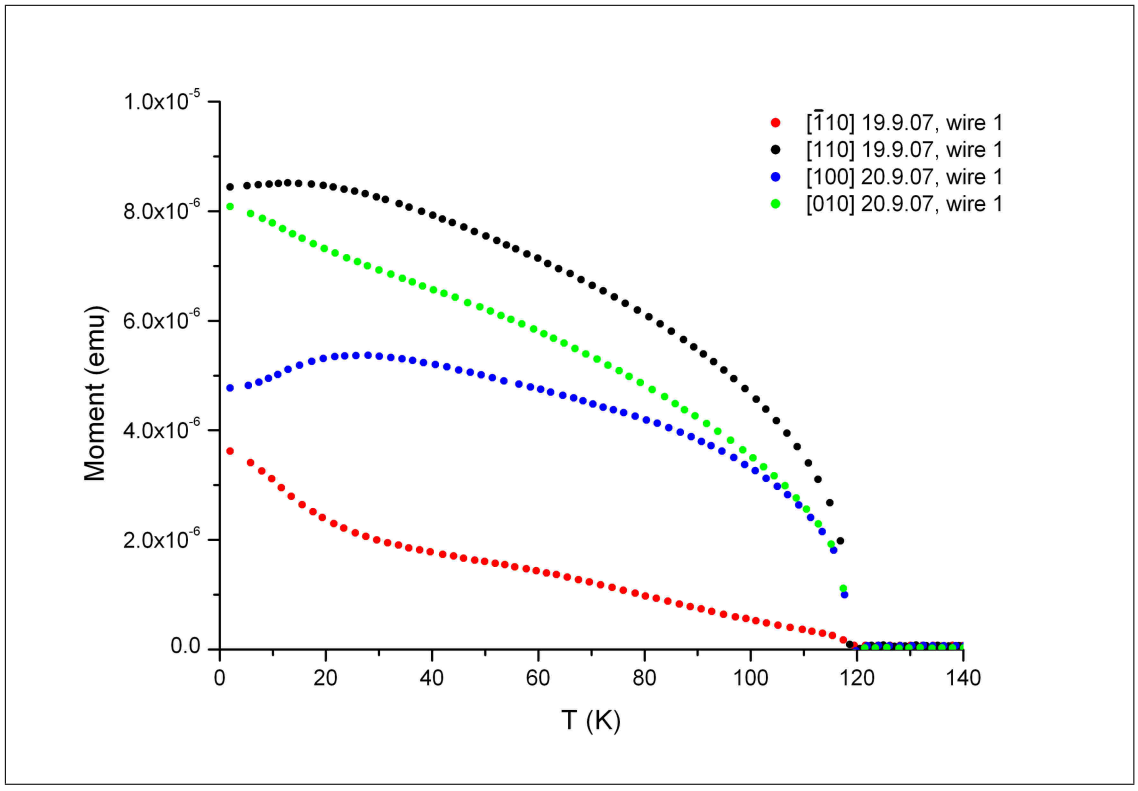

Fig. 3.24 — Remanence curves along all four in-plane crystallographic directions for *CSK140[110]*, with 750nm gratings aligned to the [110] axis.

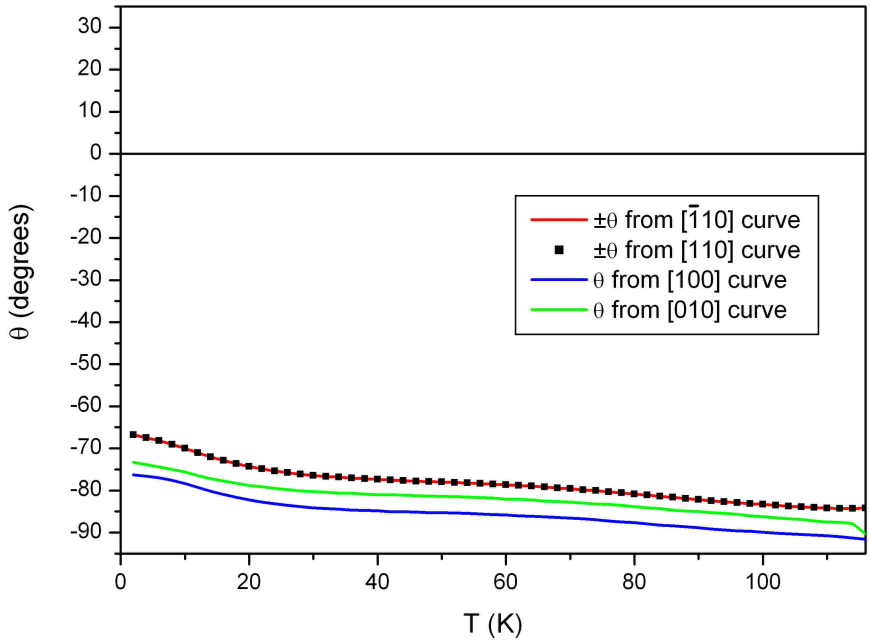

Fig. 3.25 — Orientation(s) of the easy axis(-es) for the sample with 750nm stripes along [110], extracted from remanence data along each of the four in-plane directions.

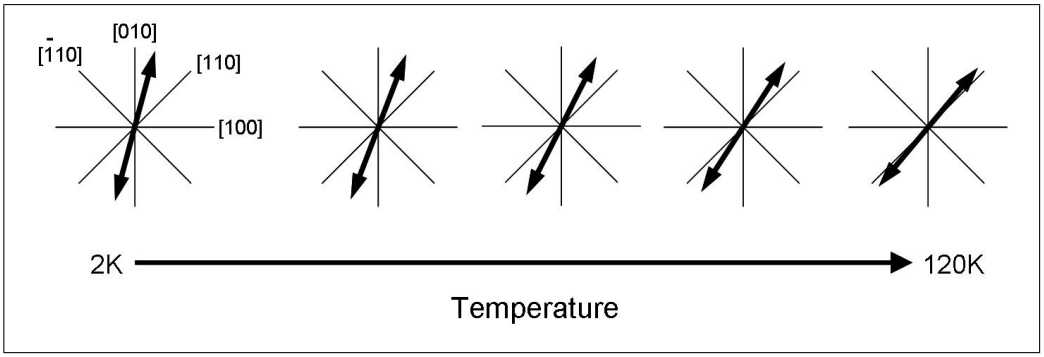

Fig. 3.26 — Schematic of the evolution of the easy axes with temperature for the sample with 750nm gratings along [110] (the angles have been exaggerated).

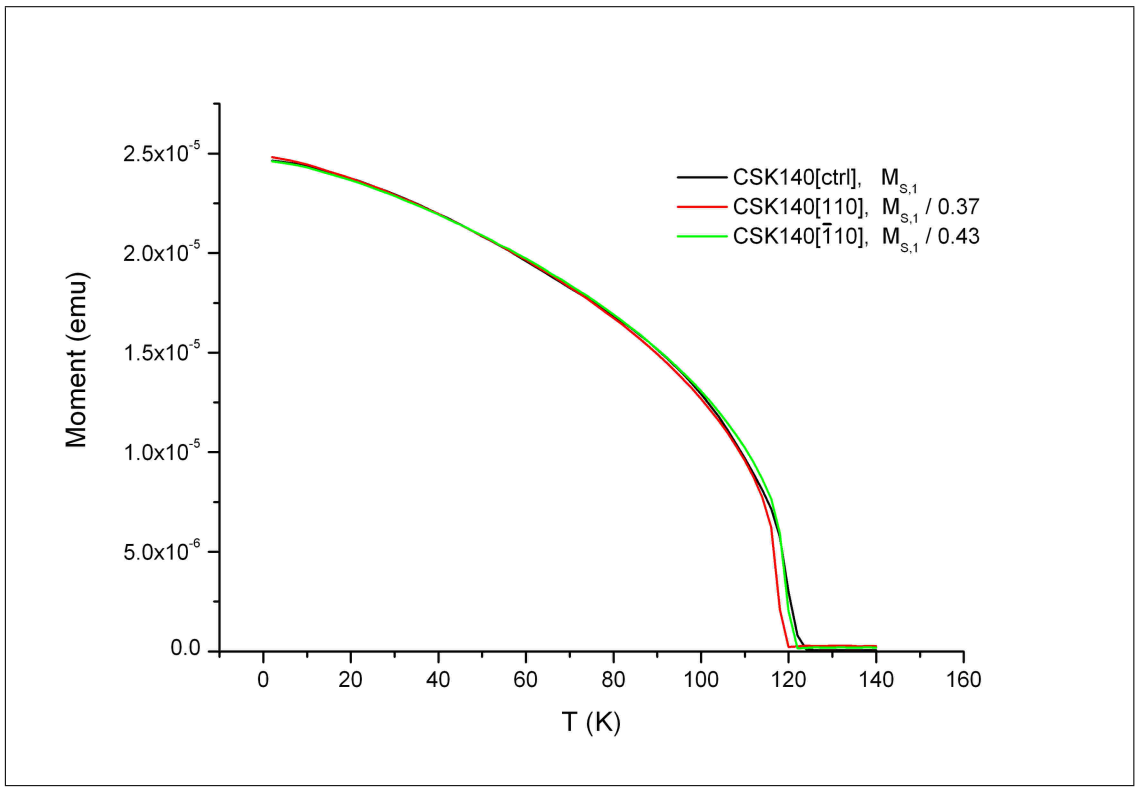

Fig. 3.27 — The net magnetization $M_{S,1}$ (see equation 3.2) for the control sample and the two patterned samples from the 750nm-grating set, showing good agreement between samples. The curves for the two patterned samples have been scaled by the volume of (Ga,Mn)As etched away.

3.6.3 Hysteresis Loop Measurements

I showed in section 3.4.2 how the anisotropy coefficients K_U and K_C can be evaluated from hard-axis hysteresis measurements by fitting either equation 3.12 or 3.13 to the data, depending on the orientation of the hard axis. For each sample we know the orientation of the hard axis from the remanence data; for the control sample and the sample patterned along $[\bar{1}10]$ the hard axis is along the [110] direction and the relevant equation for the fitting is 3.12, whereas for the [110] sample the hard axis is along $[\bar{1}10]$ and the relevant equation is 3.13. The M–H loops along the respective hard axes are shown for the three samples in figures 3.28, 3.29 and 3.30. For each sample the diamagnetic background was evaluated at each temperature and the average of these was subtracted from each loop.

The hysteresis loops for the control sample show typical hard-axis behaviour at the lower temperatures having curved M–H loops, i.e. there is a progressive rotation of the net magnetization of the sample, evolving towards easy-axis behaviour at higher temperatures where the magnetization quickly switches from one direction to the other. This is the behaviour we would expect to observe given the remanence results. There is a small amount of hysteresis at low temperatures, as shown in the inset of figure 3.28 which shows detail of the 2K measurement; this is most likely to be due to a slight misalignment of the sample in the magnetometer.

For the sample patterned along the $[\bar{1}10]$ direction the hard-axis hysteresis loops are shown in figure 3.29 and are somewhat different from those from the control sample. Once again the average diamagnetic background has been subtracted at each temperature. The loops from the patterned sample show much more curvature than those from the control sample which confirms that this hard axis is 'harder' than the control sample's, as we had already seen from the remanence data, and immediately suggests we should find a stronger K_U term in this sample. Hard-axis hysteresis loops for the sample patterned along the [110] direction are shown in figure 3.30. These show hard-axis behaviour in between that of the control sample and the sample patterned

along [$\bar{1}$10], as we would expect from the remanence data.

We can immediately make some inferences about the uniaxial anisotropy coefficients for each sample. At low field the gradient of the hysteresis loops comes from the first term in the two equations. If we assume that the cubic coefficient is constant between samples, and I will show in the detailed analysis that this is more-or-less the case, any change in gradient between samples at low field is directly due to a change in K_U. Low-field regions of the M–H loops are shown for 50 K in figure 3.31. We expect from the gradients to find that ($K_{U,[\bar{1}10]} > -K_{U,[110]} > K_{U,[\mathrm{ctrl}]}$) and that is exactly what comes out from the analysis which follows (summarized in figure 3.42 near the end of the chapter). 50 K was chosen arbitrarily. The same interpretation at 2 K gives very similar expectations.

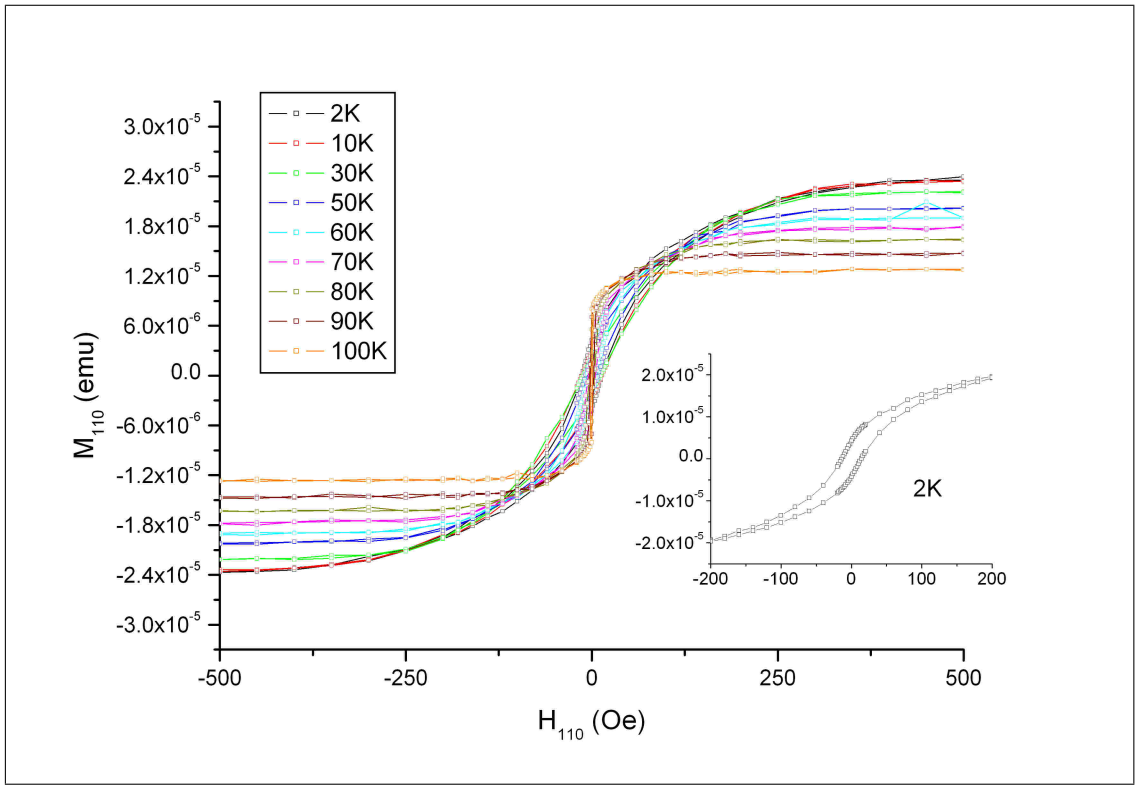

Fig. 3.28 — M–H loops along the [110] direction, the hard axis over most of the temperature range up to T_C, for the control sample from the 750nm-grating set, showing only $|H| <$ 500 Oe. Inset: the 2K loop between -200 Oe and +200 Oe showing a small amount of hysteresis, attributed to slight misalignment of the sample.

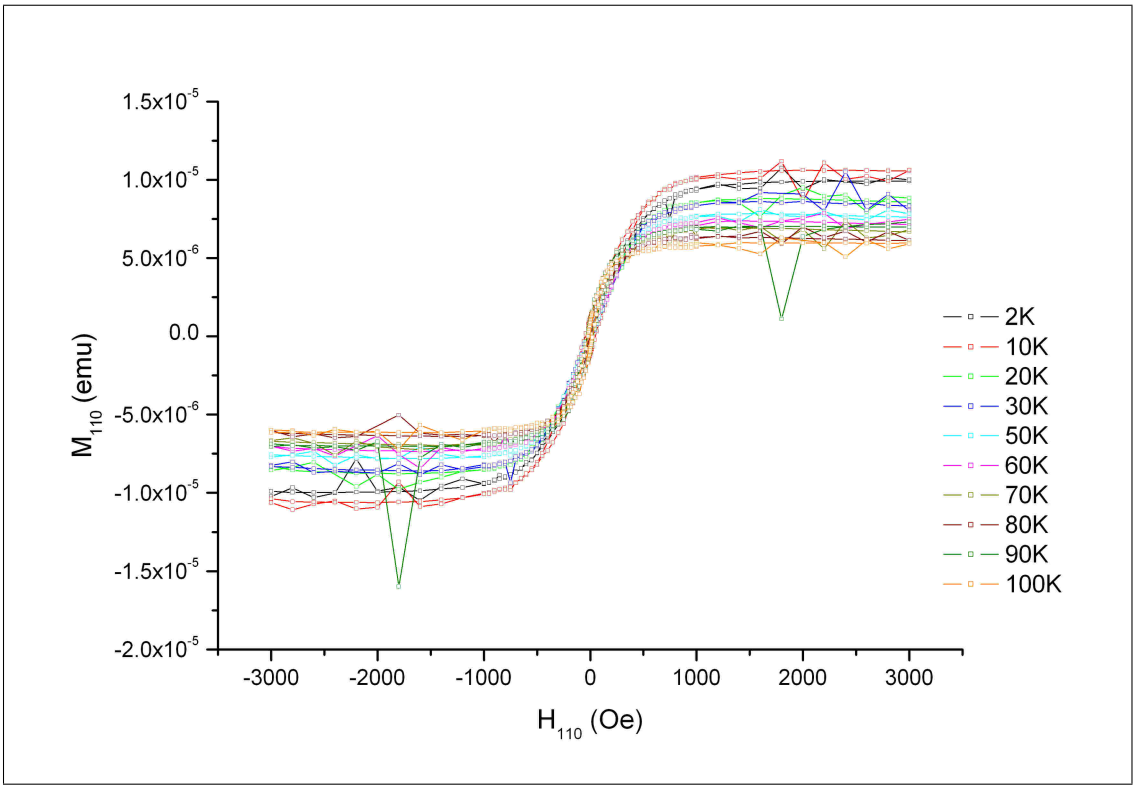

Fig. 3.29 — M–H loops along the [110] direction, the hard axis at all temperatures, for the sample with 750nm gratings aligned along $[\bar{1}10]$.

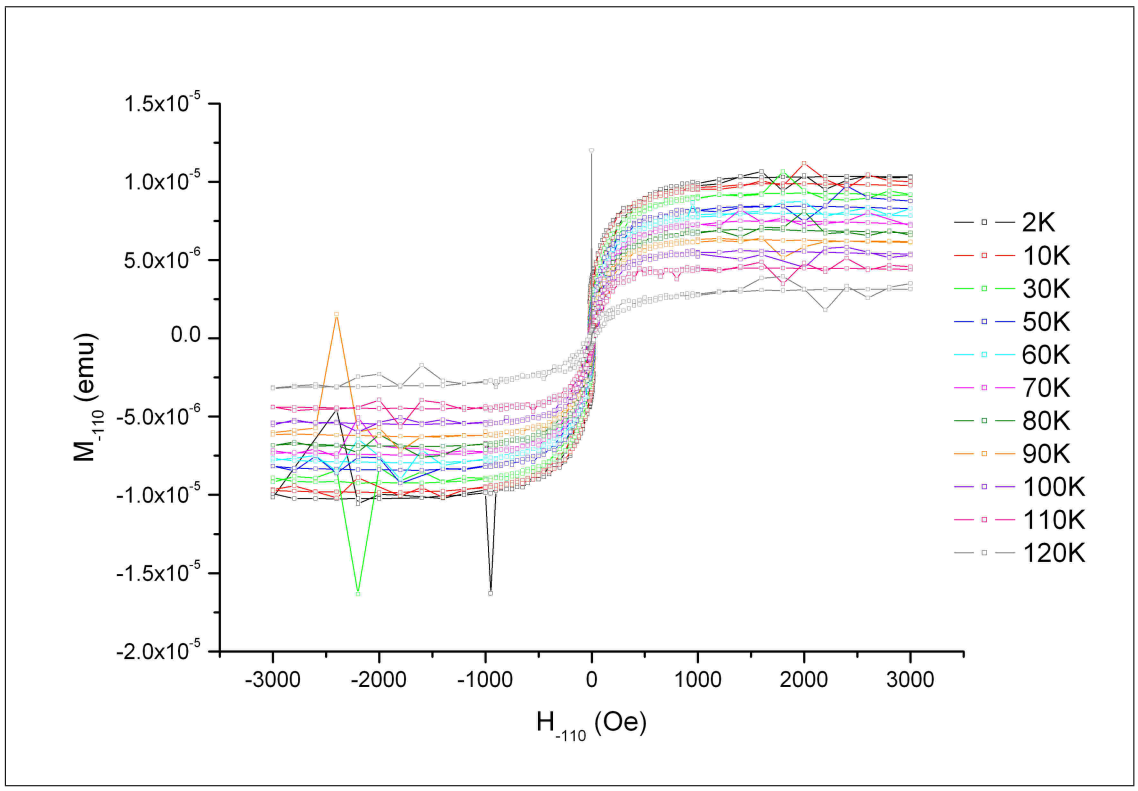

Fig. 3.30 — M–H loops along the $[\bar{1}10]$ direction, the hard axis at all temperatures, for the sample with 750nm gratings aligned along [110].

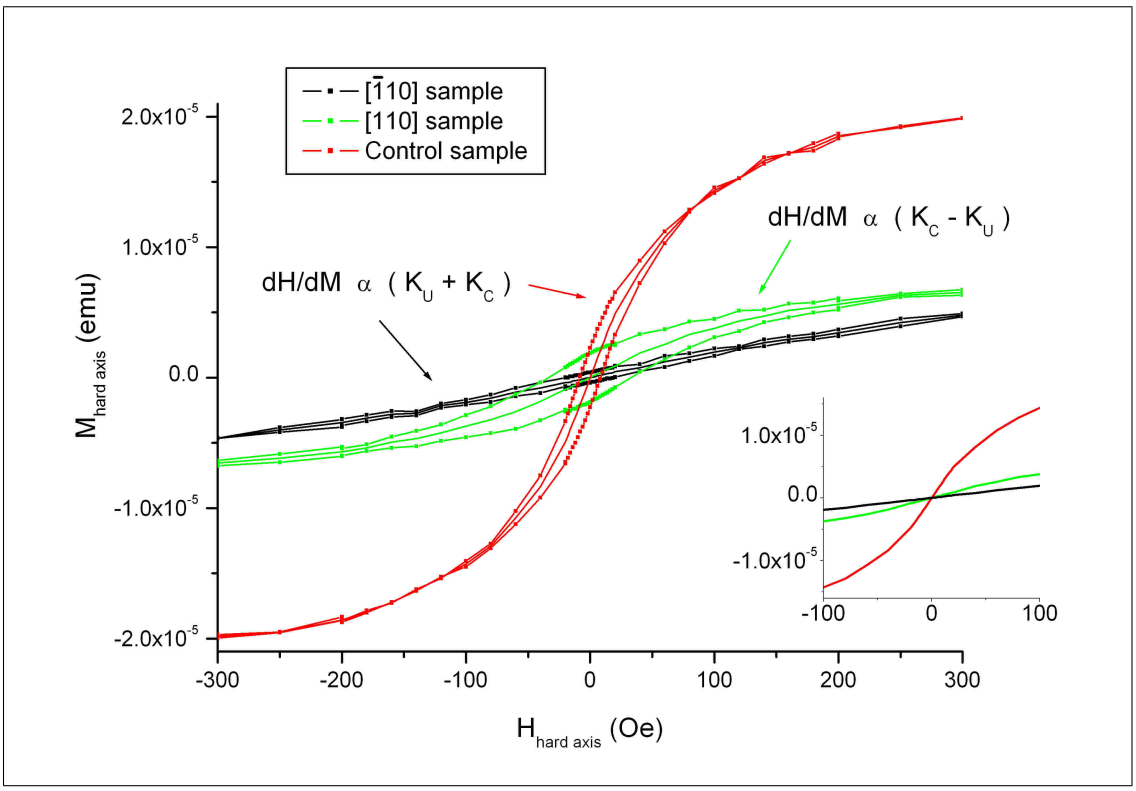

Fig. 3.31 — Low-field region of 50K hysteresis loops for all three samples from the 750 nm-grating set.

Control sample analysis

A caveat of using the fitting procedure described in section 3.4.2 is that we must be careful in our choice of the net magnetization, M_S, at each temperature because of the 4$^{\text{th}}$-power dependence of the second term in equations 3.12 and 3.13 on M_S. The first step in the analysis of the hysteresis data was, therefore, to determine an accurate net magnetization for each hysteresis loop. For each temperature a value of M_S was determined from averaging M between -3000 Oe and -1500 Oe and between 1500 Oe and 3000 Oe. A small amount of scatter was evident in these values (see figure 3.32) and so, because of the sensitivity of the 4$^{\text{th}}$-power dependence, a curve fit was performed to smooth the data. The simplest curve that gave a gave a good fit was equation 3.15, a curve based on the mean field approximation, which passed through the data very closely within error using $T_C = 117.6$ K and $M_S|_{T=0} = 2.43 \times 10^{-5}$ emu. Although I have used an expression based on the mean field approximation to smooth

the data, this is not an attempt to describe my sample with a mean field model; in addition the mean field approximation breaks down close to T_C, so the fact that the T_C used in the approximation (117.6 K) does not match T_C from the data (∼120 K) is inconsequential.

$$M_S = M_S|_{T=0} \left(1 - \frac{T}{T_C}\right)^{1/3} \tag{3.15}$$

As a further indication that this curve-fit was a good choice for M_S, the net magnetization $M_{S,1}$ from remanence data (section 3.6.2) was plotted on the same axes, which showed good agreement with the values from hysteresis data and the fitted curve. This is all shown in figure 3.32. It should be noted that it is no problem that $M_{S,1}$ from remanence data and the curve fit from hysteresis data are not identical, because the sample was removed from the SQUID magnetometer and re-installed between the two remanence curves and the hysteresis measurement, so there could well be a small misalignment which would be more than enough to account for this.

For each temperature, equation 3.12 was fitted to the corresponding hysteresis loop over an appropriate range of H to provide values for the cubic and uniaxial anisotropy coefficients, K_C and K_U respectively. The net magnetization used in the fitting was the curve-fit to the hysteresis data. It is worth saying at this point that it is no problem if the sample does split into domains along [100] and [010] at intermediate temperature ranges, because the fitting requires only $M_{[110]}$ and M_S which are unaffected by this.

Equation 3.12 is valid over the range $H < 2(K_U - K_C)/M_S$ but this range cannot be evaluated until the coefficients K_U and K_C are known; this presents us with a problem, since neither determining the range over which to perform the fitting, nor performing the fitting itself, can be done until the other has been done. In practice this turned out to be less of a problem than anticipated since, whatever range of H the fitting was performed over, $2(K_U - K_C)/M_S$ generally came out quite consistently. For those fits that satisfied $2(K_U - K_C)/M_S$, the resulting K_U and K_C were plotted as a function

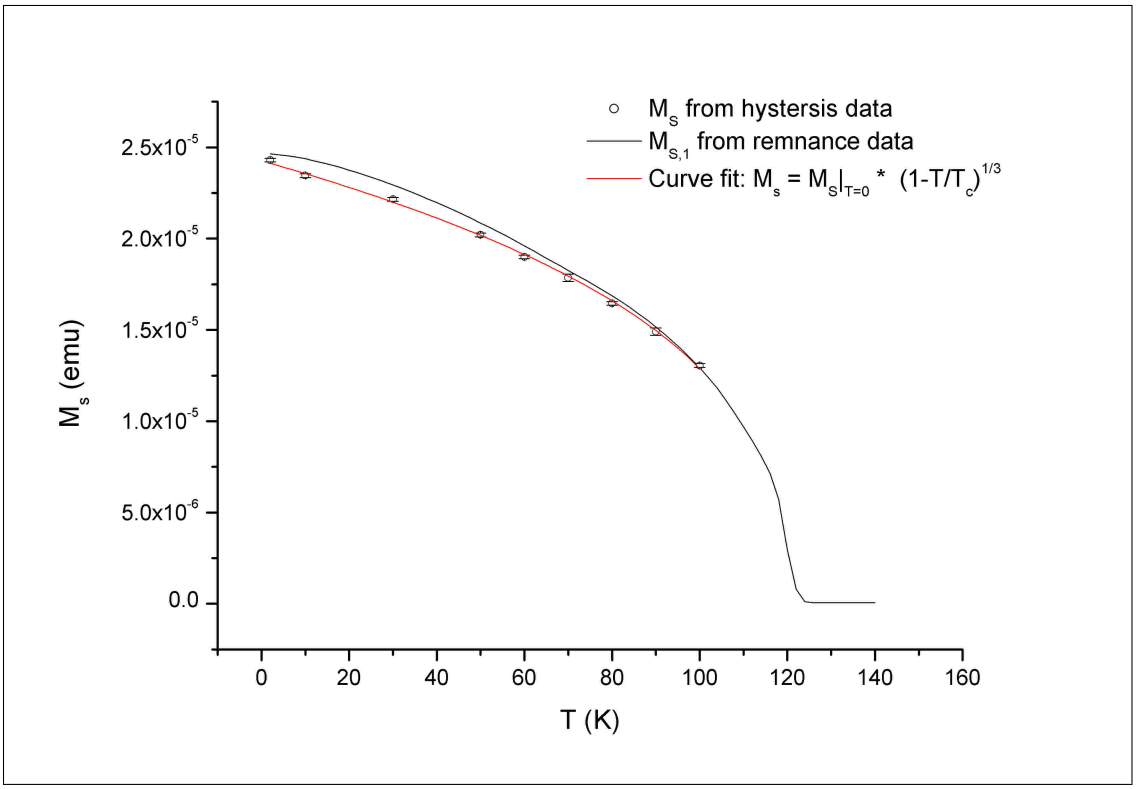

Fig. 3.32 — Net magnetization as a function of temperature for the control sample for the 750nm-grating sample set. Black line: $M_{S,1}$ calculated from remanence data. Open circles: saturation values from hysteresis measurements. Red curve: curve fit to the open circles using equation 3.15.

of temperature on figure 3.34 (the 2K fits are shown in figure 3.33). The uniaxial term is smoothly-varying and monotonic. The cubic term is non-monotonic but a similar functional form has been seen in other samples (see for example chapter 4). The uniaxial term is dominant up to around 60K, from which point the cubic term is stronger; this is consistent with the remanence data and our picture of the easy axes being like a pair of opening scissors (see figure 3.20). Between 100K and T_C (∼120K) we expect the uniaxial term to become negative as the easy axis closes on the [110] direction, but in this temperature range the hard axis is along $[\bar{1}10]$ so we would require hysteresis measurements along $[\bar{1}10]$ to verify this.

At 2K, K_U and K_C are approximately eight times and five times stronger than the shape anisotropy quoted in section 3.6.1 respectively; at 100K they are ∼2.5 and 5 times stronger respectively.

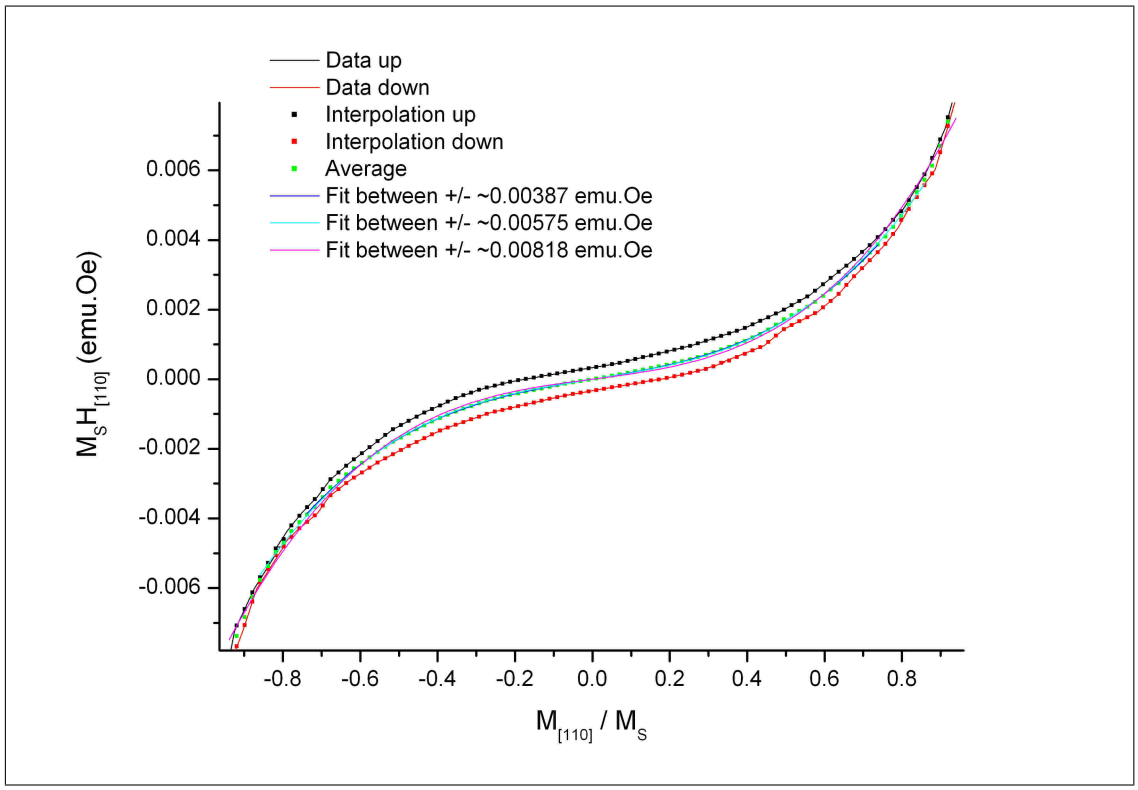

Fig. 3.33 — Hysteresis data at 2K for the control sample from the 750nm-set, along with curve fits using equation 3.12 over various ranges.

More useful than plotting the anisotropy constants against temperature is deter-

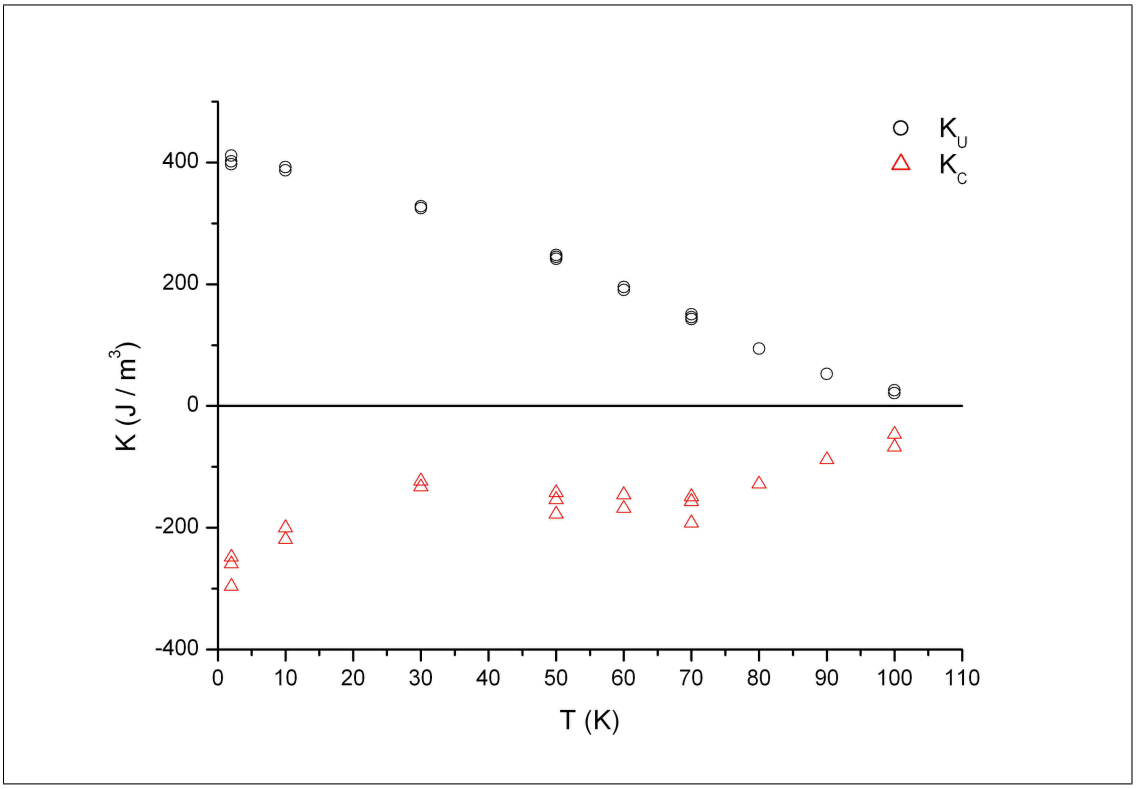

Fig. 3.34 — Cubic (K_C) and uniaxial (K_U) anisotropy coefficients against temperature for the control sample from the 750nm-grating set, extracted from hard-axis hysteresis measurements.

mining their relationship with respect to the net magnetization. For this purpose K_U and K_C were plotted against M_S, ${M_S}^2$ and ${M_S}^4$ and $\log(K_U)$ and $\log(K_C)$ against $\log(M_S)$. The plot of $\log(K_U)$ and $\log(K_C)$ versus $\log(M_S)$ is shown in figure 3.35. I am using as M_S the smoothed magnetization obtained from curve fit described above (figure 3.32) — the same as was used in the extraction of the coefficients from the data. It is clear that neither $K_U(M_S)$ nor $K_C(M_S)$ follow any single power-law relationship, although K_U is smoothly-varying and monotonic.

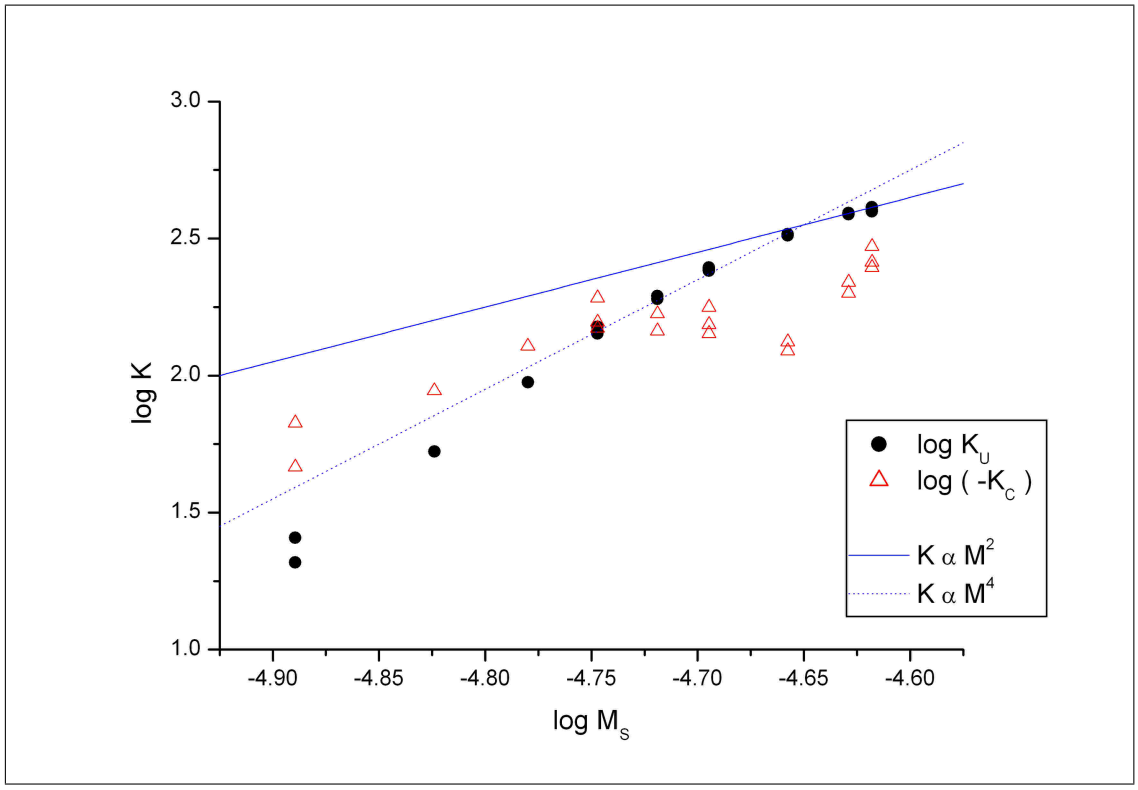

Fig. 3.35 — The uniaxial and cubic anisotropy coefficients, K_U and K_C, against the net magnetization, M_S, on a log-log scale, for the control sample from the 750nm-grating set. M_S is the smoothed magnetization from figure 3.32, the same magnetization used in fitting the hard-axis hysteresis loops. $K \propto {M_S}^2$ and $K \propto {M_S}^4$ are shown for comparison.

[$\bar{1}$10] sample analysis

The analysis for the sample with stripes along [$\bar{1}$10] followed very much the same procedure as the analysis of the control sample so, as previously, the first step was

to extract the saturation magnetization as a function of temperature. The saturation magnetization from the hysteresis loops was this time averaged between 2000 Oe $< |H| <$ 3000 Oe; these are plotted on figure 3.36 together with the net magnetization $M_{S,1}$ from the remanence data. Immediately it can be seen that the control sample gave better results in this respect (figure 3.32), in that for the control sample the data points from hysteresis measurements are monotonic and smoothly-varying within error, and those points lie much closer to the net magnetization curve from the remanence data. Nevertheless equation 3.15 was fitted to the hystereis datapoints twice to smooth the data, once for all data points and once with 'bad' data points omitted (10K, 90K and 100K); these give the black and red curves respectively. For the black curve the fitting gives $T_C = 126.5$K and $M_S|_{T=0} = 9.58 \times 10^{-6}$ emu, whereas for the red curve $T_C = 108.6$K and $M_S|_{T=0} = 9.55 \times 10^{-6}$ emu. Although T_C for the black curve is closer to that from remanence data, I use the red curve as the saturation magnetization when fitting equation 3.12 to the hard-axis loops to obtain K_U and K_C. As stated previously the mean field approximation breaks down close to T_C, so it is not necessary to pick the curve with the best match to T_C.

At each temperature equation 3.12 was fitted to the corresponding hysteresis loop to provide K_C and K_U. As before, fitting was performed over various ranges of H but $2(K_U - K_C)/M_S$ was reasonably consistent, allowing us to select K_U and K_C from the valid fits. These are shown against temperature in figure 3.37. $K_C(T)$ looks very similar to $K_C(T)$ for the control sample, both in terms of magnitude and functional form. At 2K, 90K and 100K the K_U datapoints look spurious; this is a result of the uncertainty in M_S at these temperatures, discussed above. Otherwise $K_U(T)$ for this sample is similar in shape as for the control sample but is approximately a factor of 2 stronger. Both K_U and K_C are consistently significantly stronger than the shape anisotropy over the whole range of temperatures.

A plot of $\log(K_U)$ and $\log(K_C)$ against $\log(M_S)$ is shown in figure 3.38 (again ${M_S}^2$ and ${M_S}^4$ are shown for comparison). There is no obvious power-law relationship

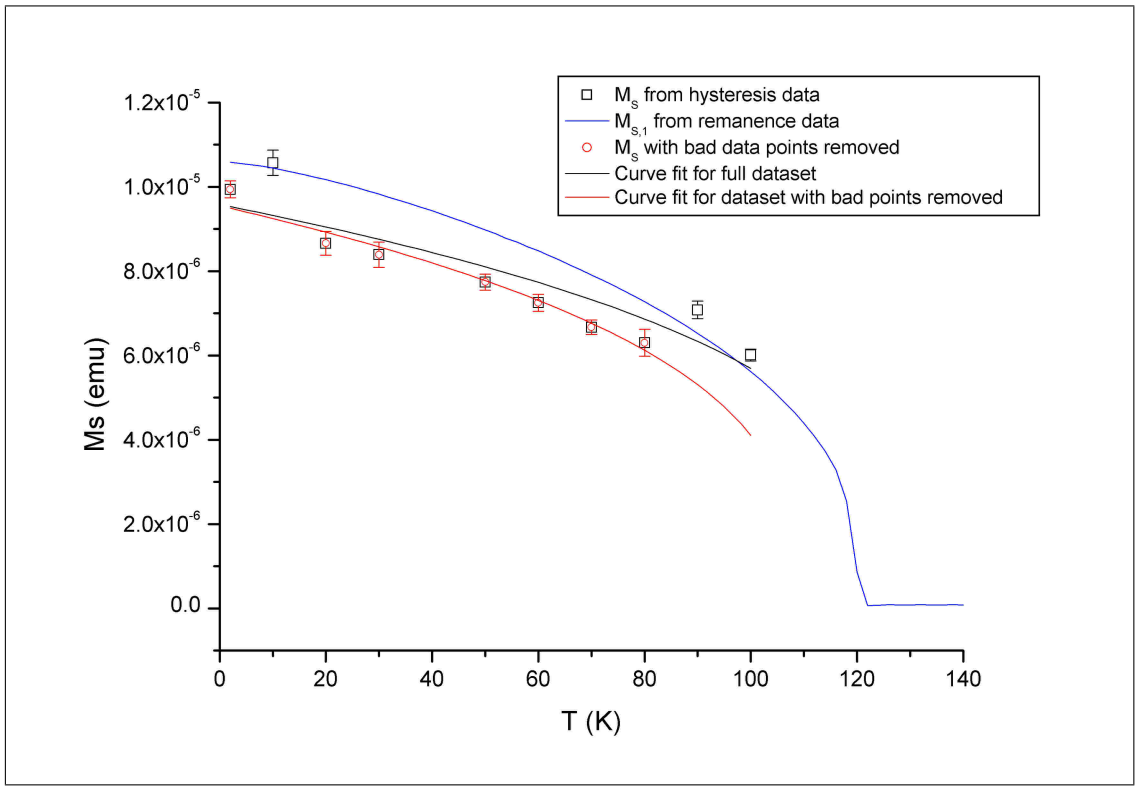

Fig. 3.36 — Net magnetization as a function of temperature for the sample patterned along $[\bar{1}10]$ from the 750nm-grating set. Blue line: $M_{S,1}$ calculated from remanence data. Open symbols: saturation values from hysteresis measurements (black: all T; red: excluding 10K, 90K and 100K). Black curve: curve fit to black symbols using equation 3.15. Red curve: curve fit to red symbols using the same expression.

between K_U or K_C and M_S.

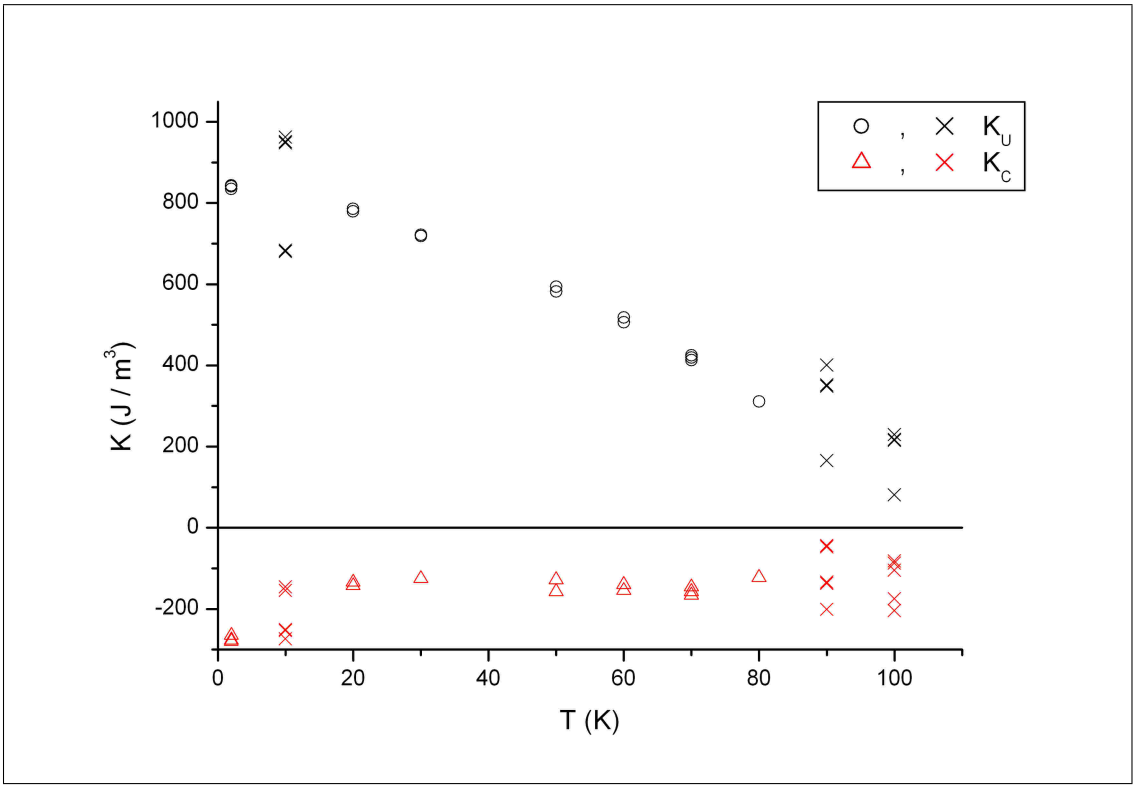

Fig. 3.37 — Cubic (K_C) and uniaxial (K_U) anisotropy coefficients against temperature for the sample with 750nm gratings along $[\bar{1}10]$, extracted from hard-axis hysteresis measurements.

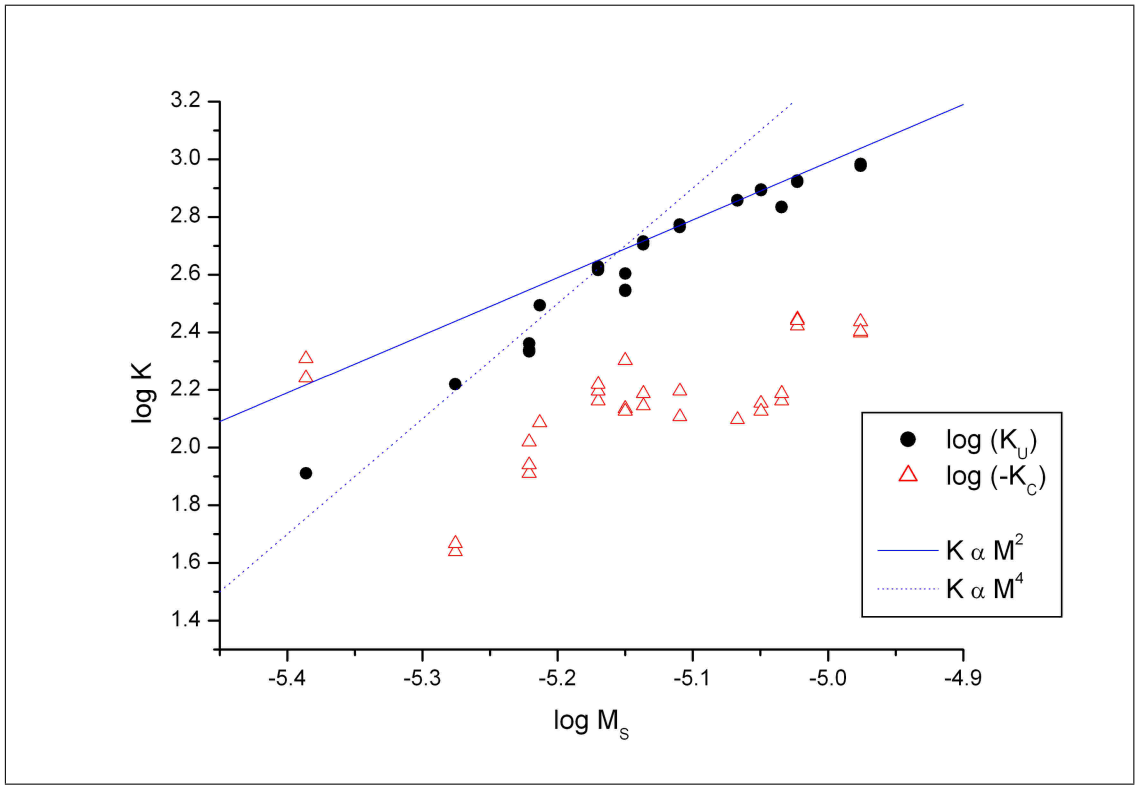

Fig. 3.38 — The uniaxial and cubic anisotropy coefficients, K_U and K_C, against the net magnetization, M_S, on a log-log scale, for the sample with 750nm gratings along $[\bar{1}10]$. M_S is the smoothed magnetization from figure 3.32, the same magnetization used in fitting the hard-axis hysteresis loops. $K \propto {M_S}^2$ and $K \propto {M_S}^4$ are shown for comparison.

[110] sample analysis

Analysing this sample in the same way as for the previous two samples, with the caveat that we must now use equation 3.13 for the fitting instead of 3.12, gave the following results. The saturation magnetization from the hysteresis measurements, averaged between $2000 < |H| < 3000$ Oe, along with the net magnetization $M_{S,1}$ from the remanence data, are shown together in figure 3.39. Also shown are two curve fits to the points extracted from hysteresis data, each with a different T_C. The first curve fit is with the Curie temperature as a free parameter, the second with it fixed at 120K. The latter seems to give the better fit and it is this that is used as the saturation magnetization in the extraction of the anisotropy coefficients.

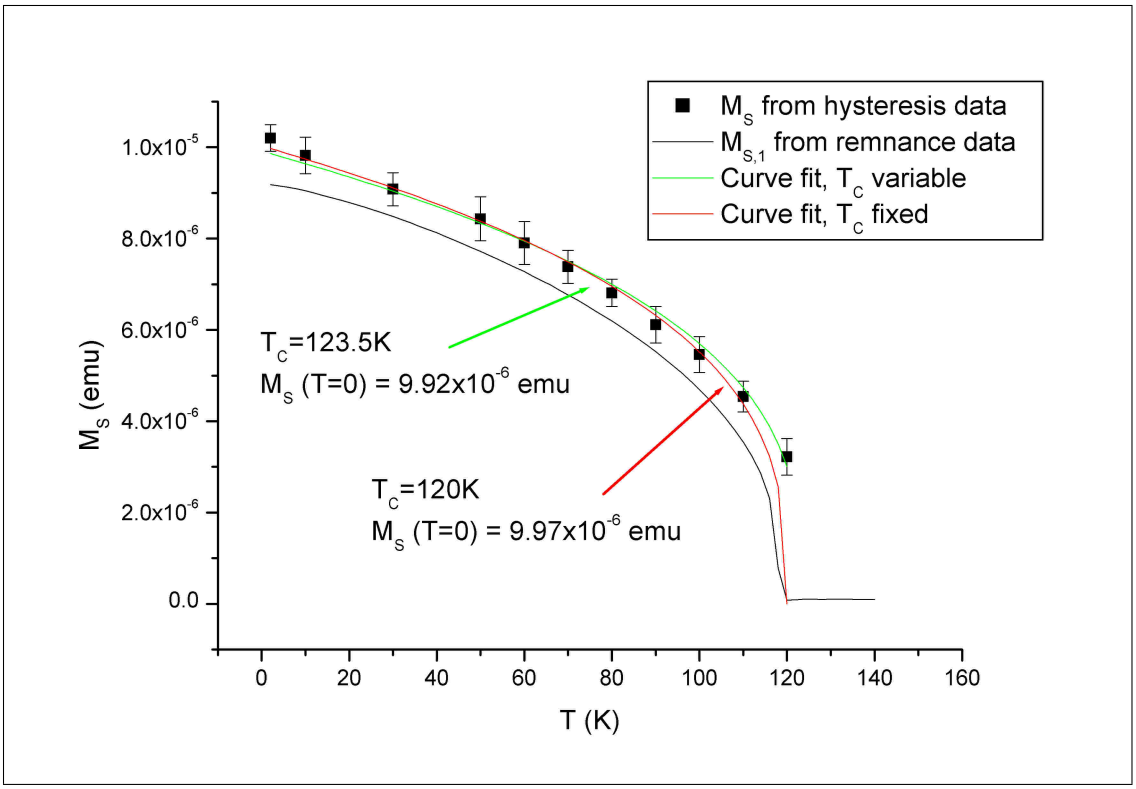

Fig. 3.39 — Net magnetization as a function of temperature for the sample patterned along [110] from the 750nm-grating set. Black line: $M_{S,1}$ calculated from remanence data. Black squares: saturation values from hysteresis measurements. Green curve: the usual curve fit with T_C as free parameter. Red curve: curve fit with T_C fixed at 120K.

K_U and K_C as a function of temperature are shown in figure 3.40. Both appear

to be monotonic, smoothly-varying functions and K_U is negative for this sample as expected from the switching of the easy and hard axes seen in the remanence data. Apart from having the opposite sign, the form of K_U is similar to the other two samples and the magnitude is a little larger than K_U from the control sample. K_C has a different functional form and a magnitude which is, in places, more than a factor of two larger than the other two samples. This is in part because the rotation of the easy axis for these gratings means that the measurement is some-way off the hard axis at the lower temperatures, with this fitting having been derived for truly hard-axis data.

As we shall see in the remanence simulations, these coefficients explain qualitatively very well most of the features of the remanence data. Once again the shape anisotropy is weaker than the magnetocrystalline anisotropy, being almost an order of magnitude smaller at all temperatures. A plot of $\log(-K_U)$ and $\log(-K_C)$ against $\log(M_S)$ is shown in figure 3.41; again there is no convincing power-law relationship between K_U or K_C and the saturation magnetization.

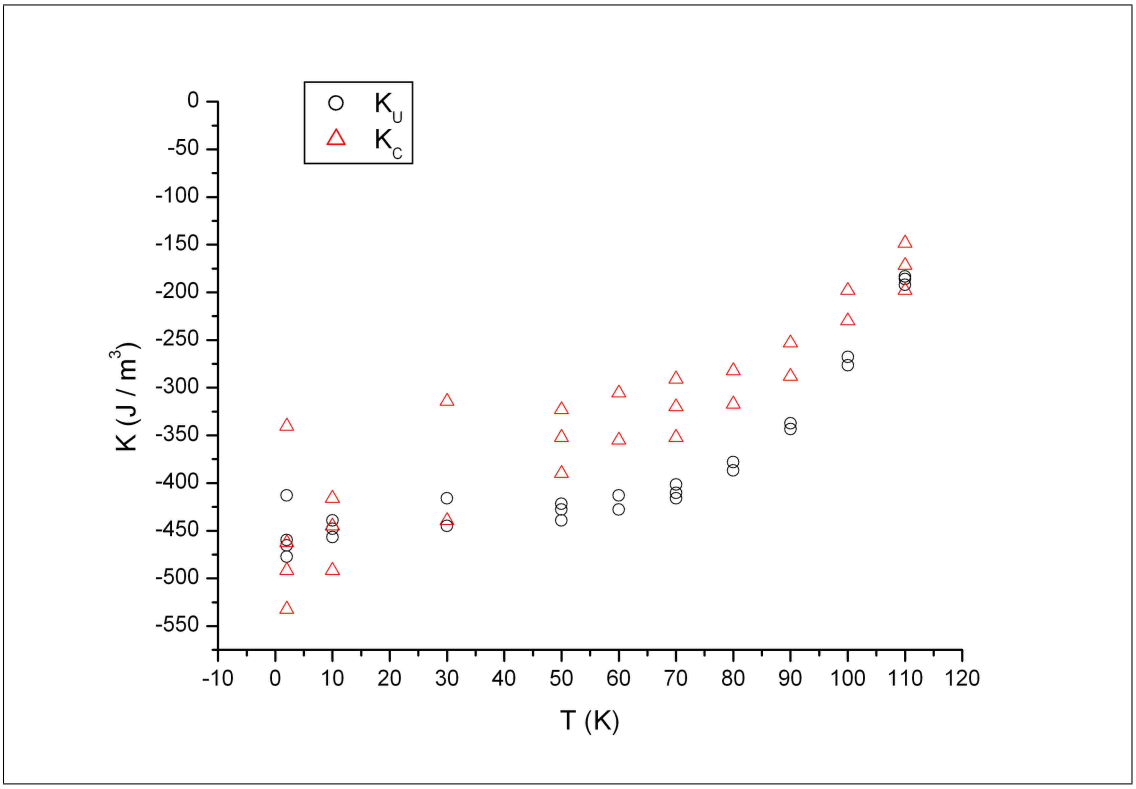

Fig. 3.40 — Cubic (K_C) and uniaxial (K_U) anisotropy coefficients against temperature for the sample with 750nm gratings along [110], extracted from hard-axis hysteresis measurements.

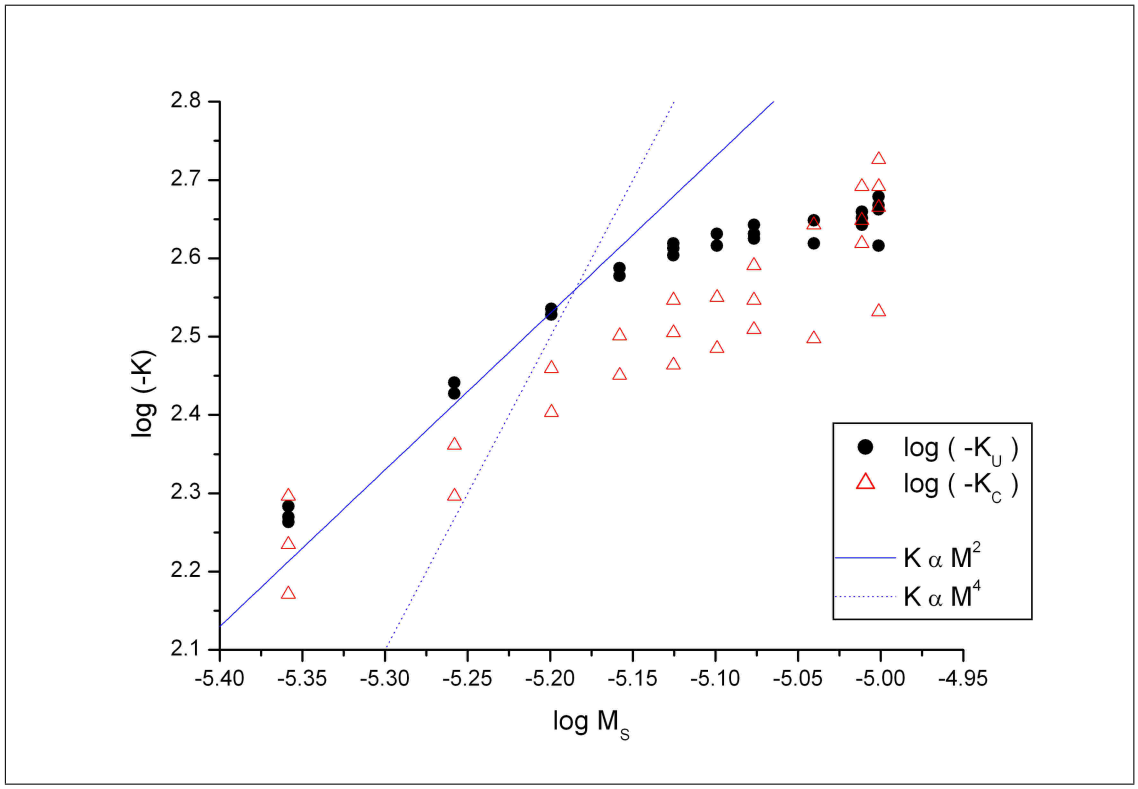

Fig. 3.41 — The cubic and uniaxial anisotropy coefficients, K_C and K_U, against the net magnetization, M_S, on a log-log scale, for the sample with 750nm gratings along [110]. M_S is the smoothed magnetization from figure 3.32, the same magnetization used in fitting the hard-axis hysteresis loops. $K \propto {M_S}^2$ and $K \propto {M_S}^4$ are shown for comparison.

3.6.4 Collated Anisotropy Coefficients

Perhaps the clearest way to show the effects of patterning on the anisotropy coefficients is to show all the anisotropy coefficients from all three samples together on one plot. Figure 3.42 shows K_U and K_C against temperature for all of the samples.

The $[\bar{1}10]$ sample shows almost no modification of the cubic coefficient, within error, as expected. K_C for the [110] sample is quite different from that for the control sample, counter to expectations, but section 3.6.3 has a discussion on this. In general we can conclude that patterning has had no definitive effect on the cubic contribution to the magnetocrystalline anisotropy.

The effects of patterning on the uniaxial coefficients are very clear in figure 3.42. For the sample with stripes along the $[\bar{1}10]$ direction the coefficient is approximately doubled — this is the sample with an overcut etch profile. For the sample with stripes along [110] which has an undercut etch profile the uniaxial term has flipped sign but kept approximately the same magnitude which represents a much stronger effect from the patterning.

Furthermore we can plot ΔK_U versus temperature — figure 3.43 — where ΔK_U is $\left(K_{U,[110]} - K_{U,[\mathrm{ctrl}]}\right)$ or $\left(K_{U,[\bar{1}10]} - K_{U,[\mathrm{ctrl}]}\right)$ for the two patterned samples respectively. This is essentially a direct representation of the dependencies of the anisotropy coefficients on the lithography. The effect of patterning in the [110] direction is around twice as strong as in the $[\bar{1}10]$ direction. The inset, which is a log–log plot of the same information, shows that the functional form of the dependence of K_U on the patterning is the same for each sample.

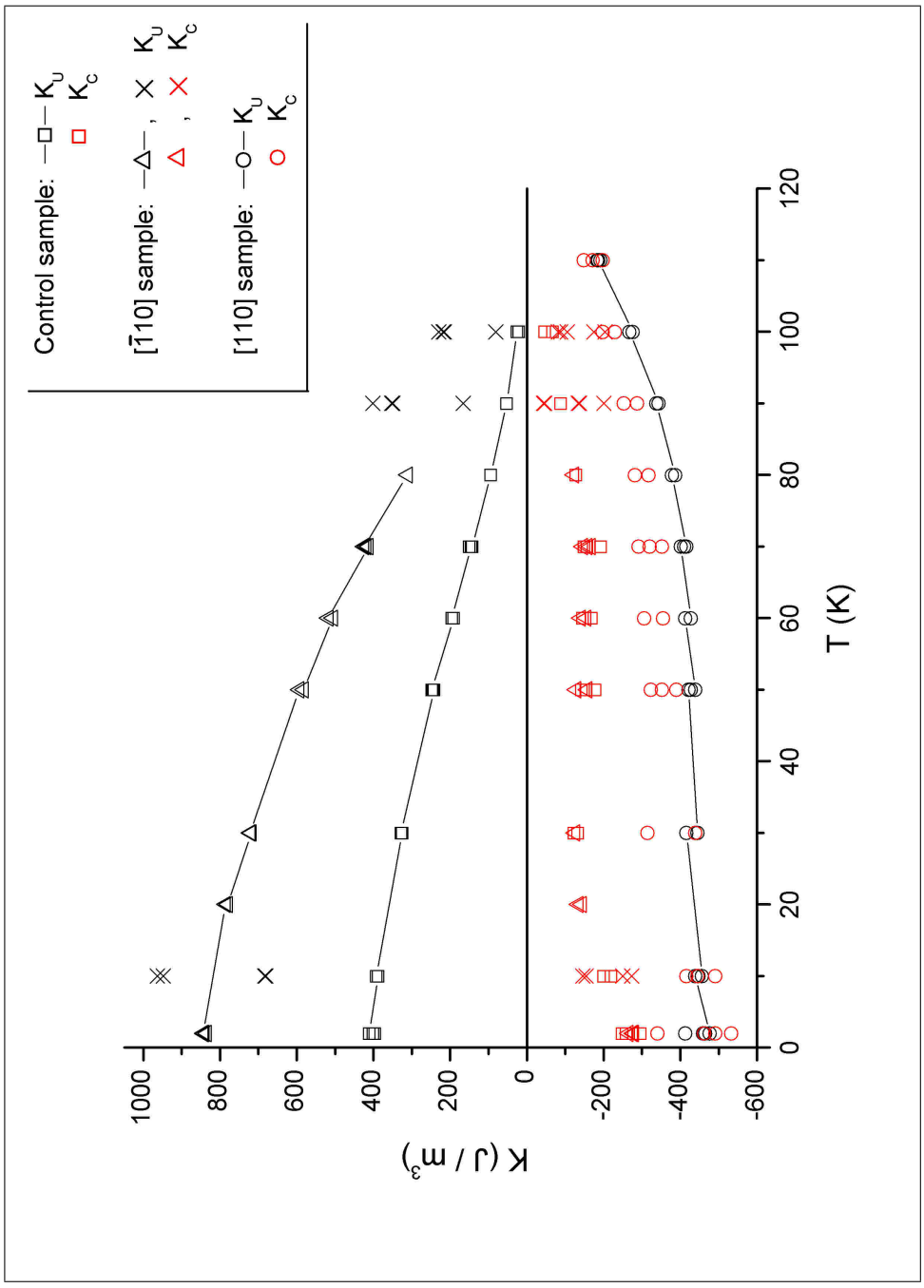

Fig. 3.42 — Cubic and uniaxial coefficients, K_C and K_U, against temperature for all three samples, showing strong modification of the uniaxial coefficients in the patterned samples but relatively small change in the cubic coefficients.

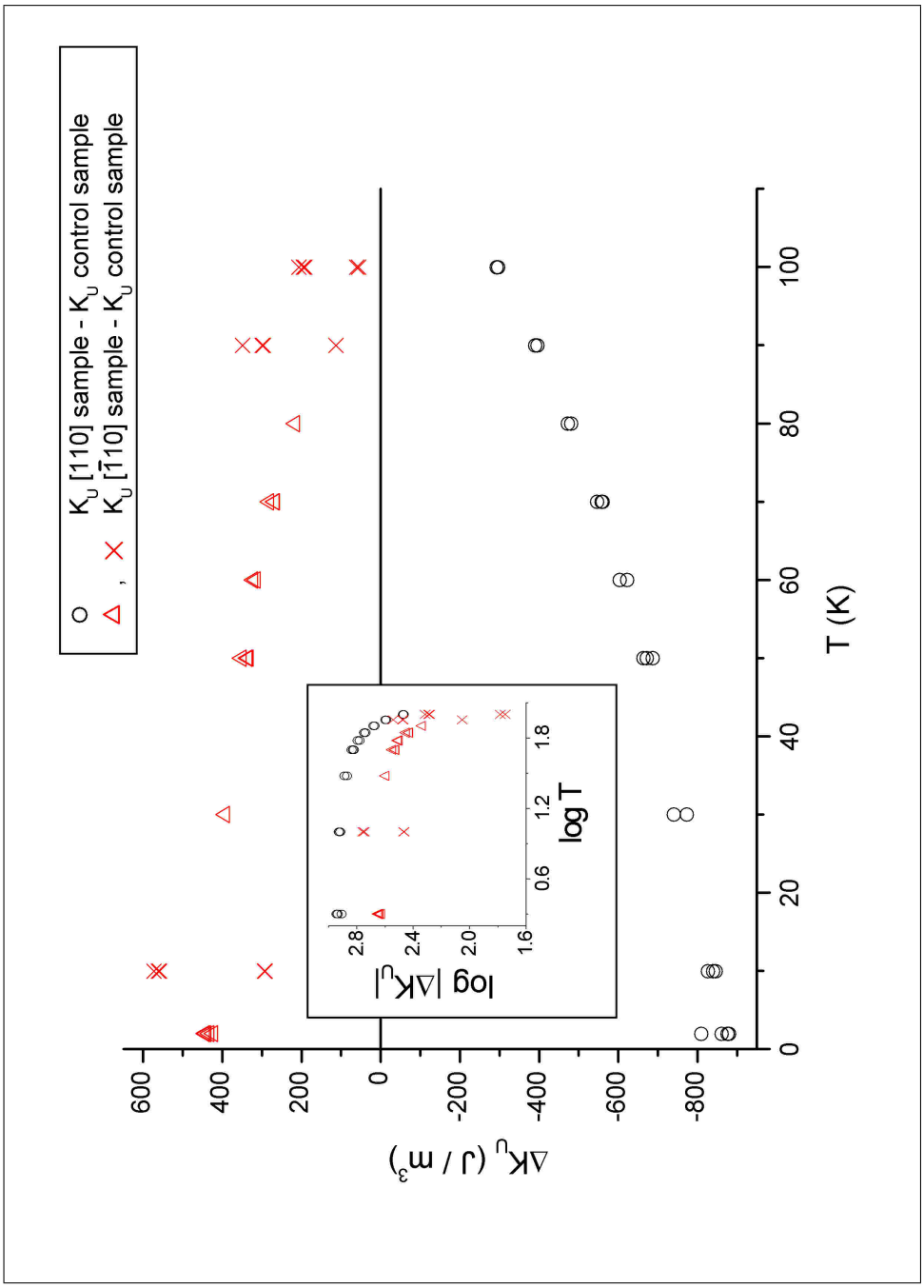

Fig. 3.43 — ΔK_U against temperature for the two patterned samples. This directly shows the dependence of the modification of the uniaxial coefficients on the lithography. Inset: ΔK_U against ΔT, showing that the dependence of the modification of the uniaxial coefficients on the lithography has the same functional form for each of the patterned samples.

3.6.5 Remanent Magnetization Simulations

The simulated remanent magnetizations are shown in figures 3.44, 3.45 and 3.46 for the control sample and the samples patterned along [$\bar{1}$10] and [110] respectively. The control sample simulation shows good agreement with the raw data for $T \leq 60$ K, except that the raw data is non-zero along the hard axis. As discussed previously, this is most likely due to a small misalignment of the sample in the magnetometer during the hard-axis remanence measurement. Above 60 K, K_U and K_C have very similar magnitudes (see figure 3.34) so the simulation is very dependent on small errors in either coefficient, and this is why the accuracy of the simulation is not so good at higher temperatures, particularly along the [110] direction. The large discrepancy between the [100] and [010] simulation and raw data above 60 K has a different cause; the sample splits into domain above ∼60 K whereas the model predicts the single-domain response.

The simulation for the sample with stripes along [$\bar{1}$10] shows remarkable agreement with the raw data. In an initial fit, using just the single-domain model (equation 3.1), the splitting of the [100] and [010] curves was not replicated and nor was the deviation of the hard axis from zero. When a small offset angle δ is incorporated into the K_U term in the model, to account for the 5° misalignment of the stripes with respect to the crystallographic axis, these effects were replicated well.

$$E = K_U \sin^2(\boldsymbol{\theta + \delta}) + \left(\frac{K_C}{4}\right) \sin^2(2\theta) - MH\cos(\gamma - \theta) \tag{3.16}$$

The choice of angle δ is somewhat arbitrary; although it is due to possible misalignment of the sample in the SQUID system the value of δ is not equal the angle of misalignment when expressed in this way. The best simulation results were for $\delta = -3.5°$ which is what is shown in figure 3.45. The fact that the agreement between simulation and raw data is so remarkably good for this sample is simply because K_U is significantly stronger than K_C at all temperatures (see figure 3.37), so any small

errors in the coefficients are inconsequential. In effect, although the simulation looks very good, it doesn't necessarily confirm that I have extracted K_U and K_C accurately, just that I was correct to find $|K_U| > |K_C|$ at all T.

For the sample patterned along [110] equation 3.16 was once again used for the simulation; this time the best fit was for $\delta = -2°$. The fit is reasonably good at all temperatures, replicating all the main features except for the convergence of the [100] and [010] traces above ∼100 K; however, because K_U and K_C have a similar magnitude, particularly at the lower temperatures (figure 3.40), the remanence is strongly dependent on variations in K_U and K_C. The scatter of the simulation datapoints is because of the large scatter in the extracted coefficients at each temperature (see figure 3.40).

In general the simulations show that all the main features seen in the data can be explained by the single-domain model with good agreement between the real data and simulated response indicating that the extracted anisotropy coefficients can at the very least be described as very plausible.

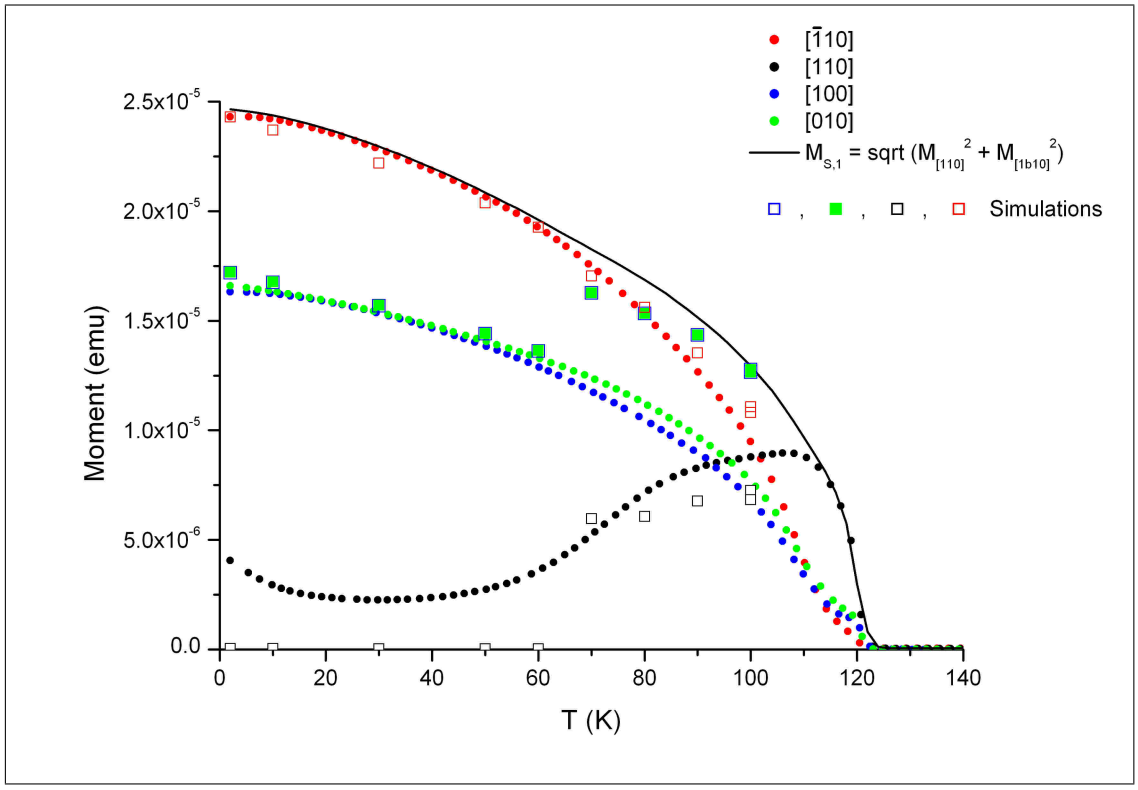

Fig. 3.44 — Remnant magnetization simulations for the control sample from the 750 nm-grating set, using the coefficients K_U and K_C extracted from hard-axis hysteresis loops.

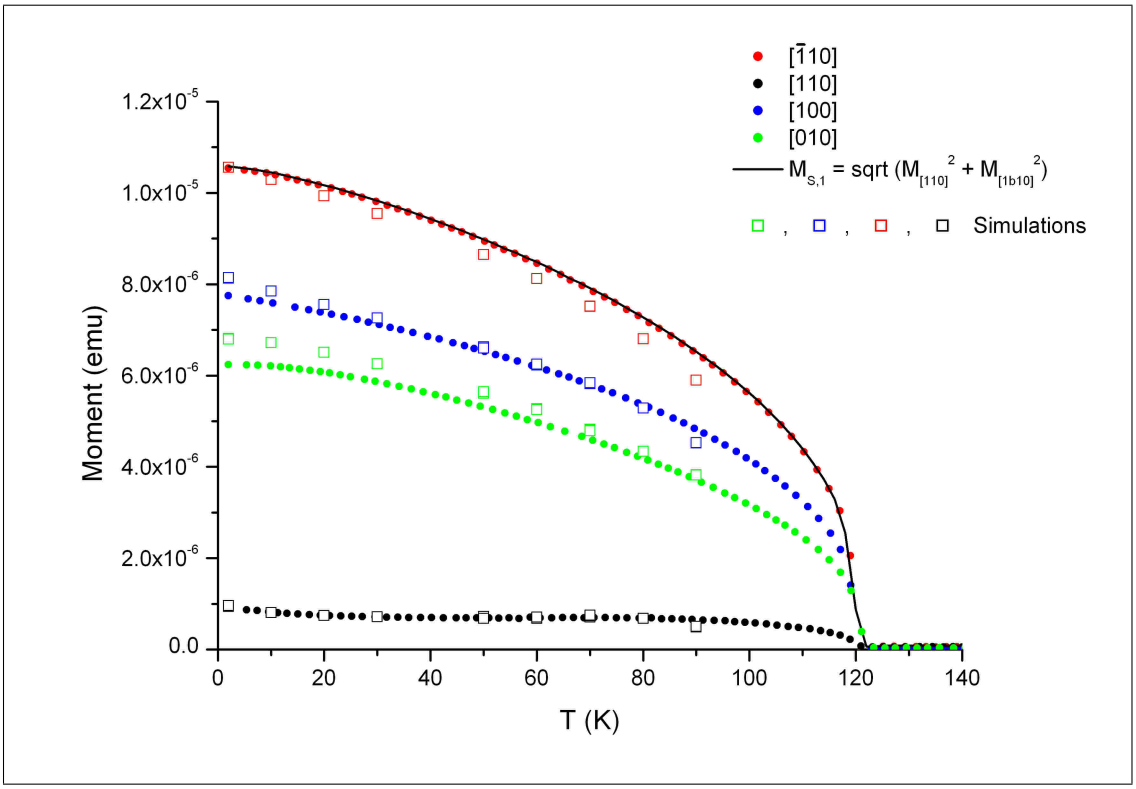

Fig. 3.45 — Remnant magnetization simulations for the sample with 750 nm gratings along [$\bar{1}$10], using the coefficients K_U and K_C extracted from hard-axis hysteresis loops. A small misalignment of K_U was added into the model to replicate the misalignment of the stripes with respect to the crystallographic axis — see text.

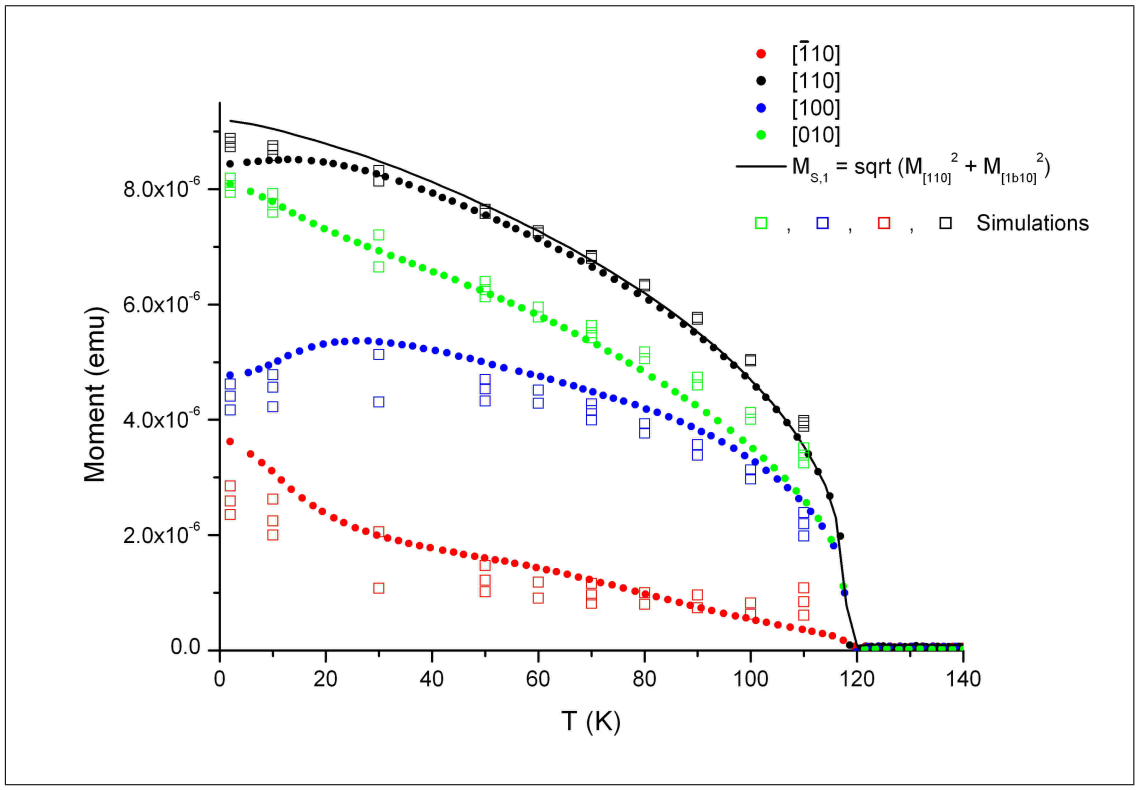

Fig. 3.46 — Remnant magnetization simulations for the sample with 750 nm gratings along [110], using the coefficients K_U and K_C extracted from hard-axis hysteresis loops. A small misalignment of K_U was added into the model to replicate the misalignment of the stripes with respect to the crystallographic axis — see text. The scatter in simulations datapoints is a result of the scatter in the extracted K_U and K_C (see figure 3.40).

3.7 Summary

In this chapter I have presented the results of patterning (Ga,Mn)As thin films into 1µm-wide and 750nm-wide stripes along the [110] and [$\bar{1}$10] in-plane crystallographic axes. From remanence data we can interpret and compare the magnetic anisotropy of the parent wafers and the patterned samples whereas hard-axis hysteresis measurements allow us to extract the cubic and uniaxial anisotropy coefficients, K_C and K_U, quantitatively. The results clearly demonstrate that patterning narrow stripes can strongly influence the magnetic anisotropy of (Ga,Mn)As thin films.

For the wider stripes the magnetic anisotropy was complicated and we were unable to describe the behaviour of the parent wafer completely, making quantitative analysis futile. However, from the remanence data we were able to see qualitatively that the effects of patterning were striking, despite these samples having wider stripes than designed. In the un-patterned sample the [$\bar{1}$10] axis was easier than the [110] axis at all temperatures and was the overall easy axis for most of the temperature range (the sample was cubic along [100] and [010] below ∼20K). The sample patterned along the [$\bar{1}$10] direction had this axis as the dominant easy axis at *all* temperatures, whereas for the sample patterned along [110], [110] was easier or equivalent to [$\bar{1}$10] at all temperatures, albeit weaker than [100] and [010] below ∼50K.

The 750nm-wide stripes exhibited a simpler magnetic anisotropy in the parent wafer and it was possible to extract the anisotropy coefficients quantitatively for these samples. The uniaxial anisotropy was strongly modified by patterning, with the stripes along the [110] direction having an effect approximately twice as strong as the stripes along [$\bar{1}$10]. This is attributed to anisotropic etch profiles which in turn was caused by wet-etching the patterned samples. The mechanism responsible for the modification of the anisotropy is believed to be strain relaxation across the widths of the stripes, and finite elements simulations confirm that the strain relaxation is significantly stronger in undercut samples than overcut.

This study also shows cubic and uniaxial coefficients which do not follow the $K_U \propto {M_S}^2$ and $K_C \propto {M_S}^4$ dependencies which have been quoted elsewhere. K_C has an unusual functional form but a similar form is seen in the following chapter, based on data taken from an entirely different wafer.

The most striking result from the chapter is that by allowing local relaxation of the incorporated growth strain we can rotate the magnetic easy axis by 90°, switching the easy and hard axis directions of the parent wafer.

References

[1] M. Tanaka and Y. Higo, "Large Tunneling Magnetoresistance in GaMnAs/AlAs/GaMnAs Ferromagnetic Semiconductor Tunnel Junctions," *Physical Review Letters*, vol. 87, no. 2, pp. 026602/1–4, 2001.

[2] C. Gould, C. Rüster, T. Jungwirth, E. Girgis, G. M. Schott, R. Giraud, K. Brunner, G. Schmidt, and L. W. Molenkamp, "Tunneling Anisotropic Magnetoresistance: A spin-valve like tunnel magnetoresistance using a single magnetic layer," *Physical Review Letters*, vol. 93, no. 11, pp. 117203/1–4, 2004.

[3] A. D. Giddings, M. N. Khalid, J. Wunderlich, S. Yasin, R. P. Campion, K. W. Edmonds, J. Sinova, T. Jungwirth, K. Ito, K.-Y. Wang, D. Williams, B. L. Gallagher, and C. T. Foxon, "Large Tunneling Anisotropic Magnetoresistance in (Ga,Mn)As nanoconstrictions," *Physical Review Letters*, vol. 94, p. 127202, 2005.

[4] J. Wunderlich, T. Jungwirth, B. Kaestner, A. C. Irvine, A. B. Shick, N. Stone, K.-Y. Wang, U. Rana, A. D. Giddings, C. T. Foxon, R. P. Campion, D. A. Williams, and B. L. Gallagher, "Coulomb Blockade Anisotropic Magnetoresistance Effect in a (Ga, Mn)As Single-Electron Transistor," *Physical Review Letters*, vol. 97, no. 7, pp. 077201–1, 2006.

[5] J. Wunderlich, T. Jungwirth, A. C. Irvine, B. Kaestner, A. B. Shick, R. P. Campion, D. A. Williams, and B. L. Gallagher, "Coulomb blockade anisotropic magnetoresistance and voltage controlled magnetic switching in a ferromagnetic GaMnAs single electron transistor," *Journal of Magnetism and Magnetic Materials*, vol. 310, pp. 1883–1888, 2007.

[6] S. Hümpfner, K. Pappert, J. Wenisch, K. Brunner, C. Gould, G. Schmidt, L. W. Molenkamp, M. Sawicki, and T. Dietl, "Lithographic engineering of anisotropies in (Ga,Mn)As," *Applied Physics Letters*, vol. 90, pp. 102102/1–3, 2007.

[7] K.-Y. Wang, M. Sawicki, K. W. Edmonds, R. P. Campion, S. Maat, C. T. Foxon, B. L. Gallagher, and T. Dietl, "Spin Reorientation Transition in Single-Domain (Ga, Mn)As ," *Physical Review Letters*, vol. 95, p. 217204, 2005.

[8] M. Sawicki, K.-Y. Wang, K. W. Edmonds, R. P. Campion, C. R. Staddon, N. R. S. Farley, C. T. Foxon, E. Papis, E. Kaminska, A. Piotrowska, T. Dietl, and B. L. Gallagher, "In-plane uniaxial anisotropy rotations in (Ga,Mn)As thin films," *Physical Review B*, vol. 71, no. 12, 2005.

[9] K. Hamaya, R. Moriya, A. Oiwa, T. Taniyama, Y. Kitamoto, and H. Munekata, "Control of Magnetic Anisotropy and Magnetotransport in Epitaxial Micropatterned (Ga,Mn)As Wire Structures," *IEEE Transactions on Magnetics*, vol. 39, no. 5, pp. 2785–2787, 2003.

[10] K. Hamaya, R. Moriya, A. Oiwa, T. Taniyama, Y. Kitamoto, Y. Yamazaki, and H. Munekata, "Contribution of Shape Anisotropy to the Magnetic Configuration of (Ga,Mn)As," *Japanese Journal of Applied Physics*, vol. 43, no. 2B, pp. L306–L308, 2004.

[11] K. Hamaya, T. Taniyama, T. Koike, and Y. Yamazaki, "Effects of the shape anisotropy on the magnetic configuration of (Ga,Mn)As and its evolution with temperature," *Journal of Applied Physics*, vol. 99, pp. 123901/1–3, 2006.

[12] J. Wenisch, C. Gould, L. Ebel, J. Storz, K. Pappert, M. J. Schmidt, C. Kumpf, G. Schmidt, K. Brunner, and L. W. Molenkamp, "Control of Magnetic Anisotropy in (Ga,Mn)As by Lithographically-Induced Strain Relaxation," *Physical Review Letters*, vol. 99, p. 077201, 2007.

[13] A. W. Rushforth, K. Výborný, C. S. King, K. W. Edmonds, R. P. Campion, C. T. Foxon, J. Wunderlich, A. C. Irvine, P. Vašek, V. Novák, K. Olejník, J. Sinova, T. Jungwirth, and B. L. Gallagher, "Anisotropic Magnetoresistance Components in (Ga,Mn)As," *Physical Review Letters*, vol. 99, p. 147207, 2007.

[14] J. Wunderlich, A. C. Irvine, J. Zemen, V. Holý, A. W. Rushforth, E. D. Ranieri, U. Rana, K. Výborný, J. Sinova, C. T. Foxon, R. P. Campion, D. A. Williams, B. L. Gallagher, and T. Jungwirth, "Local control of magnetocrystalline anisotropy in (Ga,Mn)As microdevices: Demonstration in current-induced switching," *Physical Review B*, vol. 76, p. 054424, 2007.

[15] A. Aharoni, "Demagnetizing factors for rectangular ferromagnetic prisms," *Journal of Applied Physics*, vol. 83, no. 6, pp. 3432–3434, 1998.

[16] K. Pappert, S. Hümpfner, C. Gould, J. Wenisch, K. Brunner, G. Schmidt, and L. Molenkamp, "Exploiting Locally Imposed Anisotropies in (Ga,Mn)As: a Nonvolatile Memory Device," *Nature Physics*, vol. 3, no. 8, pp. 573–578, 2007.

[17] A. W. Rushforth, E. D. Ranieri, J. Zemen, J. Wunderlich, K. W. Edmonds, C. S. King, E. Ahmad, R. P. Campion, C. T. Foxon, B. L. Gallagher, K. Výborný, J. Kučera, and T. Jungwirth, "Voltage control of magnetocrystalline anisotropy

in ferromagnetic-semiconductor-piezoelectric hybrid structures," *Physical Review B (Condensed Matter and Materials Physics)*, vol. 78, no. 8, p. 085314, 2008.

[18] H. B. Callen and E. Callen, "The Present Status of the Temperature Dependence of Magnetocrystalline Anisotropy, and the $l(l+1)/2$ Power Law," *Journal of Physics and Chemistry of Solids*, vol. 27, pp. 1271–1285, 1966.

[19] J. B. Staunton, S. Ostanin, S. S. A. Razee, B. L. Gyorffy, L. Szunyogh, B. Ginatempo, and E. Bruno, "Temperature Dependent Magnetic Anisotropy in Metallic Magnets from an *Ab Initio* Electronic Structure Theory: $L1_0$-Ordered FePt ," *Physical Review Letters*, vol. 93, p. 257204, 2004.

[20] S. Adachi and K. Oe, "Chemical Etching Chracteristics of (001)GaAs," *Journal of the Electrochemical Society*, vol. 130, no. 12, pp. 2427–2435, 1983.

Chapter 4

A.C. Susceptibility Measurements by an Anisotropic Magnetoresistance Method

4.1 Introduction and Background Theory

4.1.1 Spin Reorientation Transition

As discussed previously in this Thesis, many (Ga,Mn)As samples exhibit a crossover in their magnetocrystalline anisotropy, from cubically-dominated at low temperature to uniaxial at higher temperatures. For such samples there is a temperature at which the cubic and uniaxial terms in the single-domain model (equation 3.1 in chapter 3) are equal, $|K_C| = |K_U|$, and the energy landscape $E(\theta)$ flattens completely over a range of angles (θ is the angle between the magnetization and the $[\bar{1}10]$ direction, as defined in chapter 3). This is illustrated in figure 4.1 which shows the energy landscapes for the cases of $|K_U| < |K_C|$, $|K_U| > |K_C|$ and $|K_U| = |K_C|$.

At the crossover temperature the magnetic moments, lying in the flattened energy minimum, can be reorientated extremely easily by a perturbing field that has a com-

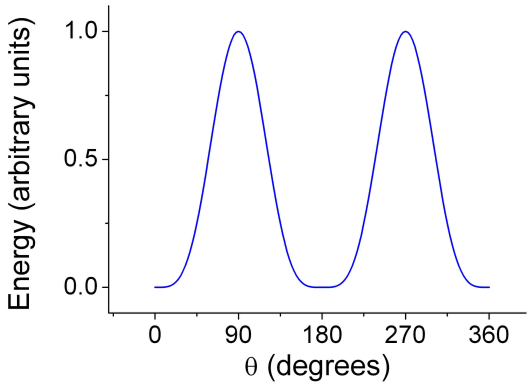

(a) $|K_U| = |K_C|$

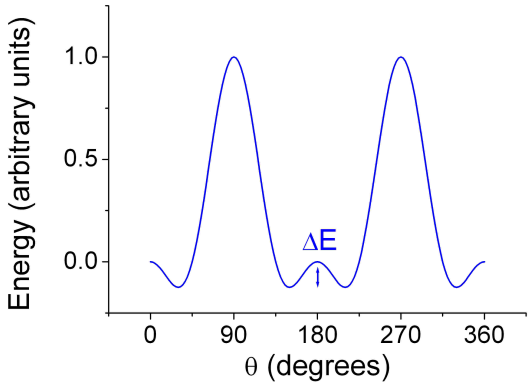

(b) $|K_C| = 2|K_U|$

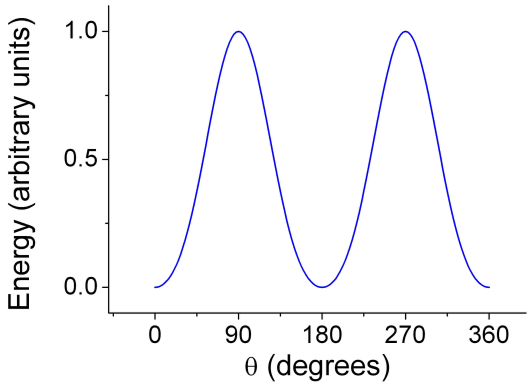

(c) $|K_U| = 2|K_C|$

Fig. 4.1 — Energy from the single domain model (equation 3.1 in chapter 3) as a function of θ and with $H = 0$, for the cases of $|K_U| = |K_C|$, K_U bigger than K_C and K_C bigger than K_U. θ is the angle between the magnetization and crystallographic axes with zero degrees being along $[\bar{1}10]$.

ponent perpendicular to the magnetization. The point at which this occurs is known as the *Spin Reorientation Transition (SRT)* [1]. The SRT creates a peak in measurements of magnetic susceptibility against temperature, measurements which have traditionally been performed by SQUID magnetometry. In this chapter I present a far simpler measurement technique, still based on the magnetic susceptibility, to identify the SRT in the temperature domain.

4.1.2 A.C. Susceptibility

It has been established in earlier chapters that a useful thing to measure in the characterization of magnetic samples is how the magnetization depends on an applied field. D.C. $M(H)$ curves are generated by slowly varying an external magnetic field and measuring the resulting magnetization. This gives us the familiar hysteresis loops seen in chapter 3. The gradient of such $M(H)$ curves, dM/dH, is called the *magnetic susceptibility* and is given the symbol χ.

Of particular interest is how the susceptibility varies in an oscillating external field — the *A.C. susceptibility*. Let us consider a sinusoidal driving field with zero D.C. offset, $H = H_0 \sin(\omega t)$. In the low-frequency regime the magnetization follows the D.C. $M(H)$ curve with no phase shift and, so long as the amplitude is small, the magnetization is proportional to the external field:

$$M(t) \propto H_0 \sin(\omega t) \tag{4.1}$$

The constant of proportionality is the gradient dM/dH i.e. the susceptibility. If the D.C. offset of the field is non-zero, or the magnetization is non-zero at zero external field due to hysteresis, we must add in an offset term Δ. Furthermore, as the frequency is increased phase lags can occur between the applied field and the magnetization due to dynamic effects in the sample. More generally for small amplitudes, therefore, we

should write:

$$M = \chi H_0 \sin(\omega t + \lambda) + \Delta \tag{4.2}$$

This can be expanded into a component in phase with the external field and a component out of phase, as follows:

$$\begin{aligned} M &= \chi H_0 \left[\sin(\omega t)\sin\lambda + \cos(\omega t)\cos\lambda\right] + \Delta \\ &= \chi' H_0 \cos(\omega t) + \chi'' H_0 \sin(\omega t) + \Delta \end{aligned} \tag{4.3}$$

where

$$\begin{aligned} \chi' &= \chi\cos\lambda \qquad \text{and} \\ \chi'' &= \chi\sin\lambda \end{aligned} \tag{4.4}$$

so

$$\lambda = \arctan(\chi''/\chi')$$

So here we have an in-phase component of the susceptibility, χ' (often referred to as the *real* part of the susceptibility), and an out-of-phase component, χ'' (often referred to as the *imaginary* part), which can be measured independently in A.C. susceptibility measurements. The phase shift and hence the out-of-phase component are due to dissipative processes in the sample — in ferromagnetic samples this can be caused by irreversible domain wall movement, whereas in conducting samples it can be caused by eddy currents (in the low frequency limit, where dissipative process are negligible, $\chi' = \chi = (dM/dH)$). Typical measurements are of the complex susceptibility against temperature, frequency, amplitude and D.C. offset. Of particular

interest in this chapter is that the in- and out-of-phase components are both sensitive to thermodynamic phase changes. In measurements of χ against temperature, the magnetic susceptibility along particular directions becomes very large at the SRT, the point at which the magnetization can undergo large rotations for relatively small oscillations of the external field. It is this peak in $\chi(T)$ at the SRT which is the subject of this chapter.

4.1.3 The Peak in the A.C. Susceptibility at the SRT

An A.C. external magnetic field that lies at an angle to the easy axis causes the magnetization to oscillate, with the largest response of the magnetization being when the field is perpendicular. Far from the SRT the strength of the anisotropy energies, K_C below the SRT and K_U above, keep the energy minima deep and any oscillations small. However, in the vicinity of the SRT the flattening of the energy landscape allows larger oscillations of the magnetization. In order to understand fully the effects of this flattening we must consider the modification to the energy landscape caused by the external field — the $MH_0\cos(\gamma-\theta)$ term in the single-domain model. Below the SRT, $E(\theta)$ is characterized by a double-minimum separated by a small energy barrier ΔE (figure 4.1(b)). Here the presence of an external field causes the minima to become asymmetrical and as the barrier reduces with increasing temperature there comes a point when ΔE is approximately equal to MH_0, allowing the magnetization to be tipped back and forth from one minimum to the other, symmetrical about $[\bar{1}10]$, as the external field alternates direction. This is illustrated in figure 4.2. Thermal fluctuations will also have a small influence on the onset, tending to increase the susceptibility before $\Delta E = MH_0$. The point at which ΔE is equal to MH_0 necessarily occurs before $K_U = K_C$; therefore we can expect to see an increase in the real part of the susceptibility below the point where the anisotropy coefficients cross over. As the temperature is increased and the system passes through the SRT the double-minimum becomes one and the magnetization oscillates within that single energy

minimum. The minimum quickly deepens as the relative strength of the K_U term increases with increasing temperature, causing the oscillations to drop off quickly. In terms of the real part of the susceptibility, we expect to see a peak in the vicinity of the SRT which begins at a point in temperature below the crossover of the anisotropy coefficients and drops to zero soon after. The imaginary part of the susceptibility is simpler — since this component arises only from dissipative processes we expect no signal until $\Delta E = MH_0$ at which point we expect to see a sharp rise, followed by dropping to zero right at the SRT.

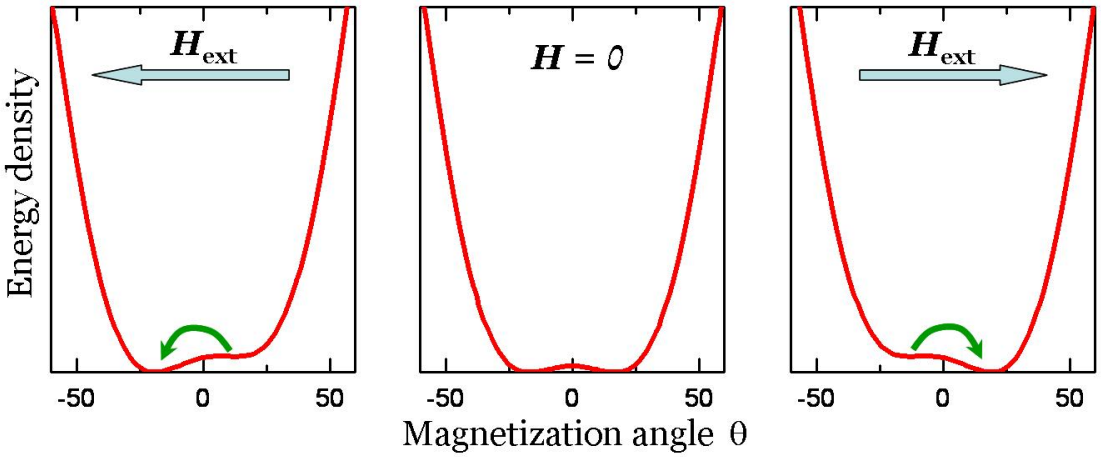

Fig. 4.2 — Below the SRT where the anisotropy is biaxial and characterized by a double-minimum, an external field that has a component perpendicular to the magnetization causes an asymmetry in the energy density; if the field is oscillating this can allow the magnetization to tip back and forth between minima. Figure courtesy of Dr. Kevin Edmonds.

A study of the SRT in 50 nm (Ga,Mn)As films by standard SQUID magnetometry has previously been reported [1]. The calculations in that study, reproduced in figure 4.3, show the expected forms of the in-phase and out-of-phase components of the susceptibility that I have described above and the same qualitative features were seen in their A.C. SQUID measurements (also in figure 4.3). In this study we aim to qualitatively reproduce the features of the complex SRT described. Wang *et. al.* saw the crossover of the cubic and uniaxial anisotropy coefficients at exactly 30 K

with the peak in the imaginary part of the susceptibility occurring at between 20 and 23 K, a difference of approximately 25%. It should be noted that the labels of the crystallographic axes in figure 4 within reference [1] are wrong, whilst the description in the text is correct.

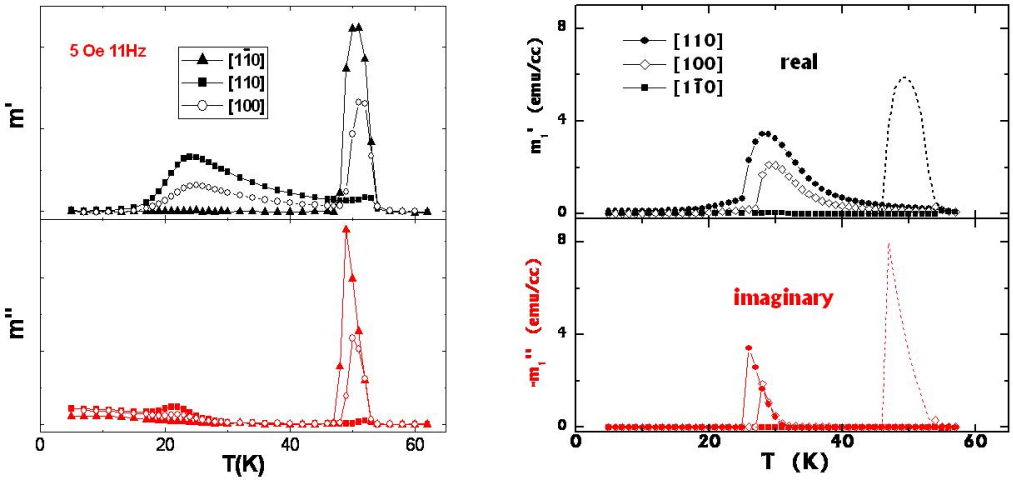

Fig. 4.3 — Measured (left) and calculated (right) responses of the real and imaginary parts of the magnetic susceptibility of a 50 nm (Ga,Mn)As film to a 5 Oe external field oscillating at 11 Hz. Figure courtesy of Dr. Kevin Edmonds, adapted from reference [1]. The temperature of the crossover of the cubic and uniaxial anisotropy coefficients was 30 K.

In our samples the magnetization rotates from an orientation below the SRT either in between [100] and [$\bar{1}$10] or between [010] and [$\bar{1}$10], to being along the [$\bar{1}$10] axis above the SRT, a rotation of 45° at most. The maximum response, therefore, is for a field along the [110] direction when the magnetization is along the [$\bar{1}$10] axis. For small A.C. fields along the [$\bar{1}$10] direction, that is fields smaller than the coercive field, we expect to see no peak in the SRT whereas along the [100] and [010] directions we would expect a peak, but smaller than that expected along the perpendicular direction.

4.1.4 A.C. SQUID Magnetometry

At its simplest, *magnetometry* is the process of applying an external magnetic field to a sample and measuring the resulting magnetization. In D.C. SQUID magnetometry a superconducting magnet is used to apply the external field along a given axis and the magnetization, usually along the same axis, is measured by moving the sample through a set of pick-up coils which induces a current. This can either be done by single-shot extraction of the sample or by oscillating the sample within the coils. The induced current is proportional to the rate of change of magnetization; since for a particular measurement the magnetization is fixed and the speed of the sample is known, the measurement is sensitive to the magnitude of the magnetization.

By performing magnetometry measurements with an oscillating driving field we can access information not attainable through pure D.C. measurements. In A.C. magnetometry the oscillating magnetization itself induces a current in the pick-up coils so there is no need to move the sample. Again the induced current is proportional to the rate of change of magnetization, but since it is the magnetization itself that is varying A.C. measurements are sensitive to χ rather than M. In fact small changes in susceptibility can be detected even when the absolute moment is large.

A particular advantage of SQUID magnetometry is its sensitivity. This does, however, come at a cost. The infrastructure is quite complex and expensive, requiring helium-cooled superconducting magnets, an intricate arrangement of pickup coils and sample movement mechanism and specialist software to extract M or χ from the induced current. Since the response of the SQUID is proportional to the total magnetization, larger samples will give a stronger signal and in our measurements we require samples of the order of 20 mm^2. Furthermore, for all but the most expensive SQUID systems the external field direction and measurement axis are always parallel, so any initial field cooling can only be performed along the same direction as the subsequent measurement direction.

4.1.5 AC-AMR

In this chapter I present results from using an AMR method to measure A.C. magnetization effects. This provides a far cheaper and simpler alternative to SQUID magnetometry for making basic A.C. measurements: all that is required is a standard cryostat, a simple solenoid and two lock-in amplifiers. With this arrangement it is also possible to field-cool the sample in one direction and perform the subsequent A.C. measurements along a different axis by simply rotating the sample, which is not possible in most SQUID systems. The situation is further simplified in this case by the fact that the effect we are looking for — the SRT — will give the strongest response at zero D.C. offset, which puts less demand on the measurement and the analysis, although the principles described above remain relevant. The main disadvantage is that AMR measurements require the fabrication of a Hall bar which means the AC-AMR measurements are on processed, as opposed to as-grown, samples, and we have seen that processing can influence the anisotropies.

In A.C. measurements, inextricably linked with the magnetic susceptibility is the AMR. By performing AMR measurements rather than standard magnetometry we can greatly simplify the experimental process whilst still gaining information about the susceptibility and, since AMR measurements are not limited to large-scale samples, we can in principle perform these A.C. measurements on nanostructures.

For a Hall bar fabricated along any crystallographic direction, the strongest terms in the AMR response are a $\cos(2\varphi)$ term for the longitudinal AMR and a $\sin(2\varphi)$ term for the transverse, where φ is the angle between the current and magnetization (see chapter 2 for full details). By forcing the magnetization to oscillate we see a time-dependent variation in the longitudinal and transverse AMR signals. The amplitude of this variation depends on the angle through which the magnetization rotates, which in turn depends on the susceptibility. For a given easy axis, the larger the susceptibility the larger the amplitude of time-varying AMR signal. Similar measurements have been reported previously, in Co/CoO exchange-coupled bilayers, to identify thermodynamic

transitions [2],[3],[4].

In theory it is possible to work back from the AMR response to quantify χ, although in practice this turns out to be quite challenging. Let us consider a measurement at a fixed temperature. If one has previously measured the amplitude of the AMR as a function of φ at this temperature by rotating a saturating external field, then by measuring the amplitude of the AMR signal in an A.C. driving field one can calculate the angle through which the magnetization is rotating, so long as you know the orientation of the easy axis at this temperature. With a small field which doesn't saturate the magnetization, however, we do not know the orientation of the magnetization at each temperature so we cannot conduct this analysis. Without knowing the starting angle, a measured amplitude of the AMR could either be caused by a small-angle oscillation at an orientation φ where the AMR has a steep gradient, or a large-angle oscillation at an orientation where $dR/d\varphi$ is small. However, measuring the AMR is still useful if one takes care over the interpretation of the data.

4.2 Experimental setup

The hysteresis loops presented in chapter 3 show coercive fields of less than 100 Oe (10 mT). Assuming that, for the samples used in this study, we have coercive fields of the same order of magnitude, we require an A.C. field amplitude, H_0, of just a few millitesla. Since we require no D.C. offset the A.C. field can be provided by a standard, resistive, air-cored solenoid which is a smaller, simpler and cheaper alternative to the large, iron-cored electromagnet used in the previous AMR measurements. We designed our own solenoid to provide a field of ∼4.4 mT at 1 V bias and 2 A current, with a maximum current of 20 A and therefore around ∼44 mT for future applications — full details are provided in appendix C. All that is required in addition is a standard cryostat and the AMR measurement setup described in chapter 2, with the exception that we use lock-in amplifiers rather than voltmeters to measure the

RMS amplitude of the AMR, which is now time-varying. The reference for the lock-in amplifiers was not from the signal generator but was the voltage across a sense resistor connected in series with the solenoid, thus the reference signal was exactly in phase with the field. The Hall bar was biased with a constant current of 200 µA.

4.3 Sample details

For these measurements we selected a set of four Hall bars fabricated along the [100], [010], [110] and [$\bar{1}$10] axes from wafer number Mn309, comprising a 25nm (Ga,Mn)As film with a nominal manganese concentration of 5%. These are the very same Hall bars used in the 25 nm AMR study which complements the results on 5 nm films presented in chapter 2, mentioned briefly earlier although not presented in this Thesis (see [5]). Therefore they have already undergone general characterization measurements and the AMR has already been measured by a colleague, as shown in figure 4.4. The Hall bar dimensions are the same as for those in chapter 2.

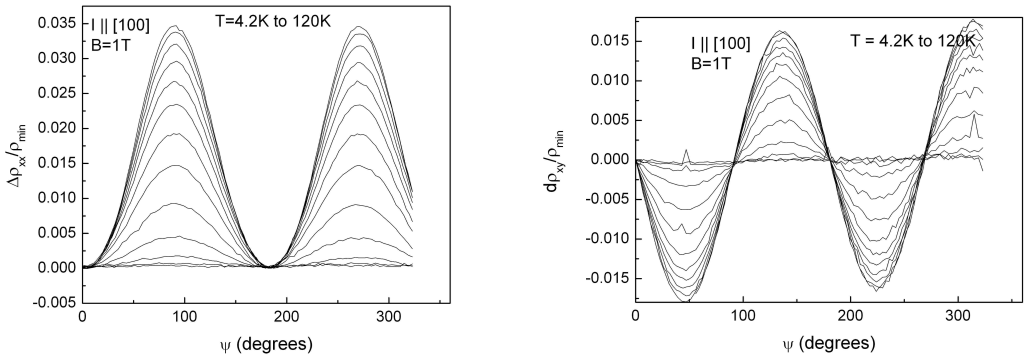

(a) Longitudinal AMR

(b) Transverse AMR

Fig. 4.4 — Longitudinal and transverse AMR for the Hall bars used in this study at temperatures from 4.2 K to 120 K, showing measurements made on the bar orientated along [100]. Figures courtesy of Dr. Andrew Rushforth.

The anisotropy coefficients for this material were extracted in the same way as in chapter 3; the magnetometry for this analysis was performed on an un-processed

sample taken from the same wafer (the Hall bars are large so the shape anisotropy and any anisotropy due to strain relaxation are negligible). The coefficients are presented in figure 4.5. The cubic coefficient has a non-monotonic functional form, not unlike that seen in chapter 3. The uniaxial coefficient has an unusual functional form, with a peak at around 30 K. The temperature at which the uniaxial and cubic coefficients are equal is about (12±2) K. Extraction of the coefficients was later repeated by a colleague using a numerical fitting procedure for the full measured hysteresis loops. A similar functional form for both K_U and K_C was seen but with a small difference in the magnitude of the uniaxial coefficient. The crossover by this method was at (14±1) K. Therefore the peak was expected in the AMR measurements to be below the range ∼10–15 K (if the peak is ∼15% below the SRT as it was in reference [1] that would put it in the range ∼8–12 K). The Curie temperature, from remanence measurements, is approximately 83 K and the resistance per square in the region of the SRT is of the order of 1 kΩ.

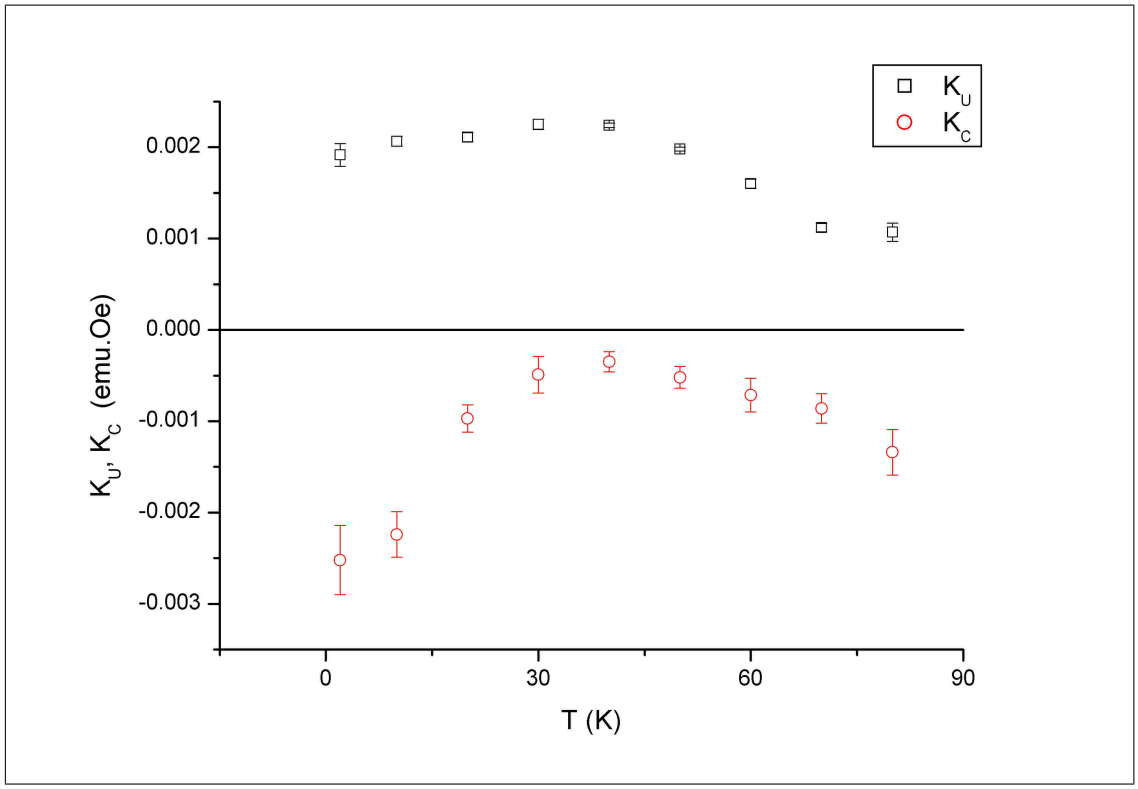

Fig. 4.5 — Anisotropy coefficients as a function of temperature for the wafer used in the fabrication of the Hall bars used for the AC-AMR measurements.

4.4 Results

Measurements were made on the Hall bar orientated along the [010] direction. This device was selected because a Hall bar at 45° to the [$\bar{1}$10] direction should give the biggest response of the longitudinal AMR to the osciallating magnetization (due to the $\cos 2\varphi$ dependence — the corollary being that the transverse AMR has a minimum gradient here, having a $\sin 2\varphi$ dependence). A frequency of 37 Hz at various field amplitudes was used to make measurements along the [010], [$\bar{1}$10] and [110] directions (measurements at further frequencies were also made in the [010] direction). Before performing each A.C. measurement the sample was field-cooled from above T_C using an external field of 3.5 mT, along the same direction as the subsequent A.C. measurement. The results for each direction are shown in figures 4.6, 4.7 and 4.8, with ±2 mT for measurements along the [110] and [$\bar{1}$10] directions and ±4.5 mT for the measurement along [010]. The temperature range shown is from base temperature to just 50 K. In figure 4.9 I show the full temperature range to above T_C for the measurement along [010].

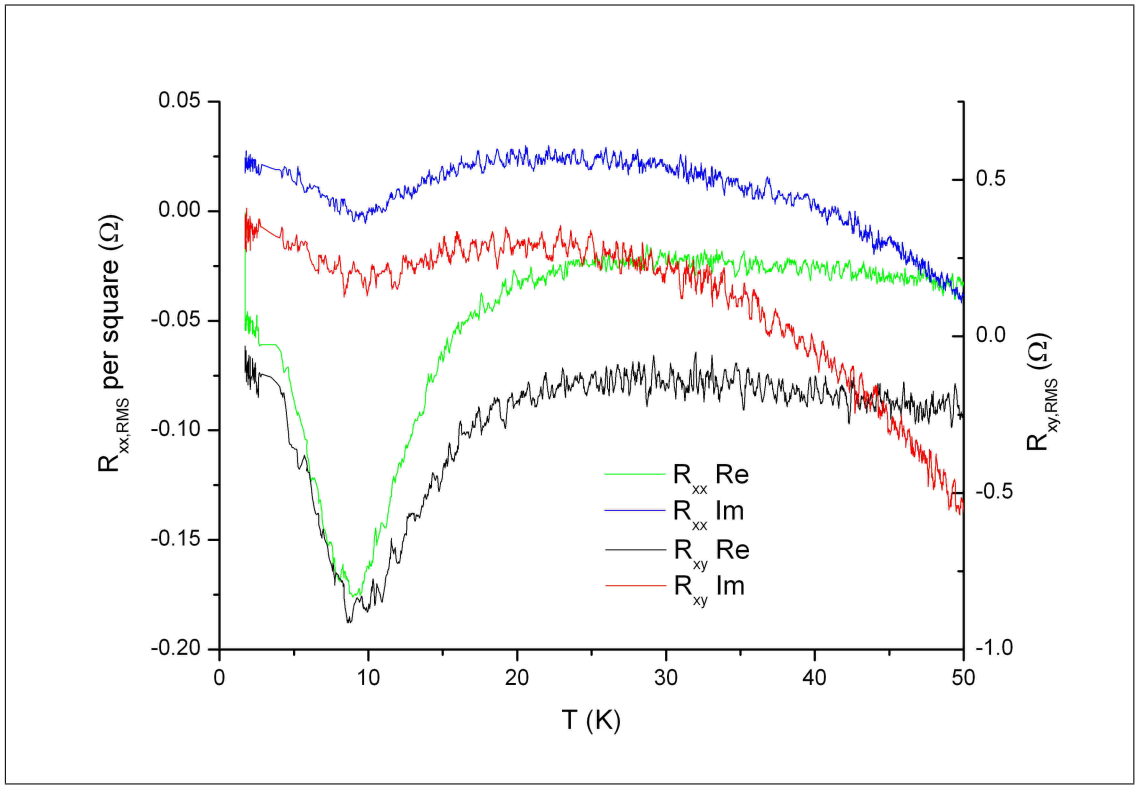

Fig. 4.6 — A.C. susceptibility measurement at 37 Hz and ±2 mT along the [110] direction for the Hall bar fabricated along [010], for temperatures up to 50 K.

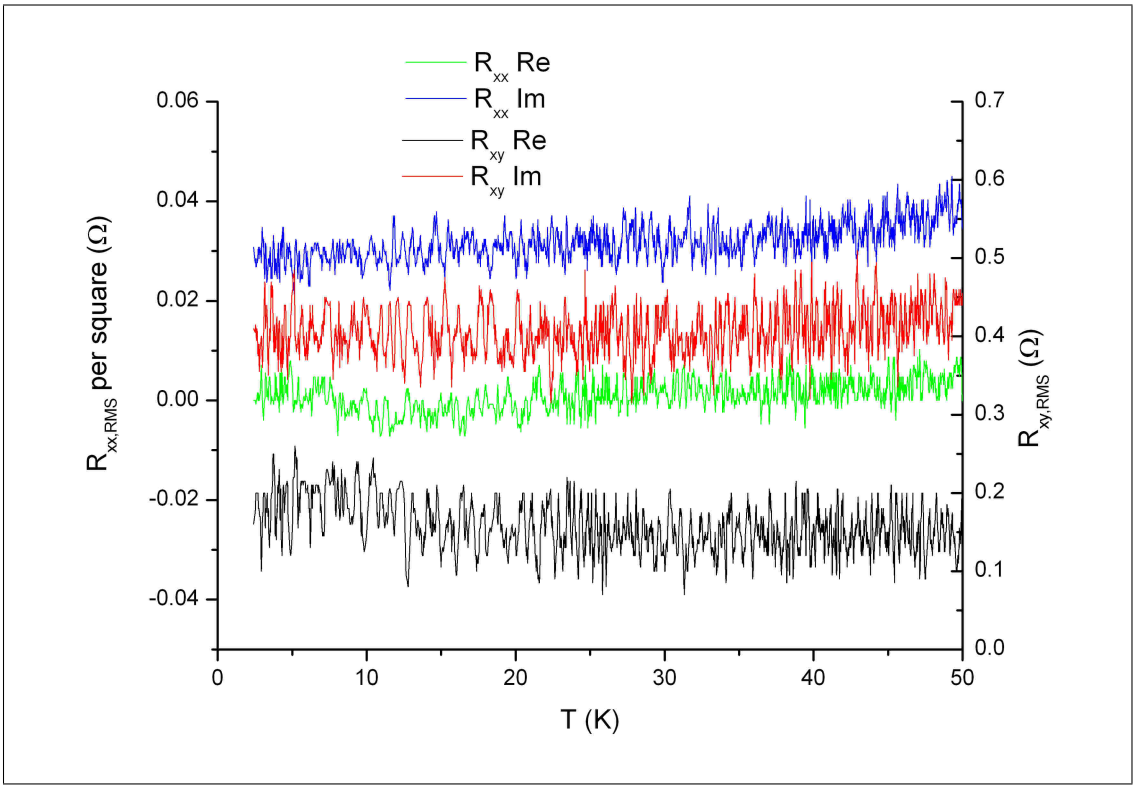

Fig. 4.7 — A.C. susceptibility measurement at 37 Hz and ±2 mT along the [$\bar{1}$10] direction for the Hall bar fabricated along [010], for temperatures up to 50 K.

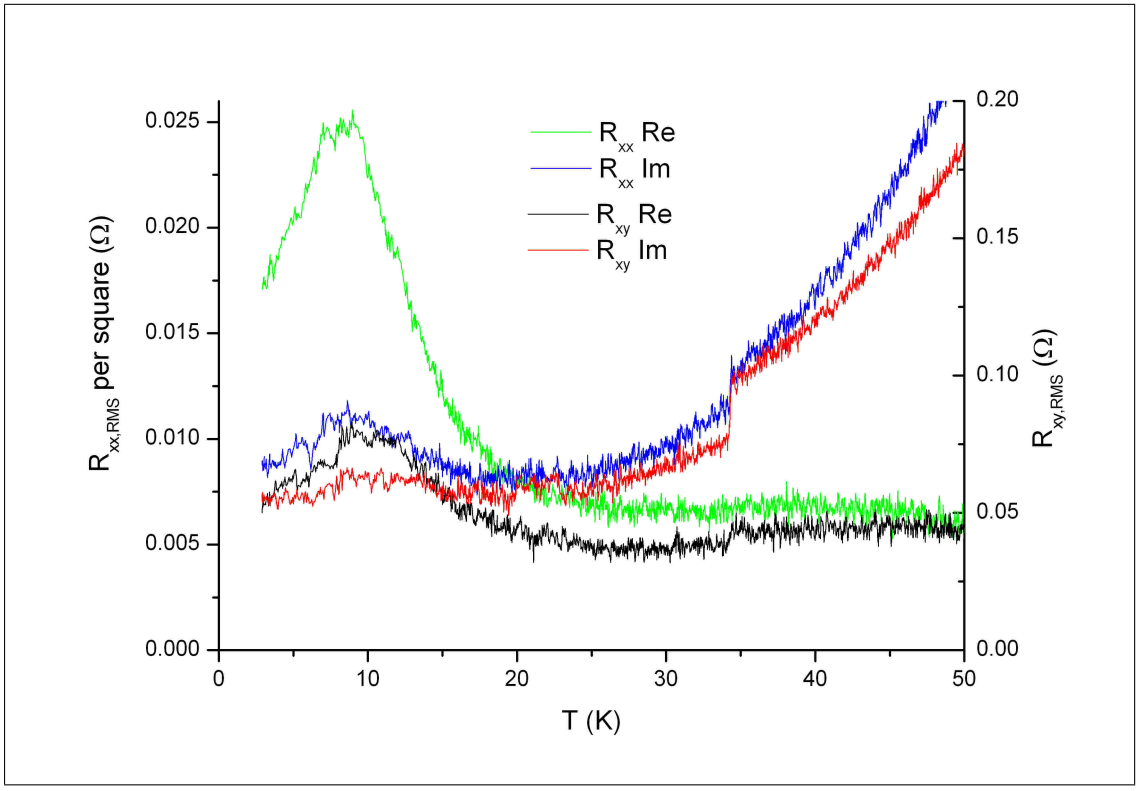

Fig. 4.8 — A.C. susceptibility measurement at 37 Hz and ±4.5 mT along the [010] direction for the Hall bar fabricated along [010], for temperatures up to 50 K.

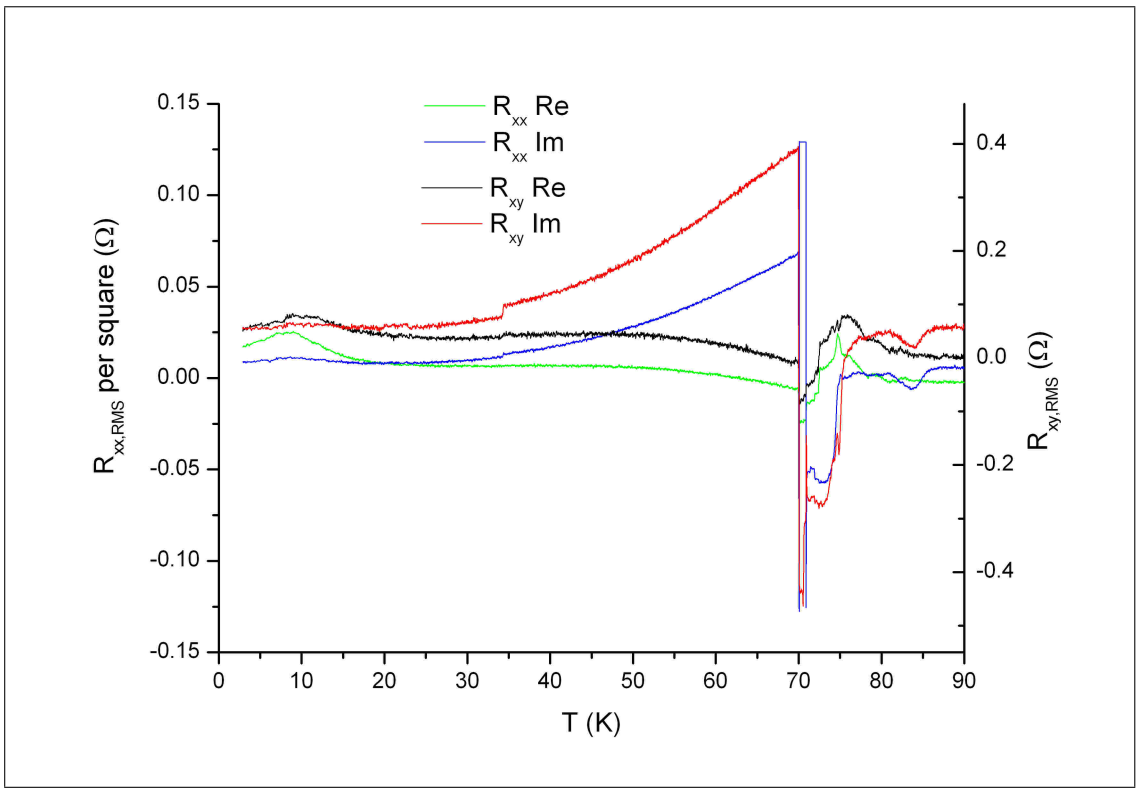

Fig. 4.9 — As for figure 4.8 but showing the full temperature range, that is up to above T_C.

4.5 Discussion

The results close to the SRT are much as expected: the measurement along the [110] direction shows a large peak just below 10 K; there is no peak in the measurement along $[\bar{1}10]$; and there is a peak in the [010] measurement but it is almost an order of magnitude smaller than the [110] peak. The peaks occur where expected in temperature, i.e. a little below the ∼10–15 K range where we calculated the crossover of the anisotropy coefficients. Above the SRT we see unexpected features, as seen in figure 4.9 which shows the full temperature range; these include a steady change in the real and imaginary parts of both the longitudinal and transverse resistances between around 30 K and 70 K and an intricate variation in R against temperature above 70 K, the detailed structure of which is dependent on temperature and external field amplitude and is entirely reproducible. These were seen in *all* measurements but it is not clear whether they are due to the sample itself or whether they are an

artefact of the measurement setup.

There appear to be D.C. offsets in some of the data sets. These are seen when the Hall bar current is removed and are therefore an artefact of the measurement setup rather than a true response of the AMR to the A.C. field. In further studies it would be useful to take steps to remove these offsets.

4.6 Summary and Future Work

Qualitatively we have reproduced the features at the SRT that were both expected and previously reported after standard magnetometry measurements [1], but using a simpler and cheaper method. This technique should be viable when looking for any peak in the A.C. susceptibility, not just peaks caused by a Spin Reorientation Transition, for any system which has a measurable AMR; in principle the technique could even be used on nanostructures.

The R_{xx} peaks are not consistently stronger than the R_{xy} peaks as had been expected — this is clearly an issue which warrants further investigation. It is also worth adding that the anisotropy coefficients were extracted from data measured on a separate piece of the parent wafer that had undergone no processing, whereas the AC-AMR measurements were made on processed samples from a different part of the parent wafer. Other areas for future study could include investigation of the frequency- and field-dependence of the AC-AMR, looking at the other three Hall bars, and field cooling along orientations other than the measurement axis. It is also possible to calculate the expected response of the AMR in simulations that use the anisotropy coefficients as the main parameters.

References

[1] K.-Y. Wang, M. Sawicki, K. W. Edmonds, R. P. Campion, S. Maat, C. T. Foxon, B. L. Gallagher, and T. Dietl, "Spin Reorientation Transition in Single-Domain (Ga, Mn)As ," *Physical Review Letters*, vol. 95, p. 217204, 2005.

[2] D. Venus, F. Hunte, I. N. Krivorotov, T. Gredig, and E. D. Dahlberg, "Magnetic relaxation in exchange-coupled Co/CoO bilayers measured with ac-anisotropic magnetoresistance," *Journal of Applied Physics*, vol. 93, no. 10, pp. 8609–8611, 2003.

[3] D. Venus and F. Hunte, "Competition between magnetic relaxation mechanisms in exchange-coupled CoO/Co bilayers," *Physical Review B*, vol. 72, p. 024404, 2005.

[4] D. Venus, F. Hunte, and E. Dan Dahlberg, "Contribution of low-temperature degrees of freedom to the anisotropy in Co/CoO exchange coupled bilayers," *Journal of Magnetism and Magnetic Materials*, vol. 286, pp. 191–195, 2005.

[5] A. W. Rushforth, K. Výborný, C. S. King, K. W. Edmonds, R. P. Campion, C. T. Foxon, J. Wunderlich, A. C. Irvine, P. Vašek, V. Novák, K. Olejník, J. Sinova, T. Jungwirth, and B. L. Gallagher, "Anisotropic Magnetoresistance Components in (Ga,Mn)As," *Physical Review Letters*, vol. 99, p. 147207, 2007.

Chapter 5

Conclusions and Future Work

The ferromagnetic semiconductor gallium manganese arsenide exhibits strong Spin-Orbit Coupling which results in magnetoresistive anisotropies. Anisotropy of the magnetoresistance is responsible for several new effects which are of potential technological importance, including Tunnelling Anisotropic Magnetoresistance and Coulomb Blockade Anisotropic Magnetoresistance. However, until now there has been no systematic study of the simpler Anisotropic Magnetoresistance in this material. In chapter 2 a systematic study on 5 nm (Ga,Mn)As films reveals that a uniaxial crystalline component can dominate the AMR, the first time this has been seen in any material system to our knowledge.

The SOC is also responsible for the rich magnetocrystalline anisotropy in (Ga,Mn)As, the exact form of which is is in part determined by the degree of growth strain incorporated into the material. It is possible to allow the growth strain to relax in a somewhat-controllable manner by lithographically patterning the material into structures with dimensions of a micron or less. In chapter 3 it is shown that such patterning can strongly modify the anisotropy landscape, in one case even rotating the easy axis by 90°. Whilst it has been inferred through finite elements simulations that the mechanism responsible for the change in magnetocrystalline anisotropy is indeed strain relaxation, it would be of further interest to perform x-ray measurements on

these samples to quantify the growth strain in the parent wafer and the relaxation for the stripes along each of the [110] and [$\bar{1}$10] directions. To extend the work into a slightly different direction our group has also begun to look at the magnetocrystalline anisotropy of samples patterned into L-shaped bars of similar widths to the stripes in this report, both with identical arms and with arms of unequal length, which we expect to reveal new features in the hysteresis data and subsequent analysis.

In the final experimental chapter it was seen that a new technique based on AMR measurements can be used to identify the Spin Reorientation Transition in samples which are biaxial at low temperature; this is the point in the temperature domain at which the uniaxial and cubic anisotropy coefficients cross over. Compared with the more conventional A.C. SQUID magnetometry measurements this technique is cheaper and simpler, whilst the main features of the magnetometry data were qualitatively reproduced. It would be of interest to take this further by investigating the frequency- and field-dependence of the peak near the SRT as well as looking into the discontinuities seen in the data at higher temperatures, as well as field-cooling the samples along different orientations and comparing the data with simulations of the expected response of the system.

Appendix A

Extraction of Crystalline AMR Terms from Hall Bar Data

The longitudinal AMR — equation 2.1 in chapter 2 — is repeated here (see figure 2.1 for definitions of the angles):

$$\frac{\Delta\rho_{xx}}{\rho_{av}} = C_I \cos 2\varphi + C_U \cos 2\psi + C_C \cos 4\psi + C_{I,C} \cos(4\psi - 2\varphi) \tag{A.1}$$

We can combine Hall bar measurements from pairs of orthogonal bars in such a way that the non-crystalline terms drop out (terms in φ) leaving just the crystalline terms (terms in ψ). Let us consider a pair of bars fabricated along the [100] and [010] crystallographic directions by way of example — the [110]–[$\bar{1}$10] pairing follows a similar procedure. We extract the crystalline terms by calculating the following (from equation 2.3):

$$\left[\left(\frac{\Delta\rho_{xx}}{\rho_{av}}\right)_{[100]} + \left(\frac{\Delta\rho_{xx}}{\rho_{av}}\right)_{[010]}\right]/2 = C_U cos2\psi + C_C cos4\psi \tag{A.2}$$

Let us show that this works. First it is helpful to expand the $C_{I,C}$ term in equation A.1 using trigonometrical addition rules, giving:

$$\frac{\Delta\rho_{xx}}{\rho_{av}} = C_I \cos 2\varphi + C_U \cos 2\psi + C_C \cos 4\psi + C_{I,C} \cos 4\psi \cos 2\varphi + C_{I,C} \sin 4\psi \sin 2\varphi$$

Substituting this into the numerator of A.2:

$$\begin{aligned}\left(\frac{\Delta\rho_{xx}}{\rho_{av}}\right)_{[100]} + \left(\frac{\Delta\rho_{xx}}{\rho_{av}}\right)_{[010]} = \\ C_I \cos 2\varphi_{(Ialong[100])} + C_U \cos 2\psi + C_C \cos 4\psi + \\ C_{I,C} \cos 4\psi \cos 2\varphi_{(Ialong[100])} + C_{I,C} \sin 4\psi \sin 2\varphi_{(Ialong[100])} + \\ C_I \cos 2\varphi_{(Ialong[010])} + C_U \cos 2\psi + C_C \cos 4\psi + \\ C_{I,C} \cos 4\psi \cos 2\varphi_{(Ialong[010])} + C_{I,C} \sin 4\psi \sin 2\varphi_{(Ialong[010])}\end{aligned}$$

Grouping terms gives

$$\begin{aligned}\left(\frac{\Delta\rho_{xx}}{\rho_{av}}\right)_{[100]} + \left(\frac{\Delta\rho_{xx}}{\rho_{av}}\right)_{[010]} = \\ C_I(\cos 2\varphi_{(Ialong[100])} + \cos 2\varphi_{(Ialong[010])}) + \\ C_{I,C} \cos 4\psi(\cos 2\varphi_{(Ialong[100])} + \cos 2\varphi_{(Ialong[010])}) + \\ C_{I,C} \sin 4\psi(\sin 2\varphi_{(Ialong[100])} + \sin 2\varphi_{(Ialong[010])}) + \\ 2(C_U \cos 2\psi + C_C \cos 4\psi)\end{aligned} \tag{A.3}$$

By consideration of the definition of φ for the current along the different crystallographic orientations (figure A.1),

$$\cos 2\varphi_{Ialong[100]} = \cos(2\varphi_{Ialong[010]} + 180^\circ) = -\cos 2\varphi_{Ialong[010]}$$

$$\sin 2\varphi_{Ialong[100]} = \sin(2\varphi_{Ialong[010]} + 180^\circ) = -\sin 2\varphi_{Ialong[010]}$$

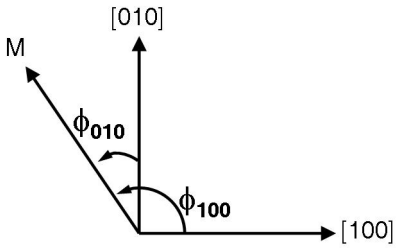

Fig. A.1 — Angles between current direction and crystallographic axes.

Substituting into A.3 most of the terms drop out leaving

$$\left(\frac{\Delta\rho_{xx}}{\rho_{av}}\right)_{[100]} + \left(\frac{\Delta\rho_{xx}}{\rho_{av}}\right)_{[010]} = 2C_U\cos 2\psi + 2C_C\cos 4\psi$$

So equation A.2 is as follows, comprising only the pure crystalline terms:

$$\frac{\left(\frac{\Delta\rho_{xx}}{\rho_{av}}\right)_{[100]} + \left(\frac{\Delta\rho_{xx}}{\rho_{av}}\right)_{[010]}}{2} = C_U\cos 2\psi + C_C\cos 4\psi \tag{A.4}$$

The same terms can be measured directly by measuring a Corbino ring instead of Hall bars. In Corbino measurements the current is radial so terms involving φ are eliminated from equation A.1 as we integrate the equation from $\varphi = 0^\circ$ to $\varphi = 360^\circ$; once again, only the crystalline terms remain:

$$\begin{aligned}\frac{\Delta\rho_{corbino}}{\rho_{av}} &= \int_{\varphi=0}^{360}\left[C_I\cos 2\varphi + C_U\cos 2\psi + C_C\cos 4\psi + C_{I,C}\cos(4\psi - 2\varphi)\right]d\varphi \\ &= C_U\cos 2\psi + C_C\cos 4\psi\end{aligned}$$

Appendix B

Derivation of the Fitting Formulae for the Extraction of Anisotropy Coefficients from Hard-axis Hysteresis Measurements

Hard axis along [110]

Here I show how, starting with the stability condition $\frac{\partial E}{\partial \theta} = 0$ given in equation 3.9, I derive the fitting equation given in equation 3.12. First rewrite the three terms in 3.9 so they are each in $\cos\theta$:

$$K_U \sin 2\theta + K_C \sin 2\theta \cos 2\theta - M_S H \cos\theta = 0$$

$$K_U \sin 2\theta + K_C \sin 2\theta \left(1 - 2\sin^2\theta\right) - M_S H \cos\theta = 0$$

$$K_U \sin 2\theta + K_C \sin 2\theta - 2K_C \sin^2\theta \sin 2\theta - M_S H \cos\theta = 0$$

$$2K_U \sin\theta \cos\theta + 2K_C \sin\theta \cos\theta - 4K_C \sin^2\theta \sin\theta \cos\theta - M_S H \cos\theta = 0$$

Then divide by $\cos\theta$:

$$2K_U \sin\theta + 2K_C \sin\theta - 4K_C \sin^2\theta \sin\theta - M_S H = 0$$
$$2\left(K_U + K_C\right)\sin\theta - 4K_C \sin^3\theta - M_S H = 0$$

Finally make the substitution $\sin\theta = \left(M_{[110]}/M_S\right)$:

$$2\left(\frac{K_U + K_C}{{M_S}^2}\right) M_{110} - 4\left(\frac{K_C}{{M_S}^4}\right) {M_{110}}^3 = H$$

Hard axis along [$\bar{1}$10]

Here I derive the fitting function, equation 3.13, in full. First find H_C given that $M_{[\bar{1}10]} = M_S \cos\theta$ for $H < H_C$.

$$\begin{aligned}
\gamma &= 0 \\
E &= K_{U,\bar{1}10} \sin^2\theta + K_{U,110} \sin^2(\theta - 90) + (K_C/4) sin^2(2\theta) - M_S H \cos\theta \\
&= \left(K_{U,\bar{1}10} - K_{U,110}\right) \sin^2\theta + (K_C/4) sin^2(2\theta) - M_S H \cos\theta + K_{U,110} \\
\frac{\partial E}{\partial \theta} &= 2K_U \sin\theta\cos\theta + K_C \sin 2\theta \cos 2\theta + M_S H \sin\theta = 0 \\
&= K_U \sin 2\theta + \frac{K_C}{2} \sin 4\theta + M_S H \sin\theta \\
\frac{\partial^2 E}{\partial \theta^2} &= 2K_U \cos 2\theta + 2K_C \cos 4\theta + M_S H \cos\theta > 0
\end{aligned}$$

Find H_C by putting $\theta = 0$:

$$\begin{aligned}
0 &< 2K_U + 2K_C + M_S H \\
H &> -2\left(K_U + K_C\right)/M_S \\
H_C &= -2\left(K_U + K_C\right)/M_S \\
M_{[\bar{1}10]} &= M_S \cos\theta = M_S \qquad \text{for} \qquad H > -2(K_U + K_C)/M_S
\end{aligned}$$

Substitute this into $(\partial E/\partial\theta = 0)$ to find the fitting formula:

$$\frac{\partial E}{\partial \theta} = 2K_U \sin\theta\cos\theta + K_C \sin 2\theta \cos 2\theta + M_S H \sin\theta = 0$$

$$0 = 2K_U \sin\theta\cos\theta + 2K_C \sin\theta\cos\theta\cos 2\theta + M_S H \sin\theta$$

$$0 = 2K_U \sin\theta\cos\theta + 2K_C \sin\theta\cos\theta\left(2\cos^2\theta - 1\right) + M_S H \sin\theta$$

$$0 = 2K_U \cos\theta + 4K_C \cos^3\theta - 2K_C \cos\theta + M_S H$$

$$H = -2\left(\frac{K_U - K_C}{M_S}\right)\cos\theta - 4\left(\frac{K_C}{M_S}\right)\cos^3\theta$$

$$H = -2\left(\frac{K_U - K_C}{{M_S}^2}\right)M_{\bar{1}10} - 4\left(\frac{K_C}{{M_S}^4}\right){M_{\bar{1}10}}^3$$

Appendix C

Solenoid Design

For a long solenoid with $r << R << L$ where r is the wire radius, R is the solenoid radius and L is the solenoid length, the field at the centre is given by:

$$B_0 = \frac{\mu_0 I n}{L} \tag{C.1}$$

and at the edge it is

$$B = \frac{\mu_0 I n}{2L} = \frac{B_0}{2} \tag{C.2}$$

where I is the current and n is the number of turns per metre.

We designed a solenoid to provide a maximum field of ∼40 mT at currents up to ∼20 A (this was higher than we required but allowed the solenoid to be useful for future applications). The following constraints limited our design. The absolute upper limit for the length of the solenoid was 35 cm, limited by the clearance around our cryostat; the tail of the cryostat has a diameter of 50 mm. We chose a length of 30 cm, wire conforming to the *Standard Wire Gauge 14* standard (SWG 14) so capable of carrying 20 A, with four layers. The parameters were as follows:

- Solenoid length, L, = 30 cm

- Solenoid diameter, D, = 60 mm
- Number of layers = 4
- SWG 14 wire diameter = 2.03 mm
- Measured wire diameter (including varnish) = 2.13 mm
- Estimated spacing on coil, d, = 2.3 mm
- Number of turns per metre per layer = 435
- Number of turns per metre, n, = 1740
- Number of turns on solenoid, N, = $n \times L = 522$
- Total wire length = $N\pi D$ = 98 m
- Total solenoid resistance = 98 m × 5.2 Ω/km = 0.5 Ω
- Weight of copper = 8920 kg/m^3 × $L \times A$ = 3 kg
- Field, H, = $\mu_0 nI$
  - Therefore 1 V gives 2 A, 4.4 mT and 2 W
- Inductance, L', = $\mu_0 N^2 A = 4\pi \times 10^{-7} \times 522^2 \times \pi(0.06/2)^2 = 1$ mH
- Reactance at 5 Hz, X_{5Hz}, = $\omega L' = 0.03$ Ω

Appendix D

Angle Definitions

For simplicity and consistency the same angle definitions have been used consistently throughout the whole Thesis. The angles are defined as in the following figure. Further details can be found in the introductions to chapters 2 and 3.

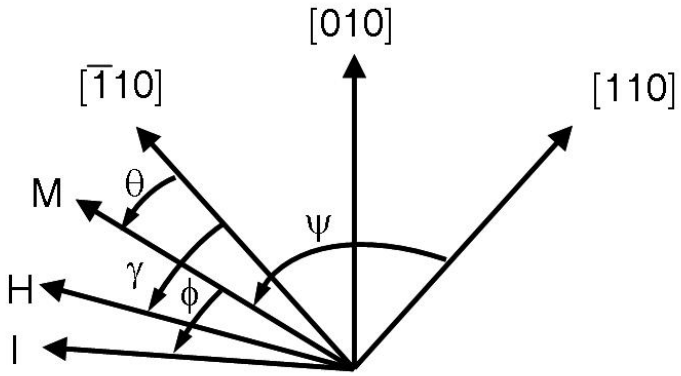

Fig. D.1 — Angle definitions used consistently throughout this Thesis.

Appendix E

List of Acronyms

AMR Anisotropic Magnetoresistance

CB-AMR Coulomb Blockade Anisotropic Magnetoresistance

DMS Dilute Magnetic Semiconductor

GMR Giant Magnetoresistance

MBE Molecular Beam Epitaxy

RMS Root Mean Square

SQUID Superconducting Quantum Interference Device

SOC Spin-Orbit Coupling

SRT Spin Reorientation Transition

TAMR Tunnelling Anisotropic Magnetoresistance

Appendix F

Units of Magnetization

$$1\ \mathrm{T} \equiv 1\ \mathrm{Wb/m^2} \equiv 1\ \mathrm{NA^{-1}m^{-1}}$$

$$1\ \mathrm{J} \equiv 1\ \mathrm{Nm}$$

$$1\ \mathrm{Wb} \equiv \frac{1}{4\pi \times 10^{-7}}\ \mathrm{Am}$$

$$1\ \mathrm{Oe} \equiv \frac{10^3}{4\pi}\ \mathrm{Am^{-1}} \equiv 10^{-4}\ \mathrm{T}$$

$$1\ \mathrm{emu} \equiv 10^{-3}\ \mathrm{Am^2}$$

$$1\ \mathrm{emu \cdot Oe} \equiv 10^{-7}\ \mathrm{J}$$

$$1\ \mathrm{emu/cm^3} \equiv 4\pi \times 10^{-4}\ \mathrm{T}$$

$$1\ \left(\mathrm{emu/cm^3}\right)^2 \equiv 4\pi \times 10^{-1}\ \mathrm{Jm^{-3}}$$

$$1\ \mathrm{T^2} \equiv \frac{1}{4\pi \times 10^{-7}}\ \mathrm{Jm^{-3}}$$

$$1\ \mathrm{erg/cm^3} \equiv 10^{-1}\ \mathrm{Jm^{-3}}$$